

PREDICTION OF TORNADO INFRASOUND WITHIN THE TURBULENT ATMOSPHERE
USING THEORY, NUMERICAL SIMULATION, WIND TUNNEL MEASUREMENTS, AND
FIELD-TESTS

By

TIANSHU ZHANG

A DISSERTATION PRESENTED TO THE GRADUATE SCHOOL
OF THE UNIVERSITY OF FLORIDA IN PARTIAL FULFILLMENT
OF THE REQUIREMENTS FOR THE DEGREE OF
DOCTOR OF PHILOSOPHY

UNIVERSITY OF FLORIDA

2021

© 2021 Tianshu Zhang

To my parents who are always supportive in my life

ACKNOWLEDGEMENTS

There are numerous people who supported me throughout the writing of this dissertation. First, I would like to thank my parents, Kan Zhang and Cuixian Zhang, for their invaluable love and support in my life. They always are my strongest backing whenever I encounter troubles and obstacles.

I want to express my sincere gratitude to my advisor, Dr. Steven A. E. Miller. As my mentor in the world of academic research, he guided me through numerous challenges and provided me with incredible resources. Thank you for teaching me how to plan and conduct the research efficiently. Your passion for research and pursuit of excellence will be my life-long goal to chase. I also would like to thank Dr. Kurtis Gurley, Dr. Ryan W. Houim, and Dr. Saeed Moghaddam for serving as my committee members. Their insights and suggestions greatly improved this work, and they also helped me with my writing and presentation skills.

I would like to thank my colleagues and friends in the Theoretical Fluid Dynamics and Turbulence Group, Alex Carr, Jianhui Chen, Trushant Patel, Weiqi Shen, and Wei Wang. Their supports helped me avoid detours when I was exploring new techniques and tools. Exchange of ideas with them always makes the work enjoyable.

I am grateful for the supports I received from the technicians and staff of Powell Family Structures and Materials Laboratory, especially the lab manager Mr. Scout Powell. The wind tunnel experiments would not have been possible without their help. I would like to acknowledge Mariel Ojeda-Tuz for her help in experimental data management and analysis. I am also grateful for the assistance I received from James Goldschmidt and Songqi Li in the anechoic chamber tests.

I am also grateful for continual funding from NOAA. This program is supported by the NOAA Weather and Air Quality Research program award number NA18OAR4590306. The program would not have been possible without their funding supports.

TABLE OF CONTENTS

	<u>page</u>
ACKNOWLEDGEMENTS	4
LIST OF TABLES.....	7
LIST OF FIGURES.....	10
ABSTRACT	11
CHAPTER	
1 INTRODUCTION	13
1.1 Motivation.....	13
1.2 Objective and Scope of Proposed Work	15
1.3 Current Tornado Damage Rating and Warning System	17
1.4 Tornado Infrasound	20
1.5 Physical Effects in Acoustic Propagation.....	21
1.5.1 Nonlinearity	21
1.5.2 Atmospheric Attenuation and Dispersion	24
1.5.3 Refraction and Shadow Zone.....	26
1.5.4 Turbulent Scattering.....	27
1.6 Numerical Propagation Models	28
1.7 Atmospheric Models.....	30
1.8 Structure of the Dissertation	34
2 NUMERICAL AND EXPERIMENTAL TECHNIQUES.....	36
2.1 Acoustic Ray Tracing	38
2.2 Propagation Models and Scheme	39
2.2.1 Geodisc Elements and Convective Volume.....	39
2.2.2 Discrete System and Atmosphere Model.....	40
2.2.3 Generalized Burgers' Equation.....	41
2.3 Lighthill's Scattering Models	44
2.4 Tartaski's Scattering Model.....	47
2.5 Ostashev and Wilson's Model	51
2.6 Acoustic-Turbulent Interaction Bridging Model	53
2.6.1 Turbulent Refraction and Bridging Model	53
2.6.2 Log Amplitude and Phase Fluctuation	58
2.7 Summary.....	58
3 RESULTS OF NUMERICAL SOLVER.....	59
3.1 Validation of the Numerical Solver.....	59
3.1.1 Ray Tracing Validation	59
3.1.2 Propagation Solver Validation.....	65
3.2 Preliminary Results of the Numerical Solver	68
3.2.1 Ray Tracing Results for Propagation Test Cases.....	69
3.2.2 Propagation Solver Case Study without Turbulent Model.....	70
3.3 Summary.....	75

4	WIND TUNNEL EXPERIMENTS AND MEASUREMENTS	76
4.1	University of Florida Turbulent Boundary Layer Wind Tunnel.....	76
4.2	Stages of the Experiment Campaign	78
4.2.1	Stage 1: UFBLWT Acoustic Conditions, Test Signal Design, and Anechoic Chamber Test	78
4.2.2	Stage 2: Turbulent Measurement in the UFBLWT.....	83
4.2.3	Stage 3: Acoustic Propagation Experiment in the Wind Tunnel	85
4.3	UFBLWT Experimental Results	88
4.3.1	Turbulent Measurements.....	90
4.3.2	Acoustic Recording and Post Processing.....	93
4.4	Field Measurements of Infrasound and Weather Data from Tornadoes	97
4.5	Summary.....	98
5	VALIDATION, SENSITIVITY, NUMERICAL ANALYSIS OF THE BRIDGING MODEL.....	99
5.1	Validation by the UFBLWT Experimental Data.....	99
5.1.1	UFBLWT Experiments Setup	100
5.1.2	Predictions Compared to UFBLWT Measurements.....	101
5.2	Sensitivity Analysis.....	105
5.2.1	Parameter Sensitivity in the Scattering Model.....	105
5.2.2	Effects of Parameters in Numerical Propagation Solver.....	107
5.3	Numerical Model Analysis and Parametric Study of the Propagation Solver.....	112
5.4	Summary and Conclusion	117
6	CONCLUSION AND FUTURE WORK	119
6.1	Summary of Results	119
6.1.1	Summary of The Bridging Model for Acoustic-Turbulent Interaction.....	121
6.1.2	Summary of The Ray Tracing Solver and Burgers' Equation Solver	122
6.1.3	Summary of the UFBLWT Propagation Experiments.....	122
6.1.4	Summary of the Numerical Investigation of the Bridging Model	123
6.2	Future Work.....	124
6.2.1	Explosion Infrasound Propagation.....	125
6.2.2	Sonic Boom Propagation	126
	APPENDIX: DATA ORGANIZATION AND DESIGNSAFE STORAGE.....	127
	REFERENCES	131
	BIOGRAPHICAL SKETCH	146

LIST OF TABLES

<u>Tables</u>	<u>page</u>
3-1 Ray tracing solver validation matrix and comparison with Hallbergs' solver.	62
3-2 Turning-point location difference between time step size = 0.1 s, 0.05 s, 0.01 s.	64
3-3 Nonlinearity Validation Matrix.....	66
4-1 Acoustic and turbulent test matrices.....	89
5-1 Validation Cases from UFBLWT	103

LIST OF FIGURES

<u>Figures</u>	<u>page</u>
1-1 Aerial view of the St. John's Regional Medical Center campus.	13
1-2 Annual average death rate from tornados.	14
1-3 Demonstration of the EF scale damage.	18
1-4 Nonlinearity caused by the local heating effect.	22
1-5 Example of total absorption coefficient at 0.4 Hz, with contributions from individual loss mechanisms shown separately.	25
1-6 Static sound speed profiles that include the effects of dispersion over a range of frequencies.	26
2-1 Flowchart of the numerical solver and techniques used in the solver.	36
2-2 Ray tube and convective volume.	39
2-3 Grid system and interpolation method.	41
2-4 Wind speed and temperature profiles at longitude: -82.3248262° W and latitude: 29.6516344° N.	42
2-5 Concept of the bridging model.	53
2-6 An example of the bridging cross-section model compared with Ostashev's model.	57
3-1 Validation with previous two-dimensional solver of Hallberg.	60
3-2 Test cases with different vertical launching angles from -82.3248262° W, 29.6516344° N, along latitude 29.6516344° N.	60
3-3 Comparison between the ray tracing solver and Hallberg's solver.	63
3-4 Ray tracing solver validation with linear temperature and wind profiles, time step sizes are 0.1 s, 0.05 s, and 0.01 s	63
3-5 Ray tracing solver validation with linear temperature and wind profiles, three launching angles are 15° , 30° , and 45°	64
3-6 Comparison between my RTS and Hallberg's solver	65
3-7 Nonlinear effect validation of the propagation solver by comparing with the BBF solution at different σ	67
3-8 Absorption Coefficient Validation.	68
3-9 Acoustic ray tracing result of the HAV case (Up: Westward propagation, Down: Eastward Propagation).	69
3-10 Acoustic ray tracing result of the MCI case (Up: Westward propagation, Down: Eastward Propagation).	70
3-11 A 140 dB and 3 Hz sine wave signal propagation.	72

3-12	Nonlinear coefficient in the near source region	73
3-13	120 dB 5 Hz signal propagation in MCI area.	73
3-14	Broadband signal propagation in MCIE case.	74
3-15	CFD simulated tornado and the spectrum of its tornadic infrasound.	74
3-16	CFD tornadic infrasound signal propagation result; Black: source signal, Red: signal at observer.	75
4-1	University of Florida Boundary Layer Wind Tunnel, acoustic configuration, and a roughness element.	77
4-2	Example of four different RPMs wind tunnel background noise spectra.	79
4-3	Raw anechoic chamber source signal recording at 2 m from the speaker.	80
4-4	Acoustic system (Left: speaker; Right: microphone) in anechoic chamber with the propagation distance = 3 m.	81
4-5	Single cycle signals at 2 m away from speaker.	82
4-6	Coordinates calibration of Three-Cobra-Probe (TCP) system at $Z = 590$ mm.	84
4-7	Turbulent Field at $EH = 30$ mm, $EL = 900$ mm, and $WS = 5.3$ m/s.	84
4-8	Microphone location and speaker location.	86
4-9	Speaker at $EL = 590$ with the supporting system.	87
4-10	GRAS 46BE 1/4 inch CCP free field standard microphone at $EL = 590$ mm with the supporting system.	88
4-11	Experimental schematic from the UFBLWT acoustic propagation tests.	89
4-12	PSD of x -direction turbulent velocity.	90
4-13	Boundary layer profiles along the x -direction, with $EH = 30$ mm and $WS = 6$ m/s.	91
4-14	Longitudinal turbulent intensity I_u with $EH = 30$ mm, $WS = 6$ m/s.	91
4-15	Auto correlation with $EH = 30$ mm.	92
4-16	TKE measurements with $EH = 0$	93
4-17	Wind tunnel recording with $EH = 10$ mm, $EL = 170$ mm, and wind speed = 3.26 m/s.	94
4-18	Ensemble signal of 1250 Hz with $EH = 30$ mm, and $EL = 590$ mm.	95
4-19	Amplitudes of the test signal at $EH = 0$ mm.	96
4-20	Amplitudes of the test signal at $EH = 50$ mm.	97
4-21	Field experiment equipment.	98

5-1	Output single cycle signals at 2 m from speaker.....	100
5-2	The comparison between the experimental results and numerical predictions with reflection isolated.....	104
5-3	The error comparison between the bridging model and Ostashev's model.	104
5-4	Turbulent kinetic energy and length scale predicted by Apsley's model.....	106
5-5	The sensitivity of the scattering models.....	107
5-6	Predicted received waveform relative to N wave source.	108
5-7	Shock wave propagation results and sensitivity analysis.	109
5-8	Reconstructed tornadic infrasound spectrum via Frazier's model.....	111
5-9	Numerical Prediction of the Tornadic Infrasound Propagation.	112
5-10	Sensitivity analysis of the tornadic infrasound case.....	113
5-11	Absorption coefficient with respect to TKE and acoustic frequency.	114
5-12	Absorption coefficient as a function of turbulent length scale and frequency.	115
5-13	Coefficient difference between the bridging model and Ostashev's model.	116
5-14	Δ OASPL of the bridging model with varying L_v and TKE.	116
5-15	Absorption coefficient distribution in frequency and altitude.....	117
A-1	Data Depot Structure.....	127

Abstract of Dissertation Presented to the Graduate School
of the University of Florida in Partial Fulfillment of the
Requirements for the Degree of Doctor of Philosophy

PREDICTION OF TORNADO INFRASOUND WITHIN THE TURBULENT ATMOSPHERE
USING THEORY, NUMERICAL SIMULATION, WIND TUNNEL MEASUREMENTS, AND
FIELD-TESTS

By

Tianshu Zhang

December 2021

Chair: Steven A. E. Miller

Major: Aerospace Engineering

A tornado creates infrasound that propagates over long distances. Triangulation of the formation position via infrasound measurement will allow for early warning systems to be developed. Infrasound propagation is altered by atmospheric turbulence, which must be accounted for to detect tornadoes. A joint program of numerical simulation, wind tunnel experiment, and field-test program is conducted to accurately model the alteration of infrasound propagation. We develop a numerical prediction solver for tornadic infrasound propagation in an inhomogeneous moving medium, which is a representative model for the effect of atmospheric turbulence on long-range propagation. The ray tracing method and generalized Burgers' equation are implemented within a solver to capture the effects of nonlinearity, refraction, attenuation, and dispersion. The geodesic element method is employed to account for the effects of the wind on nonlinearity via a windy coefficient. We demonstrate the numerical approach with examples consisting of tonal and broadband infrasound signals within several regions of the United States. The turbulent scattering effects are integrated into the solver as attenuation via a newly developed scattering coefficient, which is the major innovation of the presented approach.

To determine the turbulent scattering coefficient, a series of acoustic propagation experiments are conducted in the University of Florida Boundary Layer Wind Tunnel. A synthetic noise signal propagates through the UFBLWT to simulate infrasound propagation in the turbulent

atmosphere. The wind tunnel speed and roughness elements are varied to simulate different altitudes and terrains. The fluid dynamic and acoustic data are obtained by three Cobra probes and an inflow microphone-speaker acoustic system, respectively. The effect of turbulent attenuation on acoustic wave propagation is evaluated by analyzing the signal variation and turbulent statistics. The turbulent-acoustic interaction is observed as an attenuation effect. A new scattering model is modified based upon the experimental data and implemented into the numerical solver, which provides the generalized Burgers' equation solver with the capability of capturing the turbulent scattering effects. Therefore, the solver can capture the effects of refraction, nonlinearity, attenuation, dispersion, and turbulent scattering to precisely predict the infrasound propagation in the atmosphere.

CHAPTER 1 INTRODUCTION

1.1 Motivation

As a severe weather phenomenon with powerful destructive energy, tornadoes cause huge losses in life and property. Figure 1-1 is an aerial photo of the St. John's Regional Medical Center after a catastrophic tornado that struck Joplin, Missouri on May 22nd in 2011. The entire duration of this tornado was 34 minutes long, and the highest wind speed exceeded 200 miles per hour (mph). This deadly tornado flattened most of the city, caused 162 fatalities, 1150 injuries [1], and \$2.8 billion insured losses [2]. Along with the Joplin tornado, the tornadoes in 2011 killed 550



Figure 1-1. Aerial view of the St. John's Regional Medical Center campus; Photo courtesy of U.S. National Oceanic and Atmospheric Administration.

people and caused more than \$28 billion in property damage [3]. The United States contains the highest tornado-prone region, which is also well-known as “Tornado Alley”. The area defined by the term “Tornado Alley” is approximately located between the Rocky and Appalachian Mountains [4], extending from northern Texas, through Oklahoma, Kansas, Nebraska, Iowa, and South Dakota. On average, there are 800 tornadoes occurring in the United States every year, resulting in 80 deaths and 1500 injuries annually [5]. The state by state fatality rates are shown in Fig. 1-2, in which the southeastern United States is also a severely affected region [5].

A similar event is called tornado outbreak, which mainly happens in the “Tornado Alley” region. A tornado outbreak is usually caused by a synoptic scale weather system, which produces

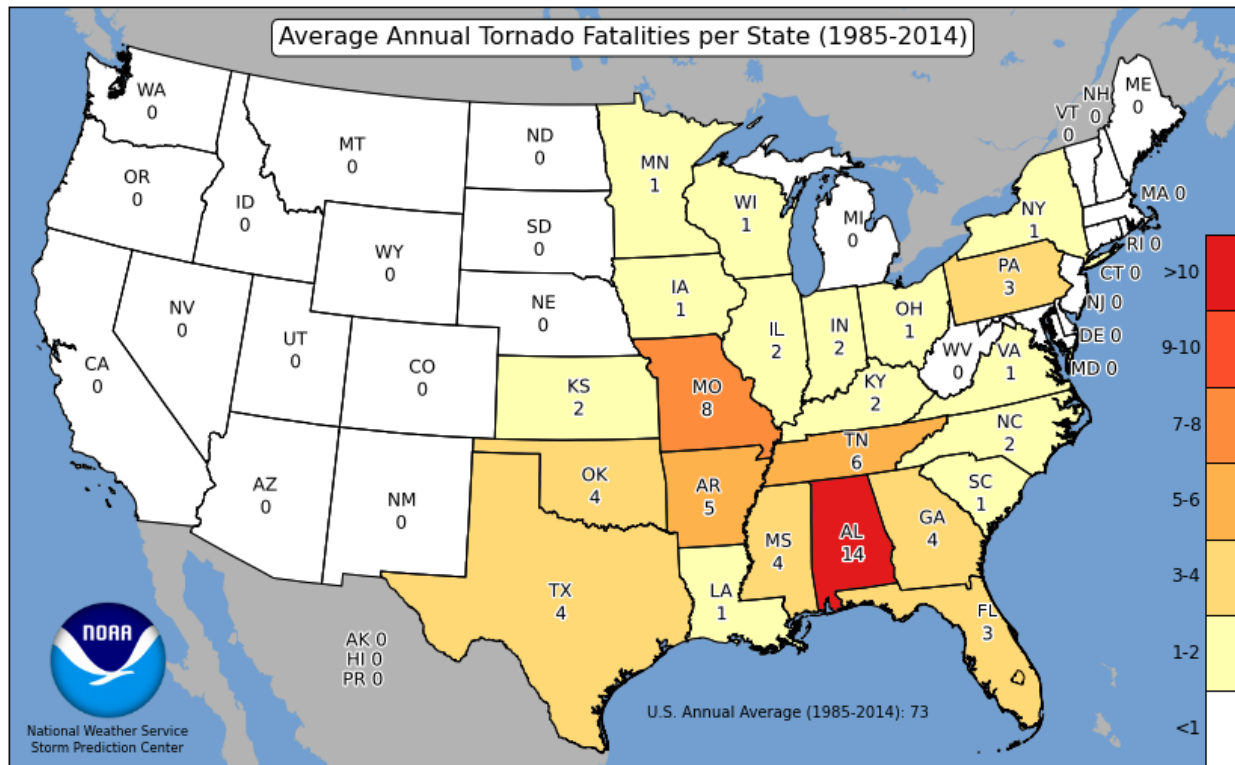


Figure 1-2. Annual average death rate from tornadoes; from U.S. National Oceanic and Atmospheric Administration.

multiple tornadoes within a short period of time (usually less than 24 hrs) [6]. In the last 50 years, there were more than 100 recorded tornado outbreaks that struck the United States. The following are particular statistics of four famous outbreaks. From April 3rd to April 4th in 1974, the “super outbreak”, generated 148 tornadoes, with 48 killer tornadoes resulting in 335 fatalities, and more than 6000 injuries [7]; On May 3rd in 1999, the Oklahoma–Kansas tornado outbreak formed 69 tornadoes, 10 of them were supercell tornadoes [8], resulting in 46 fatalities and 665 injuries; On April 27th in 2011, 199 tornadoes from another “super outbreak” killed 316 people and injured more than 2700 [9]; Recently, in 2020, the “Easter tornado outbreak” struck the United States on Easter Sunday and Monday, with a total number of 140 tornadoes hitting 10 states, which caused 32 fatalities. The statistics above demonstrate that the tornadoes or tornado outbreaks are deadly threats to life and property of people, which necessitates the continuous study of tornadoes and tornado prediction in the meteorology community. Recently, the acoustic characteristics of the

tornado caught researchers' attention as a potential tornado detection and formation prediction method.

1.2 Objective and Scope of Proposed Work

In this dissertation, the author presents an acoustic tornado prediction method by simulating the tornadic infrasound propagation with techniques including acoustic ray tracing, generalized Burgers' equation, turbulent scattering models, and wind tunnel experiments. The ultimate goal of the presented work is to achieve a fast-responding infrasound propagation simulation, which includes realistic effects of turbulence, to assist the construction of a real-time tornado warning system.

A numerical solver is developed to simulate tornadic infrasound propagation in the turbulent atmosphere. To obtain the accurate infrasound signal at an observer, the physical effects involving refraction, attenuation, dispersion, nonlinearity, and turbulent scattering are required to be modeled precisely. The acoustic ray tracing method of Gainville [10] is implemented in the numerical solver to capture the refraction effect. Atmospheric models are employed to simulate realistic temperature and wind profiles in atmosphere. To capture the effects of nonlinearity, attenuation, and dispersion, the generalized Burgers' equation is employed in the numerical solver.

To capture the turbulent scattering effect, an improved generalized Burgers' equation propagation method with an modified turbulent scattering model is developed, which is validated by a series of wind tunnel experiments. The turbulent-acoustic interaction is observed as an attenuation effect in the wind tunnel experiments. The turbulent statistics of the wind tunnel are measured and analyzed to modify the turbulent scattering attenuation model.

In this dissertation, both the numerical solver and the wind tunnel experiments are discussed. The major objectives are:

- **Improved Turbulent Scattering Model:** Introducing the turbulent effect into the generalized Burgers' equation is the major innovation of the solver. To capture the turbulent effects of the infrasound propagation, a new turbulent scattering model is improved from Ostashev's scattering model [11]. By bridging the scattering model with a turbulent

refraction model (see Section 2.4), the new model is developed and validated by the wind tunnel experiments.

- **Acoustic Ray Tracing with Meteorology Data Portal:** To capture the ray path connecting the tornado infrasound source and the observer, the acoustic ray tracing method is adapted from Gainville [10]. The computational domain of the acoustic ray tracing solver is capable of importing weather information, which allows the solver to read real-time temperature, humidity, and wind velocity data as input arguments. The grid system of this computational domain is demonstrated in Section 2.2.2, and two atmospheric models (HWM93 [12] and NRLMSISE-00 [13]) are employed to generate atmospheric parameters.
- **Modified Generalized Burgers' Equation Solver:** The generalized Burgers' equation is used to capture the effects of the nonlinearity, attenuation, and dispersion of the tornadic infrasound propagation. The generalized Burgers' equation solver is modified from Miller's [14] work. The turbulent scattering model is treated as attenuation and integrated into the generalized Burgers' equation (detailed derivation see Subsection 2.2.3).
- **Experimental Validation and Modification:** While there are many theories and models about the turbulent scattering effect [15, 16, 17, 18, 19], for long-range infrasound propagation, additional experiments are required to validate and modify our newly developed model and previous models. A unique acoustic propagation experiment is conducted at the University of Florida Boundary Layer Wind Tunnel (UFBLWT). Collected data is employed to validate and modify the turbulent scattering attenuation model. The experimental data is presented in Chapter 4.

The first three objectives listed above are integrated as a propagation solver for noise propagation from a tornado. By reading the real-time meteorology data, the solver is capable of calculating the arrival tornadic infrasonic waveform at monitor stations, which can be used as a tornado-formation evidence for the early warning system. Furthermore, the solver is capable of predicting other general acoustic propagation in turbulent medium, such as explosion infrasound and sonic boom propagation.

In the remaining portion of this chapter, related background information is introduced as follows. Section 1.3 is an introduction about current tornado damage rating and warning systems. Section 1.4 presents investigations about tornado infrasound. Section 1.5 introduces the physical effects during infrasound propagation. Section 1.6 discusses the numerical propagation models. Section 1.7 is a summary of atmospheric models. Section 1.8 outlines the structure of this dissertation and presents overviews about the content for each chapter.

1.3 Current Tornado Damage Rating and Warning System

To analyze the damage caused by a tornado, a damage rating system is required. In 1971, Dr. Tetsuya T. Fujita invented the Fujita scale rating system based on the peak wind speed of a tornado [20], which is also known as the F scale. The original F scale related the wind speed to the actual structural damage. For the F0 category, the peak wind speed is in the range from 40 to 72 mph, while the tornado-related damage is slight, such as broken tree branches and damaged sign boards. The F1 and F2 category tornadoes are capable of damaging the houses' structure with the peak wind speed in the range of 73 to 112 mph and 113 to 157 mph, respectively. When the F scale reaches F3, the tornado is considered severe. When the peak wind speed ranges from 158 to 206 mph, an F3 category tornado can tear off the roofs and some walls of a well-constructed house. The F4 category tornado can cause devastating damage with wind speed's range from 207 to 260 mph. Well-constructed houses can be leveled and cars can be lifted from the ground by an F4 tornado. The F5 category is the most intensive tornado within the F scale. With 261 to 318 mph winds, the F5 tornado can lift off house foundations and carry them for considerable distances. The F scale is widely used in the United States after Dr. Fujita invented it. However, there is an uncertain description: the well-constructed house. To make the rating system more accurate, the Fujita Scale Enhancement Project was conducted during 2000 to 2004 at the Wind Science and Engineering Research Center at Texas Tech. University [21], and officially released and implemented in the United States in 2007 [22]. Relative to the original Fujita scale, the Enhanced Fujita scale is constructed with a series of empirical investigations to determine the relation between the wind speed and the actual damage. Figure 1-3 is a virtual demonstration of the different EF scale's damage. During the super outbreak on April 27th in 2011, there were 19 EF3 (136–165 mph) tornadoes, 11 EF4 (166–200 mph) tornadoes, and 4 EF5 (> 200 mph) tornadoes. To avoid the damage by these devastating tornadoes, the timely tornado prediction is demanded by the public. This resulted in the investigation on the new method to forecast tornadoes since 1948 [23].

The tornado warning system is a complex chain of events [24] [25]. The complete



Figure 1-3. Gradations of damage ranging from EF0 (in upper-left corner) to EF5 (in lower-right corner). EF-scale ratings have been assigned to select one- and two-family houses; image courtesy of T. Marshall.

sequential steps of the entire warning system is started with tornado formation prediction, followed by detection, warning decision, dissemination, and public warning [26]. The prediction and detection play essential roles and initialize the reaction of the warning system.

Modeling with observational data is the mainstream method to predict tornado formation. With observational analysis and mesoscale numerical simulations, Egentowich et al. [27] successfully identified a series of dynamic precursors with 6 to 84 hours prior to a major tornado outbreak. As the computational technology advanced rapidly, high-resolution forecasts improved the prediction of severe weather [28]. With increasing frequency of tornado reports and data, machine learning technology is also used to forecast tornado formation [29].

Although numerical models [27, 28, 29] can predict a tornado in advance by approximately 24 hours, we still need to know when a tornado is initiated. The second step of the tornado

warning sequence, tornado detection, discovers the formation of the tornado by observing real-time meteorology information. Fortunately, with the development of the Doppler radar system, the tornado detection techniques have been developed significantly in the last century [25]. Certain characteristics of tornadoes were discovered with this new technology. In 1953, Stout and Huff [30] discovered the hook echoes, a tornadic-associated phenomenon, for the first time in their radar observation during an Illinois tornado outbreak. These hook echoes and associated rear-flank downdrafts were numerically simulated by Markowski [31]. Other features like horizontal wind shear also can be used as an early indicator of tornado formation [32]. To improve the radar coverage across the United States, the Weather Surveillance Radar-1988 Doppler network (WSR-88D) was constructed [33, 34]. Tornado detection algorithms based on WSR-88D were developed, like the WSR-88D mesocyclone detection algorithm (MDA) [35] and tornado detection algorithm (TDA) [36]. The MDA's performance for vortex detection and location were promising, while the TDA improved the probability of detection from 3% to 43%. Besides radar detection, reports from individuals in the field can be timely and critical. Programs like SKYWARN used trained "storm spotters" in the mid-1960s [23]. Similar programs have been useful for the tornado warning system, especially in the era of the Internet.

The tornado warning system has been greatly improved through the development of prediction models and detection techniques. The probability of detection has reached 90% [37] with current detection algorithms. However, there are some challenges for the current warning system. Prediction models rely on numerical simulations, where their consistency depends on the discretization technique and grid point spacing. For the prediction model, the computational domain and time-step size are directly related to the quality of the numerical simulation. To fully resolve the subgrid turbulence, the grid size must be within the order of 100 m [38], which is a liberal estimate as the smallest scale structures can be much smaller at lower altitudes. This implies an extremely expensive computational cost to model state-wide regional forecasts. Since most of the prediction models are designed for tornado outbreak forecast, there are few models for single tornado events, which make the accurate prediction of a single tornado hard to achieve.

Although current detection technology can provide the public with real-time tornado observations, the public still needs an earlier warning system to get prepared. By considering current challenges and public demand, the concept of the “warn on forecast” is invented by Stensrud et al. [39]. The goal of the “warn on forecast” system is to provide a zero-to-three-hours short-term warning system based on observational detection and real-time numerical models. To meet the requirements of the “warn on forecast,” perhaps acoustic features of tornado formation are the solutions to fill the blank of the final 3-hour warning in the system. The discovery of tornadic infrasound by Georges [40] is promising for the infrasound tornado prediction system. As a result of multiple findings in tornadic infrasound (see Section 1.4 for details), the Physical Sciences Division of the Earth Systems Laboratory and the National Weather Service Forecast Offices of the National Oceanic and Atmospheric Administration (NOAA) are working on an Infrasonic Network (IS Net) program to test the infrasound prediction method [41, 42, 43, 44, 45, 46]. With this IS Net, a potential warning system with the author’s prediction solver is feasible for this “warn on forecast” system.

1.4 Tornado Infrasound

In 1960s, the Geoacoustics Group of NOAA’s Wave Propagation Laboratory started investigating traveling low-frequency pressure variations related to thunderstorms and severe weather [47]. In 1968, Bowman [48] discovered the relation between a class of slow-traveling low-frequency barometric-pressure waves and severe weather phenomena, and he also concluded that those waves were associated with some strong convectonal severe weather in Washington DC. Bowman and Bedard [47] successfully measured the infrasonic pressure variations at the Earth’s surface using microphone arrays located at thousands of kilometres from the severe-weather disturbance in 1971. In 1973, Georges [40] reviewed previous research and confirmed the infrasound-severe weather relation with a case study of one storm, which was observed with both Doppler radar and an infrasonic microphone array.

In the 2000s, more evidence was discovered related to tornado infrasound. Akhalkatsi and Gogoberidze [49] characterized the tornadic infrasound through an equivalent source by using

Lighthill's acoustic analogy [50]. Schecter et al. [51] conducted numerical simulations of the adiabatic generation of infrasound by tornadoes, and Akhalkatsi and Gogoberidze [52] analyzed the spectrum of simulated infrasound sources related to a tornado. Besides numerical simulation of tornadic infrasound, acoustic observations of tornadoes (such as Elbing et al. [53] and Bedard [54]) presents more evidences regards to predicting tornadoes via acoustic detection. Based on recorded tornado noise, a mathematical model to represent the tornadic sound pattern was developed by Frazier et al. [55]. This mathematical model [55], and Markowski's [31] numerical simulation are employed by the author to generate the tornadic infrasound source signal.

1.5 Physical Effects in Acoustic Propagation

Once the tornado infrasound source is determined, the physical effects during noise propagation must be studied and modeled to predict the final received infrasound signal. The physical effects of long-range infrasound propagation are nonlinearity, attenuation, dispersion, refraction, and turbulent scattering. These effects are discussed in the following subsections.

1.5.1 Nonlinearity

The nonlinear effect is a phenomenon where the amplitude or the frequency of the pressure disturbances is high enough to affect the steepening of the disturbances [56]. Due to the nonlinearity, instead of the constant local speed of sound c , the propagation speed becomes

$$\frac{dx}{dt} = c \pm \beta u, \quad (1-1)$$

where $\frac{dx}{dt}$ is the total speed of the wave, x is the location of the wave front, c is the local speed of sound, u is the perturbation speed, β is the nonlinear coefficient, and is equal to $\frac{\gamma-1}{2} + 1$, where γ is the heat capacity ratio of the medium. The nonlinear coefficient, β , is dependent on the local heating and convection effects [57].

Due to the local convective effect, the acoustic wave is carried by fluid flows, which are already in motion caused by acoustic wave. The actual propagation speed is $c \propto u$. The local heating effect is shown in Fig. 1-4. The local temperature perturbation caused by the sine wave is shown as the black line. Since the speed of sound $c \propto \sqrt{T}$, and the gas at the peak of the waves is

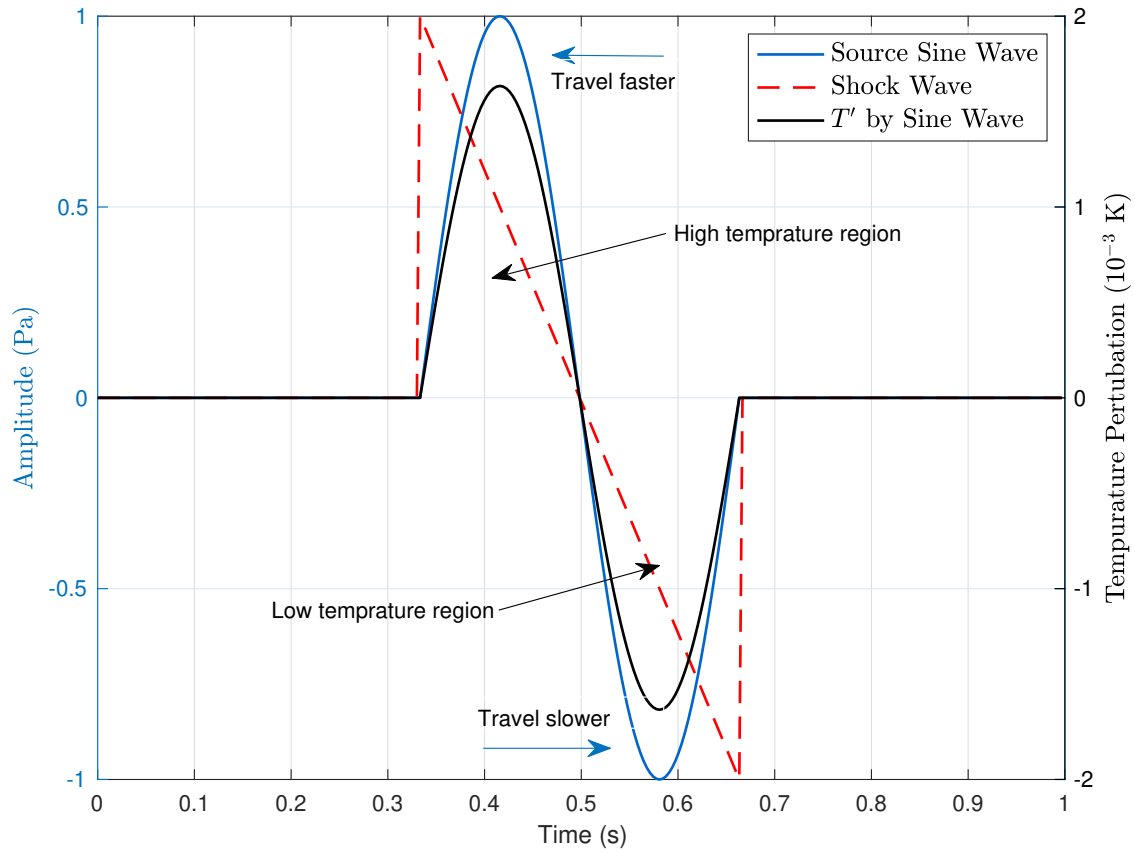


Figure 1-4. Nonlinearity caused by the local heating effect.

compressed and warmer than the ambient air, the speed of sound at the peak is the highest. Conversely, the speed of sound at a trough is the minimum. If the nonlinearity accumulates along the propagation path, the discontinuities will eventually be generated, which is also known as a shock wave as shown as the red dash line in Fig. 1-4. As a consequence of the nonlinear effects, a shock wave, or a “N” wave can be understood from the spectrum point of view as the generation of harmonics. The energy of the original frequency is transported into the harmonics, which makes the nonlinear distortion influence the amplitude of the “N” wave [10]. Besides the direct amplitude drop by distortion, an indirect attenuation is caused by the nonlinear effect because the higher frequency has stronger attenuation [58].

Nonlinear propagation is difficult to model because of the discontinuity. Direct Numerical Simulation (DNS) can model shock propagation by numerically solving the Navier-Stokes

equations with a shock capturing scheme. However, these techniques are extremely expensive in terms of computational resources. Sabatini et al. [59] simulated infrasound propagation with a three dimensional DNS with a grid point spacing of 90 m, and the calculation of a 200 km cubic domain cost 1600 s with 144 Nvidia M2090 T20A GPUs. To make the simulation faster, there are two mainstream approaches : nonlinear dominated strong shock theory and nonlinear corrected weak shock theory. The strong shock is validated for the cases with $p'/p_\infty > 1$ while the weak shock is validated for the cases with $p'/p_\infty \ll 1$, where the p' is the acoustic perturbation and p_∞ is the environmental pressure [56]. With the strong shock approach, Besset and Blanc [60] showed shock wave refraction due to the increasing stratospheric temperature, which were not captured by the linear acoustic theory. Baskar and Prasad [61] proposed an approach combining the strong shock and weak shock techniques to investigate sonic boom propagation. The strong shock approach mainly focuses on nonlinear refraction. However, for long-range infrasound propagation, the weak shock assumption is made and the nonlinear diffraction is ignored because of the geometric spreading. For weak shock propagation, the generalized Burgers' equation is able to accurately predict the propagation with effects of nonlinearity (See Section 1.5.1), absorption and dispersion (See Subsection 1.5.2), and geometric spreading. Besides the generalized Burgers' equation, the parabolic equation is also capable of capturing the nonlinear and diffraction effects [62]. A classic nonlinear parabolic propagation equation is the Khokhlov-Zabolotskaya-Kuznetsov (KZK) equation [63]. More details of the KZK are discussed in Section 1.6. The nonlinear infrasound research is often conducted for powerful explosion investigations [64, 65]. In Blanc and Rickel's [66] study, significant nonlinearities have been observed by a pulsed sounding experiment 38 km from a 4800-kg ammonium nitrate and fuel oil (ANFO) explosion.

For infrasound propagation, there are three major reasons to include the nonlinear effect in modeling. The first, the sources of the infrasound are usually powerful. The infrasonic sources in the atmosphere are always associated with the events such as nuclear explosions, powerful chemical explosions, volcanic eruptions, and supercell tornadoes. The acoustic power generated

by a tornado can reach the level of 10^7 watts [67]. The second, the propagation distance of the infrasound are long, usually in order of 100 km. As the nonlinear effects are cumulative with the propagation distance, the final received signal can be distorted heavily by the nonlinearity. Finally, the third, when the acoustic wave travels to high altitude regions, the density of air drops significantly, which amplifies the nonlinear effect, since u/c is larger with decreasing c [60].

1.5.2 Atmospheric Attenuation and Dispersion

Attenuation and dispersion are two key features that occur during infrasound propagation. Attenuation also can be modeled as atmospheric absorption, and changes both the energy and waveform of the infrasound. There are three mechanisms of atmospheric attenuation: classical absorption, molecular relaxation, and diffusion [68]. The classical absorption is caused by energy transfer from the kinetic energy of molecules in the sound wave to the random kinetic energy of the molecules in environment [68]. The relaxation is associated with the redistribution of translational or internal energy of the molecules. The relaxation can be divided into two absorption mechanisms: rotational absorption and vibrational absorption. The rotational absorption reflects the imbalance between rotational movements and translational movements, while the vibrational absorption is associated with the internal vibrations of the molecules [69]. The diffusion is caused by the mass and thermal diffusion, which generally is too small to be observed in measured data [68]. Sutherland and Bass [68] proposed a state-of-the-art model by integrating all the absorption mechanisms mentioned above. With this empirical model, the attenuation coefficient can be obtained up to an altitude of 160 km. As shown in Fig. 1-5, the absorption coefficient increases exponentially with rising altitude. In some extreme cases, the absorption difference in the stratosphere and thermosphere can lead to a mismatch between the simulated and observed results [71].

Besides absorption, dispersion is another physical phenomenon that occurs during acoustic propagation. Dispersion alters the propagation speed via the signal's frequency. This is unlikely to happen for lower (< 100 km) altitude atmospheric propagation with low frequency (< 10 Hz). However, when the frequency of the signal is high, and the molecular mean free path length is

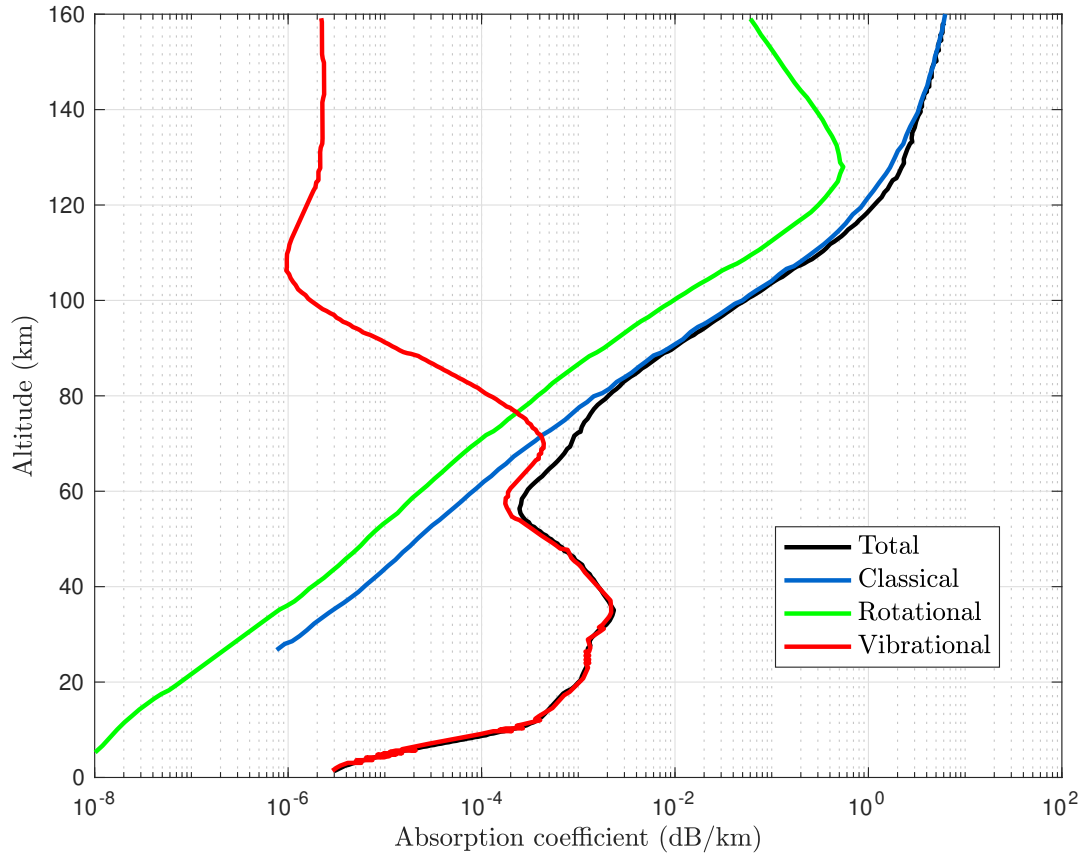


Figure 1-5. Example of total absorption coefficient at 0.4 Hz, with contributions from individual loss mechanisms shown separately [70].

large enough to make the Knudsen number approach 0.1, the dispersion mechanisms starts to increase the speed of the waves [58]. Figure 1-6 illustrates these altitude-dependent dispersion effects for different frequencies.

The absorption and dispersion mechanisms affect the wave form of the signal significantly, so a representative model of these mechanisms are essential to investigate the infraound propagation. Currently, the influence of dispersion on observed thermospheric signals is still an open research issue [70]. When dealing with high altitude acoustic propagation, the most popular and widely accepted choice to model these mechanisms is the Sutherland and Bass [68] model, which is employed in the present research.

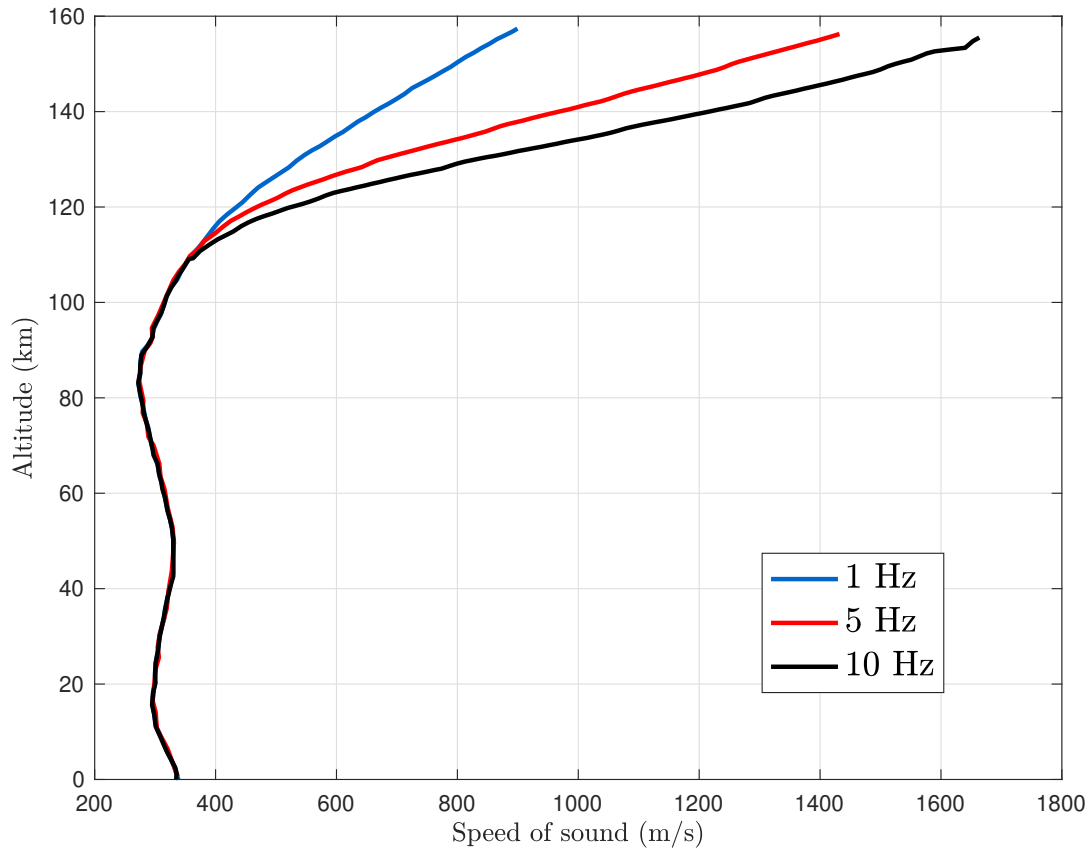


Figure 1-6. Static sound speed profiles that include the effects of dispersion over a range of frequencies.

1.5.3 Refraction and Shadow Zone

In geometric acoustics, a shadow zone is a well-known concept that defines regions where no acoustic ray passes [70]. The formation of the shadow zone is caused by refraction effects, which change the direction of the propagating wave front.

In ocean acoustics, acoustic refraction is investigated widely with the ray tracing method [72]. The refraction is caused by the vertical variation of the speed of sound, which is modeled by Snell's law [73]. In the 1990s, Dushaw et al. [74] discovered the shadow zone between a depth of 500 to 1000 m in the North Pacific, with a source located on Pioneer Seamount off the coast of California. Later in 2004, Uffelen et al. [75] confirmed the existence of the North Pacific shadow zone at ranges of 500 km and 1000 km from the source.

Sonic boom refraction and shadow zone studies started as early as in World War I, with the sonic boom generated by the gun shell [76]. As the supersonic aircraft was developed, the shock wave propagation in the atmosphere caught more attention. Guiraud [77] developed a model of the “N” wave propagation, which incorporates refraction in account with a moving nonuniform medium. With Guiraud’s [77] study, Hayes and Runyan [78] successfully implemented the model within a numerical solver. Friedman et al. [79] proposed a model to simulate the sonic boom atmospheric propagation with consideration of the refraction effect. In 1966, Maglieri et al. [80] investigated the atmospheric refraction effects on sonic boom propagation with experiments. Coulouvrat [81] proposed a nonlinear geometrical theory of diffraction to predict the sonic boom propagation in shadow zone. Today, the refraction and shadow zone research is a mature study, and multiple numerical solvers are able to capture these effect (see [82, 83, 84] as examples).

1.5.4 Turbulent Scattering

Similar to an acoustic wave, turbulence is another type of disturbance in fluids. The difference between these two disturbances is that the noise is a propagating compressive wave, while the turbulence is a rotational disturbance [85]. When the acoustic wave encounters turbulence, the spatial fluctuations of the speed of sound and the variation of the convection speed can refract the acoustic wave in other directions, which statistically, is the scattering phenomenon [86].

Ostashev and Wilson [15] developed an analytical model to simulate the propagation through an inhomogeneous anisotropic turbulent field with temperature and velocity fluctuations. Blanc-Benon et al. [16] implemented the model numerically with the KZK propagation equation and analyzed their results with experimental data. Lipkens [46] validated the model of Pierce [17] with sonic boom experiments by comparing the rise time of the mean waveform. Piacsek [87] investigated and validated the folding and focusing effect of the turbulence on sonic boom propagation by using Pierce [17]’s model. For sonic boom propagation, the distance of propagation is approximately 10 to 50 km, which is much smaller compared with the typical infrasound propagation distances. The performance of these models for long-range infrasound

propagation are not as satisfactory as for sonic boom propagation. The model of Goldreich and Kumar [18] simplified the turbulent scattering by using the mass and velocity of the turbulent structures to evaluate the turbulent scattering effect. Brown and Clifford [19] developed a turbulent scattering attenuation model by using the sound beam method. In the present model, the turbulent scattering is modeled by improving the Ostashev and Wilson's [11] model (see details in Section 2.3). The coefficient predicted by Lighthill's model [85] revealed that the acoustic-turbulent attenuation can be related to turbulent kinetic energy and length scale. In 1967, Tatarski [88] presented his turbulent scattering model, which was able to predict the directional scattering via a turbulent wavenumber spectrum. Ostashev and Wilson [11] improved Tatarski [88]'s model, which provided the model with the ability to capture the effect of inhomogeneous humidity. Our model leverages Ostashev and Wilson [11]'s model and incorporates a turbulent refraction model to account for the large-scale turbulent effects. Techniques from scattering theory [89] are employed to capture the dispersion coefficient.

1.6 Numerical Propagation Models

Long-range propagation of acoustic waves can be modeled via two major approaches, the parabolic equation method and the generalized Burgers' equation combined with acoustic ray tracing [70]. In this section, these two numerical techniques are introduced and compared.

One popular parabolic approach uses the KZK equation [90]. Blanc-Benon et al. [16] numerically evaluated the KZK equation to analyze the nonlinear distortion caused by the turbulence in the atmosphere. They found that high intensity turbulence can sufficiently enhance the nonlinear distortion. Stout et al. [91] showed how turbulence can affect an N-wave by analyzing the perceived level (PL) and the indoor sonic boom annoyance predictor metrics [92]. Aver'yanov et al. [93] investigated propagation in moving inhomogeneous media by using an extended KZK solver, which accounts for diffraction, nonlinearity, absorption, and scalar inhomogeneities. The parabolic equation method can capture phenomena caused by turbulence by solving the governing equation in the entire domain.

However, parabolic equation methods have some significant drawbacks. To resolve

turbulent effects, a computational domain with many grid points is required, which has considerable computational expense. Compared with the parabolic equation, the generalized Burgers' equation solves for the propagation along a one-dimensional ray path, which requires relatively less computational resources and can be applied to three-dimensional domains with the ray tracing [70]. Crighton [94] and Blackstock [95] described the generalized Burgers' equation, and how it is used to model nonlinear acoustic propagation. One successful numerical solver was developed by Saxena et al. [96] to solve the generalized Burgers' equation in the frequency domain. Lee et al. [97] improved the solver of Saxena et al. [96] by applying a Lanczos filter to eliminate the Gibbs' phenomenon. With this numerical generalized Burgers' equation solver, Miller [14] investigated nonlinear effects of propagating waves in the context of an acoustic analogy. In the present approach, the generalized Burgers' equation is modified with a turbulent scattering attenuation coefficient developed from Ostashev's [11] model. The detailed derivation is shown in the Chapter 2.

Acoustic ray tracing is widely used in underwater [98], architectural, and atmospheric acoustics. The wind speed in the atmosphere at high altitude can easily reach 80 m/s. This alters the propagation characteristics of the infrasound from tornadoes relative to a quiescent atmosphere. The effect is non-negligible for weather detection. Thus, a numerical ray tracing method in the moving medium was developed by Hallberg et al. [82]. A general expression of ray-acoustic intensity is derived by Thompson [83, 84]. In PCBoom, the ray tracing method was implemented to successfully capture atmospheric effects on noise propagation by Plotkin et al. [99].

Prediction of sound propagation through the atmosphere is highly dependent on the choice of the atmospheric model. Refraction, attenuation, dispersion, and diffraction are considered as major atmospheric effects for acoustic propagation [70]. By treating the atmosphere as a multilayer medium, Pierces and Rad [100] showed that stratified wind and temperature causes refraction. Attenuation and dispersion can be captured by employing atmospheric models such as Sutherland and Bass [68] and Bass et al. [101]. The nonlinear and attenuation effects at high

altitude were studied by Lonzaga et al. [102]. Averiyarov et al. [103] investigated diffraction with a two-dimensional generalized KZK solver. Their results showed that the turbulent-related diffraction phenomenon increases the mean shock rise time by almost 100%. Other factors such as ground effects must be incorporated within the solver. We use the approach of Aumann et al. [104] to integrate ground effects within the solver.

1.7 Atmospheric Models

1.7.0.1 Atmospheric Profiles

To analyze the atmospheric effects on the propagation, the profiles of the atmospheric parameters, like wind speed, temperature, density, humidity, and volume fraction of the air components, are necessary for the modelling of the nonlinearity, refraction, attenuation, and dispersion effects. Drob et al. [12] developed the Horizontal Wind Model (HWM) that can represent the mean horizontal wind speed at any location on Earth, which includes the velocity vector. To obtain the local speed of sound along the ray path, local temperature and density are required. NRLMSISE-00 model of Picone et al [13] is capable of simulating the density and temperature of the atmosphere. Both HWM93 [12] and NRLMSISE-00 [13] models are employed in present approach to generate the weather information in the propagation domain.

1.7.0.2 Turbulence in the Atmosphere

As the scattering caused by turbulence will be modeled as an attenuation effect for long range acoustic propagation, it is necessary to investigate the distribution of turbulence within the atmosphere. Methodologically, the atmosphere consists of the troposphere, stratosphere, mesosphere, and thermosphere. For acoustic propagation, we focus on the altitudes under 160 km, where the turbulence distributions can be considered within four different regions: 0 - 5 km, 5 - 10 km, 10 - 20 km, and above 20 km. We will discuss these regions separately. At the end of this section, the turbulent model used in the present approach is introduced.

Below the altitude of 5 km is the region called the atmospheric boundary layer (ABL), which is widely studied in the meteorology and atmospheric science fields. The depth of the ABL varies depending on terrains. Usually, the ceiling of the ABL is approximately one to two

kilometers high [105]. At extreme conditions, such as a mid-summer day in the desert, the height of the ABL can be 5 km [106]. At the top of the ABL is the inertial layer where the flow is considered as a free-stream. The thickness of the inertial layer is around 20 – 50% of the mean depth of the ABL [105]. Under the inertial layer, the characteristics of the boundary layer flow shifts between the daytime and the night time. During the daytime, the sun-heated ground generates a convective boundary layer (CBL). There is significant vertical velocity inside the CBL, which contributes to entrainment that cannot be ignored when analysing the CBL turbulence. As the consumption of the turbulent kinetic energy (TKE) due to the CBL entrainment should be a fixed portion of the production of the TKE due to CBL entrainment. VanZanten et al. [107] conducted a parameterization study to ascertain the TKE consumption-production ratio by using a large eddy simulation (LES). Their results show that the mean ratios of the consumption to production of TKE for the clear, smoked, and cloud-topped CBL are identical, and the ratio is 0.43. After sunset, a thin nocturnal boundary layer named the Neutral Boundary Layer (NBL) replace the CBL between altitudes of 0 to 400 m. Deardorff [108] investigated the NBL stability and heat flux to analyze the turbulence characterization. The “eddy tilts,” defined as the inclination from the vertical of the locations of the maximum turbulent velocity isotachs’ curvature are observed. The horizontal component eddies were seen tilting about 80° relative to the vertical direction, while the vertical component eddies tilted 60° on average from the near ground to the top of the NBL.

Within the altitude interval of 5 km - 10 km, the turbulence is considered as the free troposphere turbulence. Methods like flight measurements [109][110], radar techniques [111], and even stellar scintillation [112] are used to characterize the turbulence within this region. A milestone of flight measurements called the turbulent air motion measurement system (TAMMS), was reached in 1996 by Barrick et al. [109]. The TAMMS was integrated into a Lockheed 188 Electra airplane (designated NASA 429) and calibrated with the tower flyby method and remote flight maneuvers. Later in 2003, with a TAMMS instrumented P-3B airplane platform, Cho et al. [110] collected and analyzed a dataset for the troposphere turbulence above the Pacific ocean area

from 15°N to 45°N, with altitudes up to 8 km. They found that in the free troposphere, the ratio of shear-produced turbulence to convective turbulence increased from roughly 2:1 for weak turbulence to 3:1 for strong turbulence, while the ratio is about 1:1 for weak turbulence and 2:1 for strong turbulence in the CBL. Cohn [111] studied the turbulent eddy dissipation rate with two independent radar measurements, and similar shapes and profiles of the dissipation rate were found. The mean dissipation rate decreases exponentially from approximately $1 \text{ m}^2/\text{s}^3$ at 4 km to the order of $10^{-4} \text{ m}^2/\text{s}^3$ at 8 km, while a slight increment to approximately $10^{-3} \text{ m}^2/\text{s}^3$ appeared when the altitude increases from 8 km to 10 km. The method of Azouit and Vernin [112] is another interesting technique that employed stellar scintillation data to analyze the turbulence. They conducted a two-dimensional analysis on the turbulence strength relation to a double-star scintillation. A turbulent layer observed at approximately 9 km high is considered as a Kelvin-Helmholtz billow with the crest-trough amplitude about 600 m.

For the altitude range of 10 to 20 km, the gravity waves become a source of the turbulent motion residing in the upper troposphere and lower stratosphere zone. Lindgren et al. [113] studied the seasonal lower stratosphere gravity wave for different latitudinal regions with high altitude balloons. The annual variation of gravity waves induced TKE is obtained at 75 hPa pressure altitude. For the zero degree latitude, the maximum velocity oscillation is $5 \times 10^{-5} \text{ m}^2\text{s}^{-2}/(\text{cycles}/\text{day})$ for 5-mins records and $3 \times 10^{-2} \text{ m}^2\text{s}^{-2}/(\text{cycles}/\text{day})$ for 3-hrs records. Bacmeister et al. [114] investigates the turbulence near at an altitude of 20 km with 73 ER-2 airplane flights. The velocity and temperature spectrum were obtained with the wavelength range from 100 m to 1 km. The results show that for a wave length smaller than 3 km, the steeper spectra with -3 power law was found rather than the standard -5/3 power law. Lilly and Lester [115] also investigated the turbulence at an altitude from 13 km to 20 km with two instrumented RB-57F airplanes. Their measurements of velocity and temperature variations and covariances agreed with preliminary predictions of gravity wave theory. They also observed mountainous-terrain-generated gravity waves, which are observed with wave length between twenty and thirty kilometers.

Studies of turbulence above 20 km heavily rely on radar data. The turbulence within the upper-stratosphere and mesosphere is not continuously distributed in the vertical direction. Instead, the turbulent layer is the major form of the turbulence in this region. Woodman and Guillen [116] investigated the turbulent layers at altitude ranges of 10 to 35 km and 50 to 85 km with their real time Doppler radar observations. By analysing the power level and spectral width, they concluded that the turbulent layer thickness is of the order of 100 m. The velocity fluctuations induced by the gravity waves are approximately 10 m/s for the horizontal component and approximately 1 m/s for the vertical component. Large scale research on high altitude turbulence is also discussed by Gage and Balsley [117], using the mesosphere-stratosphere-troposphere (MST) radar technique. Through their investigation, the Kolmogorov scale is observed to increase from 0.1 m to 1 km with the altitudes from 20 km to 50 km.

At an altitude of 50 km, the Kolmogorov scale of turbulence reaches 1 km [117], so the effect of turbulence on acoustic propagation is mainly through refraction effects rather than scattering effects. Thus, we will not account for turbulence and its effect on the acoustic propagation above an altitude of 50 km. From a long range acoustic propagation perspective, the detailed ABL model with CBL and NBL is hard to implement at a large scale., while the turbulence in the upper-troposphere and lower-stratosphere zones are significant for the infrasound propagation and considerably simple to be modeled. As the frequency of the gravity wave is significantly lower than the acoustic wave, the effect of the gravity wave on acoustic propagation is negligible. With the conditions and assumptions discussed above, we use an atmospheric turbulent model from Lukin [118] to simulate turbulence for altitudes from 0 to 20 km. From 20 km to 50 km, the turbulence can be modeled as a sparse scattered layer with approximately 100 m thickness. Therefore, we use exponential decay models to represent the turbulence in this region. The detailed turbulence model in the present approach is discussed in Section 2.4.

1.8 Structure of the Dissertation

Chapter II: Methodology: In this chapter, the derivation and implementation of the acoustic ray tracing model, generalized Burgers' equation, and the turbulent scattering models are introduced. Acoustic ray tracing is combined with two atmospheric models (HWM [12] and NRLMSISE [13]). The generalized Burgers' equation is solved via the Fourier Galerkin method in the frequency domain. To account for the geometric effect on the nonlinearity, a geodisc element coefficient is applied to the nonlinear term in the generalized Burgers' equation. The Lighthill's turbulent scattering attenuation model is introduced in the Section 2.3, along with the modification based on the directional study of Ostashev and Wilson [15]. Finally, the experimental techniques employed in the UFBLWT test are presented.

Chapter III: Preliminary Results the Numerical Solver: The preliminary numerical results of the prediction solver are presented in Chapter 3.2. The validation of the numerical propagation solver is conducted to ascertain the effects of refraction, nonlinearity, and attenuation. Infrasonic propagation simulations are presented with both harmonic wave and broadband tornadic infrasound source signals.

Chapter IV: Experimental Results: For the wind tunnel experiments, the acoustic characterization of the wind tunnel is demonstrated, along with the source signal design. The acoustic propagation test results are demonstrated, along with post processing methods. Turbulent statistics are collected in the UFBLWT and analyzed to validate the turbulent scattering attenuation model. Finally, the preliminary results of the turbulent-acoustic interaction are presented based on the UFBLWT experiments.

Chapter V: Validation, Sensitivity, Numerical Analysis of the Bridging Model: The newly developed bridging model is validated by the UFBLWT experiments and investigated by a series of numerical tests. The model's sensitivity and model-embedded solver's sensitivity are analyzed in this chapter. A tornadic infrasound signal is employed for the study of the model on the overall sound pressure level. The application of the solver with a realistic atmosphere is also presented.

Chapter VI: Conclusion and Summary This chapter summarizes the content of dissertation and presents the conclusion of the research.

CHAPTER 2 NUMERICAL AND EXPERIMENTAL TECHNIQUES

In this chapter, three major techniques employed in the propagation solver development are introduced: the acoustic ray tracing, the generalized Burgers' equation with modified coefficients, and the turbulent scattering models. The flowchart of the the entire numerical solver is shown in Fig. 2-1, along with the techniques employed in the solver development. In Fig. 2-1, the column

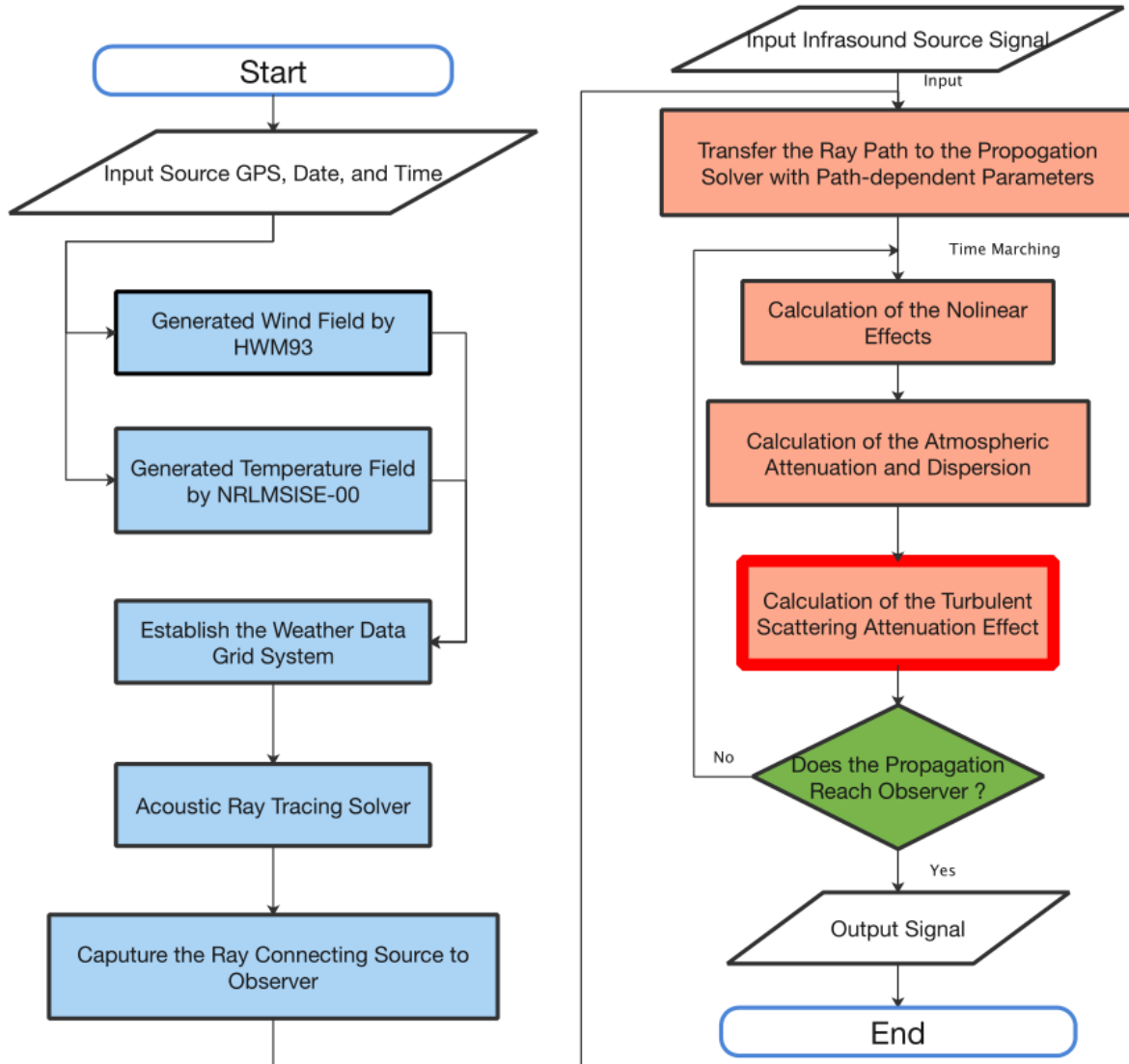


Figure 2-1. Flowchart of the numerical solver and techniques used in the solver.

with blue color on the left is the acoustic ray tracing solver, while column with red color on the right is the generalized Burgers' equation solver.

The acoustic ray tracing method from Gainville [10] is employed to find all ray paths

connecting the source and observer. These rays represent a series of one-dimensional propagation paths through the three-dimensional atmosphere. The atmosphere is modeled by the HWM93 [12] and NRLMSISE-00 [13] to construct a computational domain for the ray tracing solver. We then apply the geodisc element method [10] as a bridge to connect the ray tracing solver and generalized Burgers' equation solver. The results of the geodisc elements solver are arguments of the generalized Burgers' equation solver as a function along each ray path. We then superimpose all solutions of the generalized Burgers' equation to predict the total acoustic signal at the observer.

Along with the generalized Burgers' equation propagation solver, an improved turbulent scattering model is also employed to account for the acoustic-turbulent interaction. Because of the long propagation distance, the scattered acoustic waves are no longer significant to the final received signal. Therefore, we treat the effect of the turbulence as a type of attenuation. By collecting the path-dependent turbulent statistics (length scale and turbulent kinetic energy (TKE)) along the ray path, the propagation solver is capable of capturing the turbulent scattering attenuation. We also introduce the Tartaski's turbulent scattering model [88] (improved by Ostashev and Wilson [15]) and Lighthill's [85] model in this chapter. Both models are discussed in this chapter with detailed derivation. By bridging the turbulent refraction and scattering, a new model is developed with a correction coefficient (see Section 2.6 for detail).

Experimental techniques are also used to modify and validate the newly developed turbulent scattering model. A series of turbulent boundary layer wind tunnel experiments are conducted to analyze the turbulent effect on the acoustic propagation and to modify the turbulent scattering models. The experimental setup of these tests are introduced in Chapter 4.

With all these techniques, a propagation solver based on the generalized Burgers' equation and turbulent scattering models is developed to predict the infrasound propagation in the turbulent atmospheric boundary layer. The solver is also capable of simulating other acoustic propagation problems like sonic boom and explosion infrasound propagation.

2.1 Acoustic Ray Tracing

In this section, the equations for the numerical ray tracing solver are introduced. In most situations, the ray tracing method is only valid for high frequency (small wave length) problems [98]. However, in our case, the propagation length (more than 100 km) is long relative to the acoustic wavelength (in order of 100 m), thus ray theory is appropriate for the long-range infrasound propagation [70]. We use an infinite number of rays to represent the propagation path of the acoustic waves, and we track the rays to ascertain their propagation path. We find multiple trajectories generated by advancing wave fronts, and these trajectories are the rays used by the propagation solver. These equations are developed through use of differential geometry [119]. The first is the equation that describes the wave front location \mathbf{X} [10]

$$\frac{d\mathbf{X}}{dt} = c \cdot \mathbf{N} + \mathbf{u} = \mathbf{c}_g, \quad (2-1)$$

where c is local speed of sound, \mathbf{N} is the unity normal vector of the wave front and is equal to $\mathbf{K}K^{-1}$, \mathbf{K} is the wave vector, t is time, and \mathbf{u} is local wind speed. Our objective is to predict how refraction alters the wave vector. We take the material derivative of the wave vector and find

$$\frac{d\mathbf{K}}{dt} = \frac{\partial \mathbf{K}}{\partial t} + (\mathbf{c}_g \cdot \nabla) \mathbf{K}. \quad (2-2)$$

We then use the dispersion relation [86] to find the local derivative,

$$\frac{\partial \mathbf{K}}{\partial t} = -\nabla (\mathbf{c}_g \cdot \mathbf{K}) = -\nabla (\mathbf{c}_g) \cdot \mathbf{K} - (\nabla \mathbf{K}) \cdot \mathbf{c}_g. \quad (2-3)$$

The last term in Eqn. 2-3 is expanded as

$$(\nabla \mathbf{K}) \cdot \mathbf{c}_g = (\mathbf{c}_g \cdot \nabla) \mathbf{K} + \mathbf{c}_g \wedge \nabla \wedge \mathbf{K} = \nabla (\mathbf{c}_g) \cdot \mathbf{K}, \quad (2-4)$$

where \wedge is the cross product. Simplifying Eqns. 2-2 by applying Eqns. 2-3 and 2-4, we find,

$$\frac{d\mathbf{K}}{dt} = -\nabla \mathbf{c}_g \cdot \mathbf{K} = -K \nabla c - \nabla \mathbf{u} \cdot \mathbf{K}. \quad (2-5)$$

Finally, we use the relation $\mathbf{K} = K \cdot \mathbf{N}$ to obtain the wave front

$$\frac{d\mathbf{N}}{dt} = \frac{1}{K} \left(\frac{d\mathbf{K}}{dt} - \left(\mathbf{N} \cdot \frac{d\mathbf{K}}{dt} \right) \mathbf{N} \right). \quad (2-6)$$

Equations 2-1, 2-5, and 2-6 are the governing equations for the acoustic ray tracing solver. For our problem, c_g varies due to the variation of the speed of sound, c , and wind speed, \mathbf{u} , which is the horizontal component of wind velocity and causes refraction.

2.2 Propagation Models and Scheme

2.2.1 Geodisc Elements and Convective Volume

The volume dependent parameters of the rays are non-existent because we reduced our propagation problem to one dimension. In this section, we introduce the geodisc element method and convective volume to overcome this limitation (see Gainville [10] for detail). First, we introduce the concept of the ray tube. A ray tube is formed by a central ray's surrounding rays. The shape of ray tubes are influenced by the wind condition and local speed of sound. The effects of winds in the atmosphere twist and bend the ray tubes. One example of a ray tube is shown in Fig. 2-2, where the cross-section of a ray tube is constructed by vectors \mathbf{X}_1 and \mathbf{X}_2 . These three

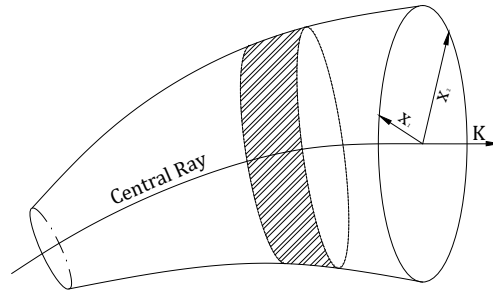


Figure 2-2. Ray tube and convective volume.

vectors (\mathbf{X}_1 , \mathbf{X}_2 and \mathbf{K}) construct the convective volume, which is defined as

$$v = \frac{|\mathbf{X}_1 \wedge \mathbf{X}_2|}{|\mathbf{K}|} = \frac{|\mathbf{X}_1 \wedge \mathbf{X}_2| \cdot \lambda}{2\pi}, \quad (2-7)$$

where v is convective volume and λ is wave length. The shadowed section in Fig. 2-2 is an example of a convective volume. X_i is governed by

$$\frac{d\mathbf{X}_i}{dt} = (\mathbf{X}_i \cdot \nabla c) \mathbf{N} + (\mathbf{X}_i \cdot \nabla) \mathbf{u} + c \mathbf{N}_i, \quad (2-8)$$

and

$$\frac{d\mathbf{N}_i}{dt} = (\mathbf{N} \cdot \mathbf{V}_r) \mathbf{N}_i + (\mathbf{N}_i \cdot \mathbf{V}_r) \mathbf{N} - (\mathbf{V}_{ri} - (\mathbf{N} \cdot \mathbf{V}_{pi}) \mathbf{N}), \quad (2-9)$$

where \mathbf{V}_r and \mathbf{V}_{ri} are

$$\mathbf{V}_r = \nabla c + \nabla \cdot \mathbf{N}, \quad (2-10)$$

and

$$\mathbf{V}_{ri} = \nabla \mathbf{u} \cdot \mathbf{N}_i + \mathbf{X}_i \cdot \nabla \nabla \mathbf{u} \cdot \mathbf{N} + \mathbf{X}_i \cdot \nabla \nabla c. \quad (2-11)$$

The subscript of \mathbf{X}_i and \mathbf{N}_i denotes the local coordinate system of the convective volume. We calculate the convective volume using Eqns. 2-8 and 2-9.

2.2.2 Discrete System and Atmosphere Model

We use a discrete grid system to store weather conditions within the propagation solver. The data storage system is shown in Fig. 2-3. The blue dashed lines represent the grid, and all atmospheric data is located at the red nodes. The black dot within the black cell is an example location of the current wave front. The green data nodes are used for the wave vector calculation. The \underline{X} , \underline{Y} , and \underline{Z} are the local coordinates of current wave front. We obtain the wave front point via its coordinates, which are dependent on the local cell. By using a second order b-spline interpolation, we obtain the interpolated wind speed, local speed of sound, and temperature at the wave front. Then we apply these parameters to the governing equations (Eqns. 2-8 and 2-9) to obtain the convective volume.

We model the atmosphere as an ideal gas and use the models HWM93 [120] and NRLMSISE-00 [121] for horizontal wind and temperature variations. These models are useful for the prediction of wind velocities and temperature variation in areas relevant to infrasound propagation from tornadoes. One example of the modeled wind and temperature profiles are

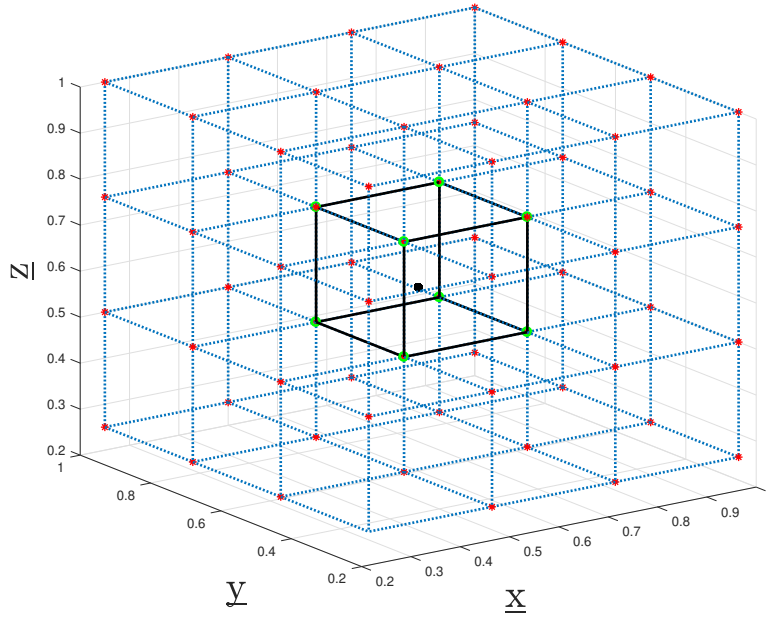


Figure 2-3. Grid system and interpolation method.

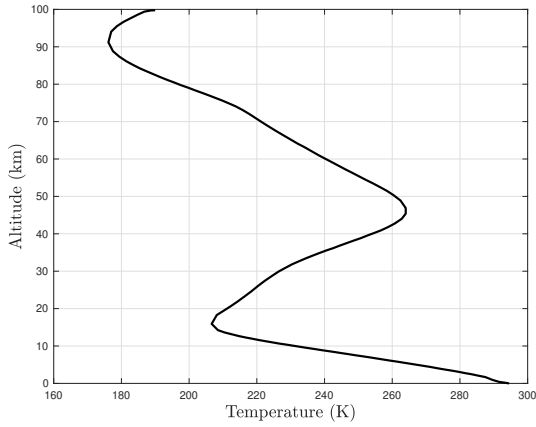
shown in Fig. 2-4. The profiles are obtained at longitude: -82.3248262° W and latitude: 29.6516344° N. The the westward latitude wind and northward longitude wind are captured for this location.

2.2.3 Generalized Burgers' Equation

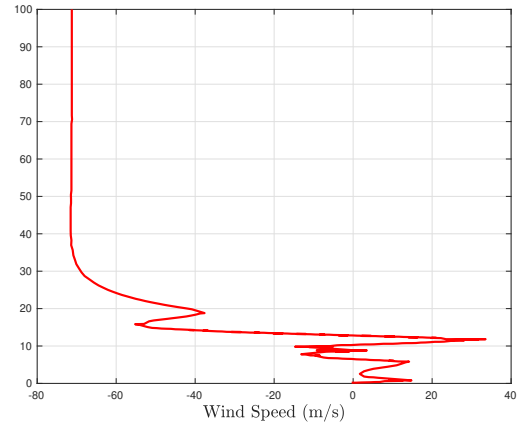
By performing an asymptotic analysis on the Navier-Stokes equation (see details in the work of Scott et al. [122]), the density perturbation about the mean turbulent atmosphere within ray tubes is

$$\begin{aligned} & \left(\frac{\rho}{c}\right)^{\frac{1}{2}} \left(\frac{\partial}{\partial t} + \mathbf{c}_g \cdot \nabla\right) \left(\frac{c}{\rho}\right)^{\frac{1}{2}} \rho' + \frac{1}{2} (\nabla \cdot \mathbf{c}_g + \mathbf{n} \cdot (\mathbf{n} \cdot \nabla) \mathbf{c}_g) \rho' \\ &= -\frac{c}{\rho} k_\phi \left(\frac{1+\gamma}{2}\right) \rho' \frac{\partial \rho'}{\partial \eta} + \varepsilon^{-2} \delta k_\phi^2 \frac{\partial^2 \rho'}{\partial \eta^2} + \frac{k_\phi}{2cT} \frac{\partial p}{\partial s} \Big|_0 \sum_{\alpha} \varepsilon^{-1} c_{v\alpha} \frac{\partial T'_{\alpha 1}}{\partial \eta}, \end{aligned} \quad (2-12)$$

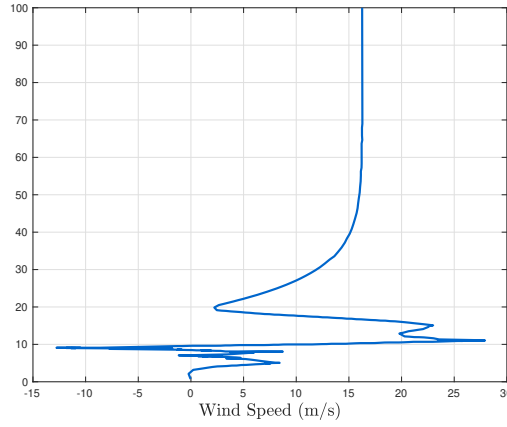
where ρ' is the acoustic density perturbation, k_ϕ is the gradient of velocity potential, η is the scaled length variable ($\eta = \frac{\xi}{\varepsilon}$), ε is the magnitude scale factor, ξ is the length along the ray, δ is thermal viscosity, subscript α represents components of the air, $c_{v\alpha}$ is constant volume specific



(a) *Temperature*



(b) *Latitude wind*



(c) *Longitude wind*

Figure 2-4. Wind speed and temperature profiles at longitude: -82.3248262° W and latitude: 29.6516344° N.

heat capacity of the component α , T is local temperature, and T'_α is the temperature perturbation of the component α . The left hand-side terms represent the propagation of the density perturbation in a moving temperature-varying medium. The first term on the right hand-side is the nonlinear effect, the second term is the absorption effect, and the third term is the dispersion effect.

To simplify Eqn. 2-12, Scott et al. [122] normalize the density perturbation ρ' as an acoustic pressure perturbation $p = \left(\frac{K\rho}{vc}\right)^{\frac{1}{2}} \epsilon \rho'$, which we informally call the term $\left(\frac{K\rho}{vc}\right)^{\frac{1}{2}}$ the “windy-coefficient,” which is

$$\mathcal{W} = \left(\frac{K\rho}{\nu c} \right)^{\frac{1}{2}}. \quad (2-13)$$

We simplify Eqn. 2-12 with the acoustic pressure perturbation and obtain

$$\frac{\partial p}{\partial t} = \delta K^2 \frac{\partial^2 p}{\partial \xi^2} + BKp \frac{\partial p}{\partial \xi} + K \sum_{\alpha} (\Delta c)_{\alpha} \frac{\partial p_{\alpha}}{\partial \xi}, \quad (2-14)$$

where Δc_{α} is the difference of the speed of sound between component α and the ambient speed of sound. The nonlinear coefficient B is

$$B = \mathcal{W} \left(\frac{1+\gamma}{2} \right). \quad (2-15)$$

Equation 2-14 is one-dimensional propagation equation. The term on the left hand side is the partial time derivative of the acoustic pressure signal. The terms on the right hand side are attenuation, nonlinearity, and dispersion, respectively. By using the Fourier Galkerin spectral method (see Blackburn and Sherwin [123] for details), we solve Eqn. 2-14 in the frequency domain while matching points along the previously predicted rays for a time marching scheme.

$$\phi_n(\xi) = e^{2\pi i n \xi / \Xi}, \quad (2-16)$$

where Ξ is wave length. Then we obtain an approximation equation with variable p^M as

$$p^M(\xi, t) = \sum_{n=-\frac{M}{2}}^{\frac{M}{2}-1} \tilde{p}_n(t) \phi_n(\xi), \quad M = 0, \pm 1, \pm 2, \dots \quad (2-17)$$

By implementing Eqn. 2-17 into the Eqn. 2-14, the integral over the wavelength is

$$\frac{1}{\Xi} \int_0^{\Xi} \left(\frac{\partial p^M}{\partial t} - \delta K^2 \frac{\partial^2 p^M}{\partial \xi^2} + K \frac{B}{2} \frac{\partial (p^M)^2}{\partial \xi} + K \sum_{\alpha} (\Delta c)_{\alpha} \frac{\partial p_{\alpha}}{\partial \xi} \right) \phi_n(\xi) d\xi = 0, \quad M = 0, \pm 1, \pm 2, \dots \quad (2-18)$$

then the Eqn. 2-18 can be solved on frequency domain as

$$\frac{\partial \tilde{p}}{\partial t} = -\Gamma \tilde{p} + i \frac{1}{2} B (\tilde{p})^2, \quad (2-19)$$

where we assemble attenuation and dispersion terms with the combined coefficient Γ as

$$\Gamma = \delta K^2 q^2 + iKq \sum_{\alpha} \frac{(\Delta c_{\alpha})}{1 - iKq\tau_{\alpha}c} . \quad (2-20)$$

Currently we use the model of Sutherland and Bass [68] to generate the dispersion and attenuation coefficients. With the RK2 time marching scheme, the wind conditions and temperature distribution, and the convective volume from the geodisc elements method, we predict the acoustic propagation by applying the generalized Burgers' equation along each ray from source to observer.

Although the generalized Burgers' equation and acoustic ray tracing are able to capture the nonlinearity, attenuation, dispersion, and refraction, there is another important effect for long-range propagation, which is the effect of atmospheric turbulence. In the following section, this turbulent effect is discussed by analyzing scattering by turbulent structures.

2.3 Lighthill's Scattering Models

The interaction between the acoustic wave and turbulence causes some radiated waves at an angle relative to the incident wave, which is known as scattering. Lighthill [85] studied the scattering effect with his acoustic analogy [50]. By combining the incident wave with the fluid field, the first approximation to the turbulent-acoustic coupled instantaneous quadrupole with strength per unit volume is

$$\rho (v_i + V_i) (v_j + V_j) = \rho v_i v_j + \rho V_i V_j + \rho (v_i V_j + v_j V_i) , \quad (2-21)$$

where ρ is the local density, V is the incident wave speed, and v is the instantaneous flow-field that the sound wave incident upon. In Eqn. 2-21, the three terms on the right-hand-side represent different mechanisms of quadrupoles, respectively: the first term represents the quadrupole of the sound already generated by the turbulence regardless to the incident wave; the second term is responsible for the wave form deformation due to the incident wave's finite amplitude; the third term, also known as the scattering quadrupole, is responsible for the interaction between the incident wave and the turbulent structure.

By dividing the instantaneous velocity v into mean velocity and turbulent velocity, the scattering quadrupole is split into two parts: the refraction wave by the mean flow as $\rho_0 (\bar{v}_i V_j + \bar{v}_j V_i)$ and the turbulent scattering part as $\rho_0 (v'_i V_j + v'_j V_i)$. For a plane harmonic incident wave, the V_i is

$$V_i = A_0 c \cos[\kappa(x_1 - ct)] \delta_{i1}, \quad (2-22)$$

where A_0 is the amplitude of the incident wave, κ is the wave number, and x_1 is the propagation direction. By applying Eqn. 2-22 into $\rho (v'_i V_j + v'_j V_i)$, the quadrupole due to turbulent velocity's fluctuation is

$$\rho_0 A_0 c \cos[\kappa(x_1 - ct)] (v'_i \delta_{j1} + v'_j \delta_{i1}). \quad (2-23)$$

On a unit volume basis, we apply this quadrupole into the Lighthill's [50] acoustic analogy given by

$$\rho - \rho_0 \sim \frac{1}{4\pi c^4} \frac{x_i x_j}{x^3} \int \frac{\partial^2}{\partial t^2} T_{ij} \left(\mathbf{y}, t - \frac{|\mathbf{x} - \mathbf{y}|}{c} \right) d\mathbf{y}, \quad (2-24)$$

then the equation becomes

$$\rho - \rho_0 \sim \frac{\rho_0 A_0 \kappa^2}{2\pi c} \frac{x_i x_j}{x^3} \int \frac{\partial^2}{\partial t^2} \cos[\kappa(y_1 + |\mathbf{x} - \mathbf{y}| - ct)] v'_i \left(\mathbf{y}, t - \frac{|\mathbf{x} - \mathbf{y}|}{c} \right) d\mathbf{y}. \quad (2-25)$$

By multiplying the factor c^3/ρ_0 with the mean square of the Eqn. 2-25, we obtain the intensity of the scattered wave, I_s , as

$$I_s \sim \frac{\rho_0 A_0^2 \kappa^4 c}{4\pi} \frac{x_i x_j x_1^2}{x^6} \int \int \frac{\cos[\kappa(y_1 + |\mathbf{x} - \mathbf{y}| - ct)] \cos[\kappa(z_1 + |\mathbf{x} - \mathbf{z}| - ct)]}{\times v'_i \left(\mathbf{y}, t - \frac{|\mathbf{x} - \mathbf{y}|}{c} \right) v'_j \left(\mathbf{z}, t - \frac{|\mathbf{x} - \mathbf{z}|}{c} \right)} d\mathbf{y} d\mathbf{z}. \quad (2-26)$$

When \mathbf{x} is large compared to $|\mathbf{y} - \mathbf{z}|$, the product of the cosines in Eqn. 2-26 is $\frac{1}{2} \cos(\mathbf{k} \cdot (\mathbf{y} - \mathbf{z}))$, where $k_i = \kappa \left(\frac{x_i}{x} - \delta_{i1} \right)$. So the intensity of the scattered wave becomes

$$I_s \sim \frac{\rho_0 A_0^2 \kappa^4 c}{4\pi} \frac{x_i x_j x_1^2}{x^6} F_{ij}(\mathbf{k}), \quad (2-27)$$

where $F_{ij}(\mathbf{k})$ can be considered as the spectrum respected to the wave vector as

$$F_{ij}(\mathbf{k}) = \frac{1}{8\pi^3} \int \int \overline{v'_i(\mathbf{y})v'_j(\mathbf{y})} d\mathbf{y}. \quad (2-28)$$

By integrating over a sphere in \mathbf{k} space with the center at $(\kappa, 0, 0)$ and the radius of κ , along with multiplying a factor x^2/κ^2 , the scattered energy P_s is obtained from Eqn. 2-27 and Eqn. 2-26 as

$$P_s \sim \frac{2\pi I \kappa^2}{c^2} \int \left(\delta_{i1} + \frac{k_i}{\kappa} \right) \left(\delta_{j1} + \frac{k_j}{\kappa} \right) \left(1 + \frac{k_1}{\kappa} \right)^2 F_{ij}(\mathbf{k}) dS, \quad (2-29)$$

over the \mathbf{k} space sphere, where I is the intensity of the incident wave.

Because $F_{ij}(\mathbf{k})$ is only significant when the k/κ is small, which makes the integrating sphere as small as well. This near-center-point condition leads to simplification that makes the scattered energy as

$$\begin{aligned} P_s &\sim \frac{2\pi I \kappa^2}{c^2} \int_{-\infty}^{\infty} \int_{-\infty}^{\infty} F_{11}(0, k_2, k_3) dk_2 dk_3 \\ &= \frac{I \kappa^2}{c^2} \int d\mathbf{y} \int_{-\infty}^{\infty} \overline{v'_1(y_1, y_2, y_3) v'_1(y_1 + w, y_2, y_3)} dw. \end{aligned} \quad (2-30)$$

For a unit volume of turbulence, the integral resulting from Eqn. 2-30 gives the scattered energy per unit volume, p_s , as

$$p_s \sim 2I \kappa^2 L_1 \frac{\overline{v_1'^2}}{c^2}, \quad (2-31)$$

where L_1 is the macro-scale of turbulence.

Finally, the scattered energy can be calculated by integrating the p_s over the volume of the turbulent structure, the turbulent scattering attenuation coefficient α_t is extracted as

$$\alpha_t = \frac{8\pi^2 L_1}{\Lambda^2} I \frac{\overline{v_1'^2}}{c^2}, \quad (2-32)$$

where Λ is the wave length of the incident wave.

Lighthill's scattering model is well developed and fits the infrasound propagation properly, however, the scattering wave's propagating direction is not considered when we calculate the scattered intensity in Eqn. 2-25. The scattered wave can be in the same direction with the incident wave, which means a portion of the scattered energy can be recycled back into the incident wave.

Therefore, the Lighthill's scattering model may over-predict the attenuation caused by the turbulent scattering.

2.4 Tartaski's Scattering Model

To solve the overestimated attenuation of Lighthill's [50] model, we employ a directional scattering model to modify α_i by recycling part of the scattered energy back into the incident wave. The Tartarski's model [88] is a well-developed theory to account for the directionality of the scattering effect. The model uses the wave equation in moving media

$$\Delta P - \frac{1}{c^2} \left(\frac{\partial}{\partial t} + u_i \frac{\partial}{\partial x_i} \right)^2 P = 0, \quad (2-33)$$

where P is the potential of sound wave and u_i is the velocity of the motion of moving media. We assume that the mean velocity is zero, therefore $u_i = u'_i$. By expanding the square of the operator $\frac{\partial}{\partial t} + u_i \frac{\partial}{\partial x_i}$, we obtain

$$\Delta P - \frac{1}{c^2} \frac{\partial^2 P}{\partial t^2} = \frac{1}{c^2} \frac{\partial u'_i}{\partial t} \cdot \nabla P + \frac{2}{c^2} u'_i \cdot \nabla \frac{\partial P}{\partial t}, \quad (2-34)$$

We only take the accuracy to the order of u'/c , so the first term on the righthand side is neglected. Then Eqn. 2-34 becomes

$$\Delta P - \frac{1}{c^2} \frac{\partial^2 P}{\partial t^2} = \frac{2}{c^2} u'_i \cdot \nabla \frac{\partial P}{\partial t}, \quad (2-35)$$

By applying the ideal gas assumption, we obtain the relation

$$c(T) = c(\bar{T}) \left(1 + \frac{T'}{2\bar{T}} \right). \quad (2-36)$$

In the atmosphere, the quantity T'/\bar{T} is of the same order of u'/c . Then Eqn. 2-36 becomes

$$\Delta P - \frac{1}{c^2} \frac{\partial^2 P}{\partial t^2} = \frac{2}{c^2} u'_i \cdot \nabla \frac{\partial P}{\partial t} + \frac{1}{c^2} \frac{T'}{\bar{T}} \frac{\partial^2 P}{\partial t^2}. \quad (2-37)$$

For a harmonic incident sound wave, we assume the solution takes the form $P = \Pi e^{-i\omega t}$, then

Eqn. 2-37 becomes

$$\Delta \Pi - k^2 \Pi = -2ik \frac{u}{c} \cdot \nabla \Pi + k^2 \frac{T'}{T} \Pi. \quad (2-38)$$

We write the solution of Eqn. 2-38 as a series solution, $\Pi = \Pi_0 + \Pi_1 + \Pi_2 \dots$, which results in

$$\Delta \Pi_0 + k^2 \Pi_0 = 0 \quad (2-39)$$

and

$$\Delta \Pi_1 + k^2 \Pi_1 = -2ik \frac{u'}{c} \cdot \nabla \Pi_0 + k^2 \frac{T'}{T} \Pi_0, \quad (2-40)$$

which is based on an asymptotic expansion. Π_0 represents the amplitude of acoustic wave potential, and we set it as $\Pi_0 = A_0 e^{-ikr}$ for spherical wave. Then we have

$$\Delta \Pi_1 + k^2 \Pi_1 = -2k^2 \left(\frac{u_i \cdot n_i}{c} + \frac{T'}{2T} \right) A_0 e^{-ikr}. \quad (2-41)$$

For a large distance from the scattering volume V_s , ($\lambda r \gg L^2$ and $V_s = L^3$)

$$\Pi_1(\vec{r}) = -\frac{1}{4k} \frac{e^{ikr}}{r} \int 2k^2 \left(\frac{\vec{u}'(\vec{r}') \cdot \mathbf{n}}{c} + \frac{T'(\vec{r}')}{2T} \right) A_0 e^{-ik\vec{r}' \cdot \vec{m}} dV'_s, \quad (2-42)$$

where \vec{m} is the unit vector directed from the center of the scattering turbulent volume to the observer. Thus, $\Pi_1(\vec{r})$ represents a spherical wave with random complex amplitude Q as

$$Q = -\frac{k^2 A_0}{2\pi} \int \left(\frac{\vec{u}'(\vec{r}') \cdot \vec{n}}{c} + \frac{T'(\vec{r}')}{2T} \right) e^{-ik\vec{r}' \cdot (\vec{n} - \vec{m})} dV'_s. \quad (2-43)$$

The average value of the flux density vector of scattering energy is equal to

$$\vec{S} = \frac{\omega \rho}{2} \text{Im}(\Pi_1^* \nabla \Pi_1). \quad (2-44)$$

By calculating the gradient of Π_1 , we obtain

$$\nabla \Pi_1 = \nabla Q \frac{e^{-ikr}}{r} = Q \left(ik \frac{e^{ikr}}{r} - \frac{e^{ikr}}{r^2} \right) \vec{m} - ikQ \frac{e^{ikr}}{r} \vec{m}. \quad (2-45)$$

Therefore we have

$$\vec{S} = \frac{\omega \rho}{2} \text{Im} \left(Q^* \frac{e^{-ikr}}{r} - ikQ \frac{e^{ikr}}{r} \vec{m} \right) = \frac{\omega \rho k}{2r^2} Q Q^* \vec{m}. \quad (2-46)$$

The mean value of the scattering energy in Eqn. 2-46 is

$$\vec{S} = \frac{\omega \rho k}{2r^2} \overline{QQ^*} \vec{m} = \vec{m} \frac{\rho c k^6 A_0^2}{8\pi^2 r^2} \times \iint \left[\frac{\vec{u}'(\vec{r}'_1) \cdot \vec{n}}{c} + \frac{T'(\vec{r}'_1)}{2T} \right] \left[\frac{\vec{u}'(\vec{r}'_2) \cdot \vec{n}}{c} + \frac{T'(\vec{r}'_2)}{2T} \right] e^{-ik(\vec{r}_1 - \vec{r}_2) \cdot (\vec{n} - \vec{m})} dV_1 dV_2. \quad (2-47)$$

Based on incompressibility, we have no correlation of \vec{u}' and \vec{T}' . The correlation tensors of velocity and temperature are

$$B_{ik}(r_1 - r_2) = \overline{u'_i(r_1) u'_k(r_2)} \quad (2-48)$$

and

$$B_T(r_1 - r_2) = \overline{T'(r_1) T'(r_2)}. \quad (2-49)$$

By evaluating the double integrals over the volume using Eqn. 2-47, we obtain

$$\vec{S} = \vec{m} \frac{\rho c k^6 A_0^2}{8\pi^2 r^2} \left[\frac{1}{c^2} n_i n_k \int B_{ik}(\vec{r}') e^{ik(\vec{n} - \vec{m})\vec{r}'} dV' + \frac{1}{4T^2} \int B_T(\vec{r}') e^{ik(\vec{n} - \vec{m})\vec{r}'} dV'_s \right]. \quad (2-50)$$

Similar to the spectrum of velocity field in the turbulent flow, we can obtain the correlation tensor by using spectrum of energy, $E(\vec{k})$, and temperature spectrum, $\Phi_T(\vec{k})$. Now, Eqn. 2-48 and Eqn. 2-49 become

$$B_{ik}(\vec{r}) = \iiint_{-\infty}^{+\infty} e^{i\vec{k}\vec{r}} \left(\delta_{ik} - \frac{k_i k_k}{k^2} \right) E(\vec{k}) d\vec{k} \quad (2-51)$$

and

$$B_T(\vec{r}) = \iiint_{-\infty}^{+\infty} e^{i\vec{k}\vec{r}} \Phi_T(\vec{k}) d\vec{k}. \quad (2-52)$$

Then we integrate terms $B_{ik}(\vec{r}) e^{-i\vec{k}\vec{r}}$ and $B_T(\vec{r}) e^{i\vec{k}\vec{r}}$ in flux density Eqs. 2-50, we obtain

$$\vec{S} = \vec{m} \frac{\rho c k^6 A_0^2}{8\pi^2 r^2} \left[\frac{1}{c^2} n_i n_k \overline{\left(\delta_{ik} - \frac{k^2 (n_i - m_i)(n_k - m_k)}{k^2 (\vec{n} - \vec{m}) \cdot (\vec{n} - \vec{m})} \right) E(k(\vec{n} - \vec{m}))} + \frac{1}{4T^2} \overline{\Phi_T(k(\vec{n} - \vec{m}))} \right]. \quad (2-53)$$

The double bar function $\overline{F(\vec{k})}$ denotes the average of this function over the region in wave number space of volume $8\pi^3/V_s$ surrounding the point \vec{k} . In our case, the volume V_s is so large that averaging the region $8\pi^3/V_s$ of wave number space does not substantially change the

averaged function, so we can simplify the term

$$n_i n_k \left(\delta_{ik} - \frac{k^2 (n_i - m_i)(n_k - m_k)}{k^2 (\vec{n} - \vec{m}) \cdot (\vec{n} - \vec{m})} \right) = \frac{1}{2} (1 + \vec{n} \cdot \vec{m}). \quad (2-54)$$

As $\vec{n} \cdot \vec{m} = \cos \theta$, we have $\frac{1}{2} (1 + \vec{n} \cdot \vec{m}) = \cos^2 \frac{\theta}{2}$. The Eqn. 2-53 becomes

$$\vec{S} = \vec{m} \frac{\pi \rho c k^6 A_0^2 V_s}{r^2} \left[\frac{1}{c^2} E(k(\vec{n} - \vec{m})) \cos^2 \frac{\theta}{2} + \frac{1}{4T^2} \Phi_T(k(\vec{n} - \vec{m})) \right]. \quad (2-55)$$

By assuming the isotropic turbulence, $E(\vec{k}) = E(k)$, $\Phi(\vec{k}) = \Phi(k)$, we obtain

$$\vec{S} = \vec{m} \frac{\pi \rho c k^6 A_0^2 V_s}{r^2} \left[\frac{1}{c^2} E\left(2k \sin \frac{\theta}{2}\right) \cos^2 \frac{\theta}{2} + \frac{1}{4T^2} \Phi_T\left(2k \sin \frac{\theta}{2}\right) \right]. \quad (2-56)$$

By normalizing with the incident wave's energy flux density, we obtain

$$d\sigma(\theta) = 2\pi k^4 V_s \left[\frac{1}{c^2} E\left(2k \sin \frac{\theta}{2}\right) \cos^2 \frac{\theta}{2} + \frac{1}{4T^2} \Phi_T\left(2k \sin \frac{\theta}{2}\right) \right] d\Omega. \quad (2-57)$$

Then we employ the spectra from Tatarski [88]

$$E(k) = 0.061 C_v^2 k^{-\frac{11}{3}}, \quad (2-58)$$

and

$$\Phi(k) = 0.033 C_T^2 k^{-\frac{11}{3}}, \quad (2-59)$$

into Eqn. 2-57, where $C_v^2 = \varepsilon^{2/3}$, and $C_T = a^2 \bar{N} \varepsilon^{-1/3}$ [124], ε is the turbulence dissipation rate,

C and a are constant, and \bar{N} is the temperature dissipation rate (see details in Oboukhov [124]).

Then we obtain

$$d\sigma(\theta) = 0.030 k^{\frac{1}{3}} V \left[\frac{C_v^2}{c^2} \cos^2 \frac{\theta}{2} + 0.13 \frac{C_T^2}{T^2} \right] \left(\sin \frac{\theta}{2} \right)^{-\frac{11}{3}} d\Omega. \quad (2-60)$$

We introduce $l(\theta) = \frac{2\pi}{2k \sin \frac{\theta}{2}}$ here, and the final equation is

$$d\sigma(\theta) = \frac{V}{2\pi l} \left[\frac{v_0^2}{3c_0^2} \sin^2 \theta \left(\frac{k^2 l^2}{1 + k^2 l^2 \sin^2 \frac{\theta}{2}} \right)^3 + \frac{T_0^2}{T^2} \left(\frac{k^2 l^2}{1 + k^2 l^2 \sin^2 \frac{\theta}{2}} \right)^2 \right] d\Omega. \quad (2-61)$$

Equation 2-61, is a direction-dependent equation. The first term on the right hand side is the scattering caused by the velocity fluctuation, and the second term is the scattering caused by the temperature fluctuation.

2.5 Ostashev and Wilson's Model

Since Tartarski developed his scattering model[88], further improvements have been applied by Ostashev and Wilson [11]. Ostashev improved Tartarski's model by using a Helmholtz-type equation (Eqn. 6.91 in [11]) as

$$\left[\nabla^2 + k^2(1 + \varepsilon_a) - (\nabla \ln(\rho/\bar{\rho})) \cdot \nabla - \frac{2i}{\omega} \frac{\partial v'_i}{\partial x_j} + \frac{\partial^2}{\partial x_i \partial x_j} + \frac{2ik}{\bar{c}} \mathbf{v}' \cdot \nabla \right] \hat{p} = \rho(i\omega - \mathbf{v}' \cdot \nabla) \hat{Q}, \quad (2-62)$$

where k is the wave number of the acoustic wave, $\varepsilon_a = \bar{c}^2/c^2 - 1$, c is the speed of sound, ρ is the instantaneous density, ω is the frequency, \hat{p} represents the spectrum of the acoustic wave, v' is the velocity fluctuation, and \hat{Q} is the function of the mass source. The overline represents an averaged quantity, and the hat represents a spectrum. The scattering field is presented as (see Eqn. 6.110 of [11]) as

$$\langle I_s \rangle = \frac{2\pi k^4 I_0 \mathbf{n}}{R^2} \left[\frac{\beta^2(\theta) \Phi_T(\mathbf{q})}{4T_0^2} + \frac{\beta(\theta) \eta(\theta) \Phi_{CT}(\mathbf{q})}{2T_0} + \frac{\eta^2(\theta) \Phi_C(\mathbf{q})}{4} + \frac{\cos^2 \theta n_{0,i} n_{0,j} \Phi_{ij}(\mathbf{q})}{\bar{c}^2} \right]. \quad (2-63)$$

where the $\langle I_s \rangle$ is the mean intensity of the scattered field, \mathbf{n} is the direction of the scattered wave, I_0 is the intensity of the incident acoustic wave, R is the distance from the scattering location to the observer, β and η are the construction parameters defined by Eqn. 6.67 of [11], θ is the scattering angle, and Φ_T , Φ_{CT} , Φ_C , and Φ_{ij} are the spectra of temperature, humidity-temperature, humidity, and velocity fluctuations, respectively. Then Eqn. 2-63 can be simplified and represented by the cross-section σ as

[11] as

$$\sigma(\theta) = \sigma(\mathbf{n} - \mathbf{n}_0) = 2\pi k^4 \left[\frac{\beta^2(\theta)\Phi_T(\mathbf{q})}{4T_0^2} + \frac{\beta(\theta)\eta(\theta)\Phi_{CT}(\mathbf{q})}{2T_0} + \frac{\eta^2(\theta)\Phi_C(\mathbf{q})}{4} + \frac{\cos^2 \theta \cot^2(\theta/2)E(\mathbf{q})}{16\pi k^2 \bar{c}^2} \right], \quad (2-64)$$

where $\sigma(\theta)$ is the scattering cross-section and defined as

$$\sigma(\theta) = \frac{I_s(\theta)R^2}{I_0V}. \quad (2-65)$$

The cross-section referenced is on a per unit volume basis. More details about Ostashev's model are available in Ostashev and Wilson [11].

To extend and validate the scattering model, a series of boundary layer wind tunnel tests are conducted. However, in the boundary layer flow in the wind tunnel, the fluctuations of the first three terms in Eqn. 2-64 are negligible. Thus, in the following investigation, only the fourth term on the right hand side is retained to account for the velocity inhomogeneity, and this term is named as the turbulent cross-section σ_E as

$$\sigma_E(\theta) = 2\pi k^4 \left(\frac{\cos^2 \theta \cot^2(\theta) E(2k \sin \frac{\theta}{2})}{16\pi k^2 \bar{c}^2} \right), \quad (2-66)$$

where $E(\kappa)$ is the turbulent velocity spectrum. Here, the von Karman spectrum is used and is

$$E(\kappa) = \frac{55\Gamma(5/6)}{9\pi^{1/2}\Gamma(1/3)} \frac{\sigma_v^2 \kappa^4 L_v^5}{(1 + \kappa^2 L_v^2)^{17/6}}, \quad (2-67)$$

where $\kappa = 2k \sin \frac{\theta}{2}$ is the scattering wave number, Γ is the gamma function, and σ_v is the variance of the fluctuating velocity. Because our goal is to predict the scattered acoustic energy, the total scattering cross-section is

$$\sigma_{E,tot} = \int_0^{2\pi} \int_0^\pi \sigma_E(\theta) \sin(\theta) d\theta d\phi, \quad (2-68)$$

where subscript *tot* denotes total.

2.6 Acoustic-Turbulent Interaction Bridging Model

2.6.1 Turbulent Refraction and Bridging Model

Although Ostashve's [11] model accounts for directional scattering, small refraction angles, θ , can invalidate the resulting cross-section calculation. As θ approaches zero, $\kappa = 2k \sin \frac{\theta}{2}$ also reaches zero, indicating that the scattering near the forward propagation direction is caused by large-scale (or extremely large-scale) turbulence. However, when the turbulent structure is larger than the acoustic wavelength, turbulent refraction is believed to contribute to acoustic-turbulent interaction instead of scattering.

A new model is developed based on the concept shown in Fig. 2-5 to bridge the turbulent scattering and turbulent refraction.

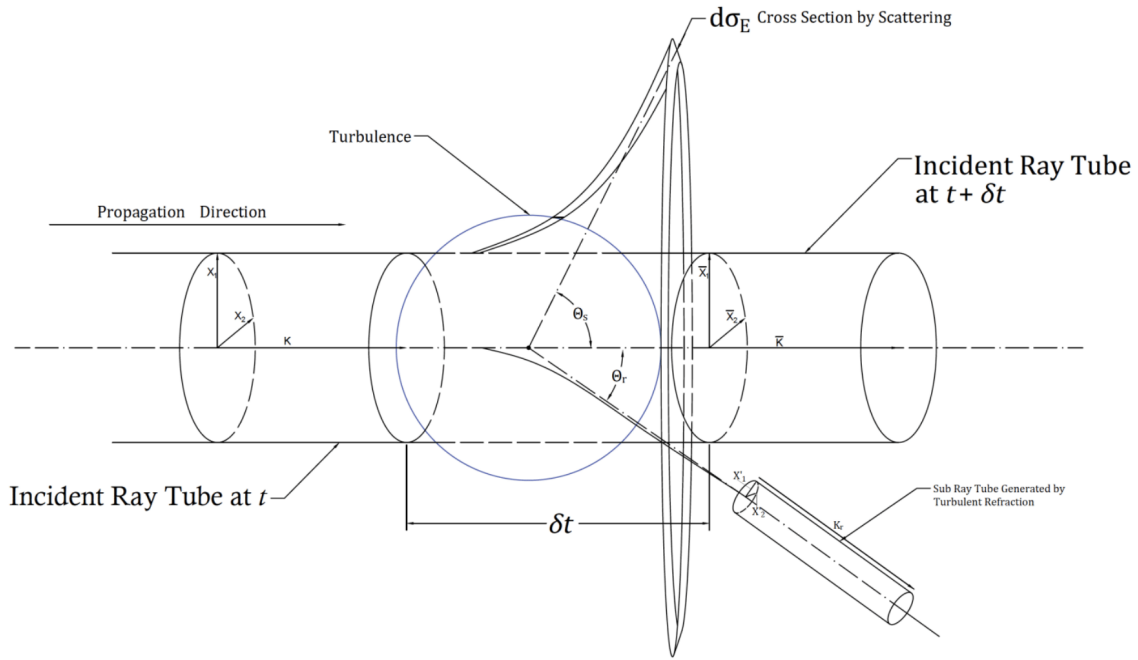


Figure 2-5. Concept of the bridging model.

In this figure, a right-running incident wave is assumed to be a plane wave with the condition $R_0 \gg \lambda$, where R_0 is the propagation distance and λ is the wave length of the incident wave. The incident wave is represented by the incident ray tubes at t and $t + \delta t$. The blue sphere represents a turbulent eddy that the acoustic wave impacts upon. Acoustic-turbulent interaction occurs during

the time span between t and $t + \delta t$. The turbulent scattering angle is represented by two angle, Θ_s and Θ_r . Θ_s is the scattering angle, and Θ_r is the turbulent refraction angle. To the right side of the turbulent structure, a ring represents the Ostashev's scattering-cross section. $d\sigma_E$ is the turbulent scattering cross-section discussed in the previous subsection. The \mathbf{X} s are the geodisc elements. The detailed parameters' introduction and subray tube development will be presented in the following discussion.

To capture the refraction caused by the turbulence, the geodesic elements technique of ray theory [122] is employed to represent the ray tube and to construct the convective volume. The governing equation [10] for the geodesic element is

$$\begin{aligned} \frac{d\mathbf{X}_{\mathbf{p}_i}}{dt} &= \frac{\partial}{\partial p_i} (\bar{c}(\mathbf{X}, t) \mathbf{N} + v_0(\mathbf{X}, t)) \\ &= \bar{c} \frac{\partial \mathbf{N}}{\partial p_i} + (\mathbf{X}_{\mathbf{p}_i} \cdot \nabla \bar{c}) \mathbf{N} + (\mathbf{X}_{\mathbf{p}_i} \cdot \nabla) \mathbf{v}_0, \end{aligned} \quad (2-69)$$

where the subscript \mathbf{p}_i represents the local coordinate system at the wave front and the X is the geodisc element as discussed in previous subsection.

The first step is the decomposition of the velocity field as $\mathbf{v}_0 = \bar{\mathbf{v}}_0 + \mathbf{v}_0'$. Then the geodisc elements are expressed as

$$\begin{aligned} \frac{d\mathbf{X}_{\mathbf{p}_i}}{dt} &= \frac{d\bar{\mathbf{X}}_{\mathbf{p}_i}}{dt} + \frac{d\mathbf{X}_{\mathbf{p}_i}'}{dt} \\ &= \bar{c} \frac{\partial \mathbf{N}}{\partial p_i} + (\mathbf{X}_{\mathbf{p}_i} \cdot \nabla \bar{c}) \mathbf{N} + (\mathbf{X}_{\mathbf{p}_i} \cdot \nabla) (\bar{\mathbf{v}}_0 + \mathbf{v}_0'). \end{aligned} \quad (2-70)$$

The additional term $(\mathbf{X}_{\mathbf{p}_i} \cdot \nabla) \mathbf{v}_0'$ is the fluctuating geodisc element generated by the turbulent refraction. Unlike the governing equation of the geodesic element $\mathbf{X}_{\mathbf{p}_i}$ in Eqn. 2-69, the $\mathbf{X}_{\mathbf{p}_i}'$ is generated along the ray path and independent relative to its values at previous times. Thus, the term $\frac{d\mathbf{X}_{\mathbf{p}_i}}{dt}$ can be interpreted as the generation rate of a turbulent refraction element. In Gainville [10]'s paper, the convection volume is defined as

$$v = \frac{|\mathbf{X}_1 \wedge \mathbf{X}_2|}{|\mathbf{K}|} = \frac{|\mathbf{X}_1 \wedge \mathbf{X}_2| \cdot \lambda}{2\pi}, \quad (2-71)$$

where \mathbf{X}_1 and \mathbf{X}_2 are corresponding geodisc elements, which are perpendicular to the wave vector. The geodisc elements \mathbf{X}_1 and \mathbf{X}_2 are presented in Fig. 2-5 in the incident ray tube at t . Since the magnitude of the wave vector \mathbf{K}_r is same as the incident wave's wave vector \mathbf{K} , the turbulent refracted convective volume is

$$v' = \frac{|\mathbf{X}'_1 \wedge \mathbf{X}'_2|}{|\mathbf{K}_r|} = \frac{|\mathbf{X}'_1 \wedge \mathbf{X}'_2|}{|\mathbf{K}|} = \frac{|\mathbf{X}'_1 \wedge \mathbf{X}'_2| \cdot \lambda}{2\pi}. \quad (2-72)$$

This equation is also represented in Fig. 2-5 by the sub ray tube in the right lower corner. The sub ray tube is produced by the generation of \mathbf{X}'_1 and \mathbf{X}'_2 . If the field is represented by locally isotropic turbulence, the direction of the refracted wave vector \mathbf{K}_r deviates from the mean incident wave vector $\bar{\mathbf{K}}$. Multiple refractions can cause the refracted wave to return to the incident wave, however, the energy contained within multiple refracted waves is negligible compared to the initial refracted wave as the all the scattered waves are considered as spherical waves [11].

The turbulent refracted convective volume v' is required to ascertain the intensity of refracted waves. In Eqn. 2-72, \mathbf{X}'_1 and \mathbf{X}'_2 represent the value of $\frac{d\mathbf{X}_1}{dt}$ and $\frac{d\mathbf{X}_2}{dt}$, respectively, which are the generation rate of the geodesic elements for the subray tube. The governing equation of \mathbf{X}'_i is obtained from Eqn. 2-70 as

$$\mathbf{X}'_i = \frac{d\mathbf{X}_{p_i}}{dt} = (\mathbf{X}_{p_i} \cdot \nabla) \mathbf{v}'_0. \quad (2-73)$$

Because the value of the incident wave vector is identical to the refracted wave vector, its influence on the value of the convective volume can be ignored. Thus Eqn. 2-73 can be expanded as

$$\begin{aligned}
X'_{1,j} &= \frac{1}{2} X_{1,i} \left(\frac{\partial v'_{0,i}}{\partial p_j} + \frac{\partial v'_{0,j}}{\partial p_i} \right); \\
X'_{2,j} &= \frac{1}{2} X_{2,i} \left(\frac{\partial v'_{0,i}}{\partial p_j} + \frac{\partial v'_{0,j}}{\partial p_i} \right).
\end{aligned} \tag{2-74}$$

Then the mean convective volume is obtained by inserting Eqn. 2-74 into Eqn. 2-72 as

$$\begin{aligned}
v' &= \frac{\lambda}{8\pi} X_{1,i} X_{2,i} \overline{\left(\frac{\partial v'_{0,i}}{\partial p_j} + \frac{\partial v'_{0,j}}{\partial p_i} \right)^2} \cos(\mathbf{X}_1, \mathbf{X}_2) \\
&= \frac{\lambda}{8\pi} X_{1,i} X_{2,i} \overline{s_{ij}s_{ij}} \cos(\mathbf{X}_1, \mathbf{X}_2).
\end{aligned} \tag{2-75}$$

The turbulent refraction cross-section σ_r is defined as

$$\sigma_r = \frac{v'}{v} = \frac{\overline{s_{ij}s_{ij}}}{4} \sim \frac{\sigma_v^2}{\lambda_T^2}, \tag{2-76}$$

where the term $\overline{s_{ij}s_{ij}}$ represents the turbulent velocity variance σ_v and the Taylor microscale λ_T [125].

For infrasound waves, the large-scale turbulence has the greatest effect on turbulent refraction. Therefore, the relation between the turbulent wave number and the fluctuating strain rate is employed as [126]

$$\overline{s_{ij}s_{ij}} = \frac{\varepsilon}{2\nu} = \int_0^\infty k^2 E(k) dk. \tag{2-77}$$

Then only the turbulence with length scale larger than L_v is used within $\overline{s_{ij}s_{ij}}$, then σ_r is

$$\sigma_r = \frac{v'}{v} \sim \frac{\sigma_v^2}{\lambda_T^2} \frac{\int_0^{2\pi/L_v} k^2 E(k) dk}{\int_0^\infty k^2 E(k) dk}. \tag{2-78}$$

Here, we define the variable C_E as $(\int_0^{2\pi/L_v} k^2 E(k) dk) / (\int_0^\infty k^2 E(k) dk)$, which ranges approximately from 10^{-6} to 10^{-4} within the von Kármán spectrum. Thus, σ_r can also be represent as $\sigma_r = C_F \sigma_v^2 / L_v^2$, where $C_F = L_v^2 C_E / \lambda_T^2$.

Unlike scattering described by Eqn. 2-65, σ_r is no longer a function involving the scattering angle because of the integration of the $k^2 E(k)$ over the scattering angle from 0 to $2\pi/L_v$ in Eqn. 2-78. Thus, we require a model function to bridge the refraction cross-section σ_r with the directional scattering cross-section σ_E . Since we only use a refraction model at the low scattering angles (where $k \sin(\theta/2) < 2\pi/L_v$), a sine function is selected with σ_r as

$$\sigma_{eff}(\theta) = \max(\sigma_E(\theta)) - \frac{A}{\sigma_r} \left[\sin \left(\frac{\pi k_r L_v}{2} - \pi/2 \right) - 1 \right], \quad (2-79)$$

where A is the constant coefficient to be determined. Here, $k_r = 2k \sin \frac{\theta}{2}$ and $k_r \in (0, \frac{2\pi}{L_v})$. By applying this bridging function, the turbulent refraction is represented by the area below the sine curve and can be adjusted the parameters in Eqn. 2-79. Finally, we obtain the expression for the effective total cross-section as

$$\sigma_{tot} = \sigma_{eff} + \int_0^{2\pi} \int_{2\arcsin(\frac{\pi}{kL_v})}^{\pi} \sigma_E(\theta) \sin(\theta) d\theta d\phi, \quad (2-80)$$

and an example plot of the bridging model is shown in Fig. 2-6.

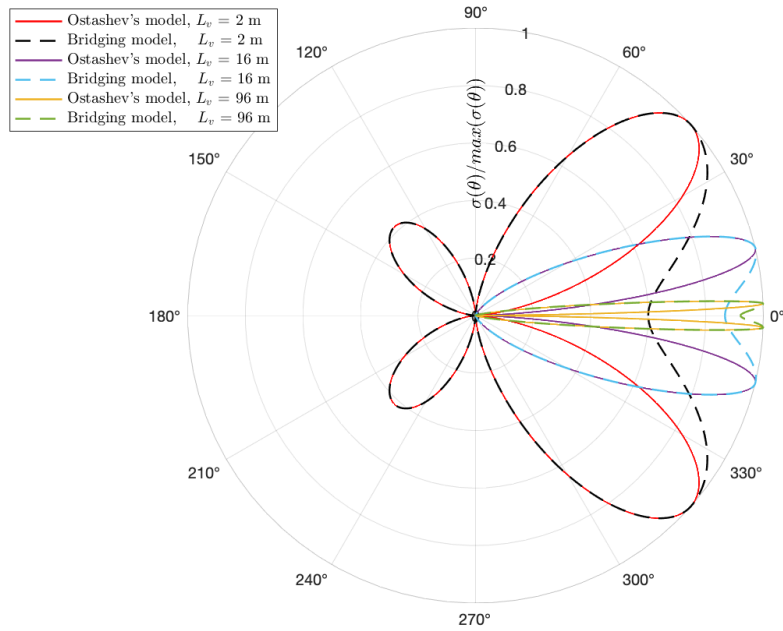


Figure 2-6. An example of the bridging cross-section model compared with Ostashev's model.

Figure 2-6 shows the difference between the proposed bridging model and Ostashev's model [11]. Turbulent refraction is the primary effect within the new model near scattering angles that are small.

2.6.2 Log Amplitude and Phase Fluctuation

As the mean absorption and dispersion coefficients are obtained from the above discussion, the fluctuation range can be also calculated by implementing the line-in-sight theory to the Burgers' propagation solver. The variances of amplitude and phase fluctuations [127] are

$$\sigma_{\chi, \phi} = \frac{\pi^2 k^2}{2 \cos(\theta)} \int_0^h dz \int_0^\infty \Phi(z, k) \left[1 \mp \cos \left(\frac{z(h-z)k^2}{kh \cos \theta} \right) \right] dk, \quad (2-81)$$

where χ and ϕ represent absorption and dispersion, θ is the angle between path and vertical direction, h is the height along the path, and Φ is the turbulent spectrum.

2.7 Summary

In this section, the techniques used in the propagation solver development are introduced and discussed. The entire methodology consists of three major parts: the generalized Burgers' equation solver with acoustic ray tracing, and the turbulent scattering attenuation models. Introducing the turbulent effect into the generalized Burgers' equation is the major innovation of the solver. With both numerical models and experimental results, the model implemented into the propagation solver is able to capture the turbulent effect on the infrasound propagation in the turbulent atmospheric boundary layer.

CHAPTER 3

RESULTS OF NUMERICAL SOLVER

In this chapter, the preliminary results of the numerical solver are demonstrated. The numerical solver consists of two parts, the acoustic ray tracing solver and the generalized Burgers' equation propagation solver. In Section 3.1, the validations of the acoustic ray tracing solver and the validations of the generalized Burgers' equation solver are presented. The results of the acoustic ray tracing solver are compared with a numerical acoustic ray tracing solver developed by Hallberg et al. [82]. The effects of the nonlinearity and attenuation are validated by comparing with the Blackstock Bridging Function (BBF) and Sutherland and Bass's model [68], respectively. As the satisfactory validation results are obtained for both the acoustic ray tracing solver and propagation solver, a case study in four different regions is performed. The ray tracing results in these regions are obtained with realistic atmospheric models (HWM93 [120] and NRLMSISE-00 [121]). Both sinuous infrasound and broadband tornadic infrasound sources are employed to demonstrate the propagation along the calculated ray paths. The results of the propagation solver are demonstrated and discussed in Section 3.2.

3.1 Validation of the Numerical Solver

3.1.1 Ray Tracing Validation

The first step in the prediction process involves finding the propagation paths of the acoustic waves. This is performed with the propagation solver. As shown in Fig. 2-1, the results of the ray tracing solver are: the ray path data and the wind and temperature data along the rays. The ray paths and atmospheric data are then used by the propagation solver, which marches along each ray cast from source to observer. Therefore, an accurate acoustic ray tracing solver is the foundation of the entire numerical solver, and the validation of the ray tracing solver is important and necessary.

The governing equations for ray acoustics can be solved analytically with linear speed of sound and temperature profiles (see details in Thompson [8]). As a validated ray tracing solver with corresponding analytical solution, the solver of Hallberg et al. [82] is used to validate the new ray tracing solver. Figure 3-1 shows a comparison of the ray tracing solver prediction and the

two-dimensional result of Hallberg et al. [82] with identical linear wind and temperature profiles. The sound source is located at zero altitude with $X = 0$ km, and the launching angle is 45°

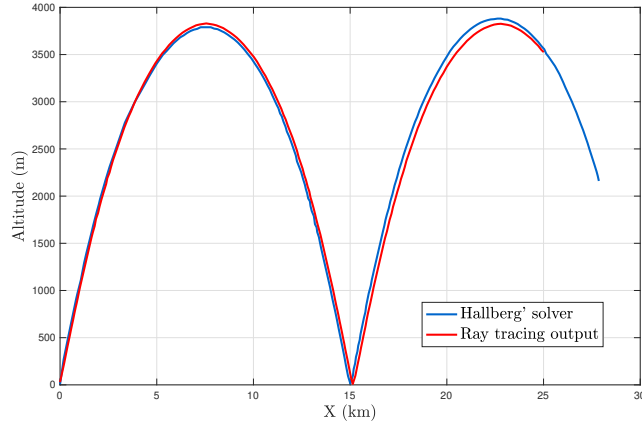


Figure 3-1. Validation with previous two-dimensional solver of Hallberg.

relative to the X direction. The parabolic wind and temperature profiles amplify the refraction effect. The two touch-down locations from the acoustic ray tracing solver and Hallberg's solver are at $X = 15003.34$ m and $X = 15130.86$ m, respectively, where the difference is 0.85%.

Because a b-spline interpolation method is employed in our ray tracing solver, the precision of the ray tracing solver is dependent on the grid point spacing (discussed in Subsection 2.2.2), which causes differences relative to the solver of Hallberg et al. [82]. Besides the comparison with the previous solver, the test case of the ray tracing solver with atmospheric models is shown in Fig 3-2. This is a east propagating test at Gainesville. Three rays are launched with angles of 0° , 15° ,

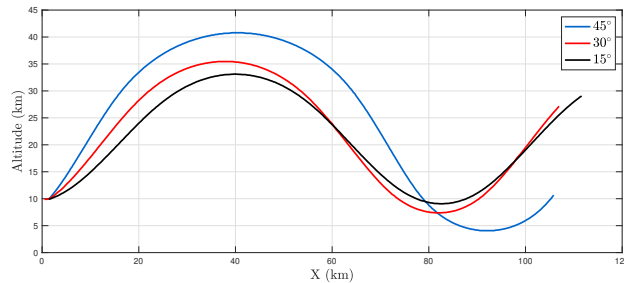


Figure 3-2. Test cases with different vertical launching angles from -82.3248262° W, 29.6516344° N, along latitude 29.6516344° N.

and 30° along latitude 29.6516344° towards the east in this figure. With westward winds, a

shadow zone appears at approximately 100 km from the source location.

The ray tracing solver's ability to capture the refraction effect provides the generalized Burgers' equation solver with the capability of predicting propagation in a three-dimensional domain. Presently, only limited validation cases are conducted for ray tracing and attenuation predictions. Therefore, a well-designed validation procedure is necessary to guarantee the solver's accuracy. As a benchmark ray tracing solver, the solver of Hallberg et al. [82] will be employed to further validate our ray tracing solver. The governing equations of the rays in the solver of Hallberg et al. [82] are shown as following

$$\frac{dx}{dz} = \pm \frac{v(1 - vk_1) + c^2 k_1}{c\Omega_r^{\frac{1}{2}}}, \quad (3-1)$$

$$\frac{dy}{dz} = \pm \frac{ck_2}{\Omega_r^{\frac{1}{2}}}, \quad (3-2)$$

$$\frac{dt}{dz} = \pm \frac{(1 - vk_1)}{c\Omega_r^{\frac{1}{2}}}, \quad (3-3)$$

$$\Omega = (1 - vk_1)^2 - c^2(k_1 + k_2)^2, \quad (3-4)$$

where x , y , and z are the coordinates of the wave front. k_1 and k_2 are ray parameters, which are constant for each ray as

$$k_1 = \frac{\sin \mu \cos \theta}{d} - \frac{v_0}{d^2 + v_0 d \sin \mu \cos \theta}, \quad (3-5)$$

and

$$k_2 = \frac{\sin \mu \cos \theta}{d}, \quad (3-6)$$

where $d = [v_0^2(\sin^2 \mu \cos^2 \theta - 1) + c_0^2]^{\frac{1}{2}}$, $v_0 = v(z_s)$, $c_0 = c(z_s)$, μ and θ are the altitude and azimuth angles, and z_s is the altitude of the sound source.

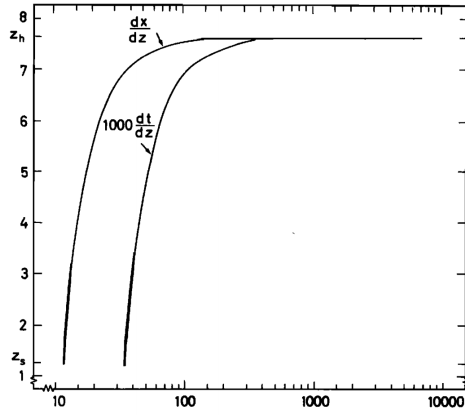
To validate our ray tracing solver, a test matrix is conducted by both the ray tracing solver and the Hallberg's solver as shown as Table 3-1. In this test matrix, the wind profile and the speed of sound profile are set as three types: the linear profile, the parabolic profile, and the cubic

Table 3-1. Ray tracing solver validation matrix and comparison with Hallbergs' solver.

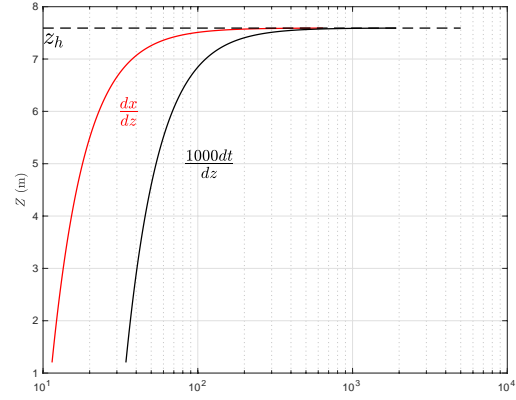
Setpoint	Launching Angle (degree)	Wind Profile	Speed of Sound Profile	Turning Point of RTS (m)	Turning Point of Hallberg (m)
1	15	linear	linear	245	250
2	30	linear	linear	403	415
3	45	linear	linear	821	858
4	15	N/A	linear	325	328
5	30	N/A	linear	756	761
6	45	N/A	linear	1694	1702
7	20	parabolic	parabolic	236	236
8	30	parabolic	parabolic	280	280
9	40	parabolic	parabolic	342	344
10	50	parabolic	parabolic	425	434
11	60	parabolic	parabolic	543	573
12	70	parabolic	parabolic	806	838
10	30	N/A	parabolic	314	315
11	45	N/A	parabolic	444	445
12	60	N/A	parabolic	648	650
13	30	cubic	cubic	235	235
14	45	cubic	cubic	279	282
15	60	cubic	cubic	353	370
16	30	N/A	cubic	243	244
17	45	N/A	cubic	293	294
18	60	N/A	cubic	368	369

profiles. The linear profile of the wind can be expressed as a function of the altitude z as $v_{wind} = 0.2z + 10$; the parabolic profile of the wind is $v_{wind} = 10 + 0.001z^2$; and the cubic profile of the wind is $10 + 0.00001z^3$. The linear profile of the speed of sound can also be expressed as a function of the altitude as $343 + 0.2z$; the parabolic profile of the speed of sound is $343 + 0.001z^2$; and the cubic profile of the speed of sound is $343 + 0.00001z^3$. Different ray radiation angles are also included in the test matrix as shown as the first column in Table 3-1. To compare the ray tracing solver and Hallberg's solver, we use the turning point altitude Z_h as the validation parameter. The average difference between current ray tracing solver and Hallberg's solver is 1.693%, while the case by case difference varies between 0 to 5.23%. Because the ray tracing solver uses the wave front tracking method, a slight difference from the Snell-law-based Hallberg's solver is expected. Based on the results from the test matrix, the ray tracing solver agrees well with Hallberg's solver on the turning point.

In Hallberg's paper [82], a case study is conducted to investigate the effect of the order of magnitude of the governing equations. This case is repeated by our ray tracing solver, and the results are shown in 3-3a and 3-3b. The launching angle of this case is set to 85 degree. The



(a) Results from Hallberg's paper (Fig. 2 in the original paper).



(b) Results from the ray tracing solver with the same conditions

Figure 3-3. Comparison between the ray tracing solver and Hallberg's solver

horizontal wind profile is linear as the wind velocity $v_{wind} = 0.2z$, and constant speed of sound profile is obtained in this case. In the Fig. 3-3, the overall behavior of the ray are same in both solvers when the value of dt/dz is amplified 1000 times. The turning point in both solvers converges to approximately $Z_h = 7.6$ m, where Z_h represents the height where the ray begin propagates downwards.

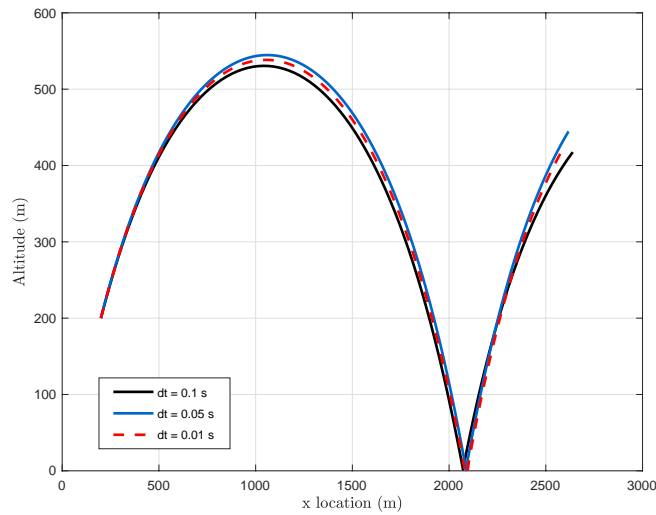


Figure 3-4. Ray tracing solver validation with linear temperature and wind profiles, time step sizes are 0.1 s, 0.05 s, and 0.01 s

Besides the solver validation, a grid independence study is also conducted. We conducted

both time-step-size dependency and spatial mesh dependency studies for the ray tracing solver.

Fig. 3-4 shows the influence of the time step size on the ray propagation. In this figure, the linear temperature and speed of sound profiles are implemented while the ray is launched at 45 degree relative to the horizon. The three time step sizes are 0.1 s, 0.05 s, and 0.01 s. The 0.01 s case is set as the benchmark case for the other two to compare with. Both x -direction and z -direction difference of the turning point is recorded in Table 3-2. The difference in this case converges to zero with increasing Δt .

Table 3-2. Turning-point location difference between time step size = 0.1 s, 0.05 s, 0.01 s

	dt = 0.1s	dt = 0.05s	dt = 0.01s
Z-error (m)	12.619	5.642	0
X-error (m)	4.897	2.201	0

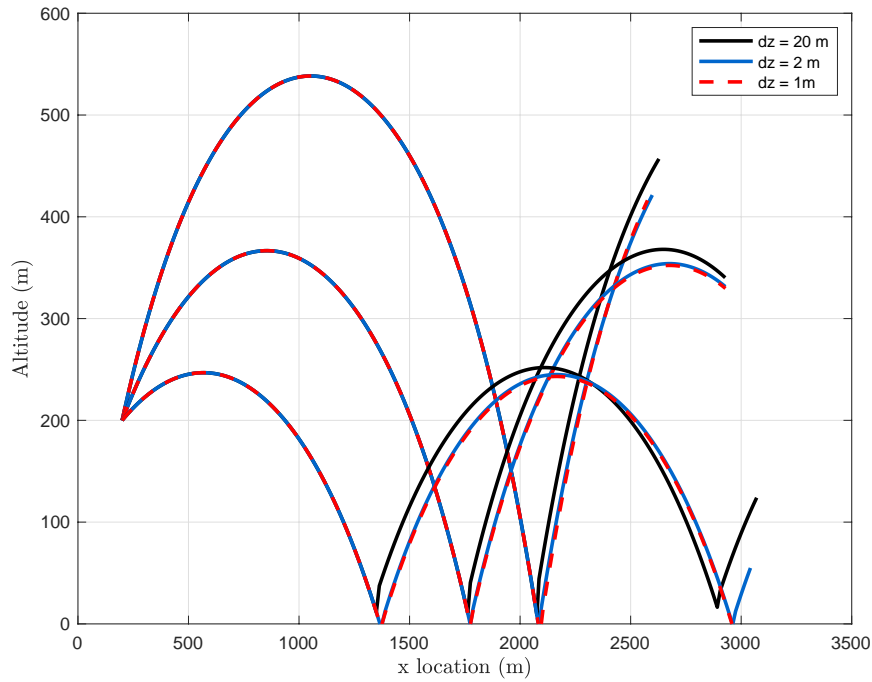


Figure 3-5. Ray tracing solver validation with linear temperature and wind profiles, three launching angles are 15° , 30° , and 45° .

A spatial step size dependency study is also conducted with three grid step sizes in the z -direction, and the results are shown in Fig. 3-5. The grid step sizes are set as $dz = 20$ m, $dz = 2$

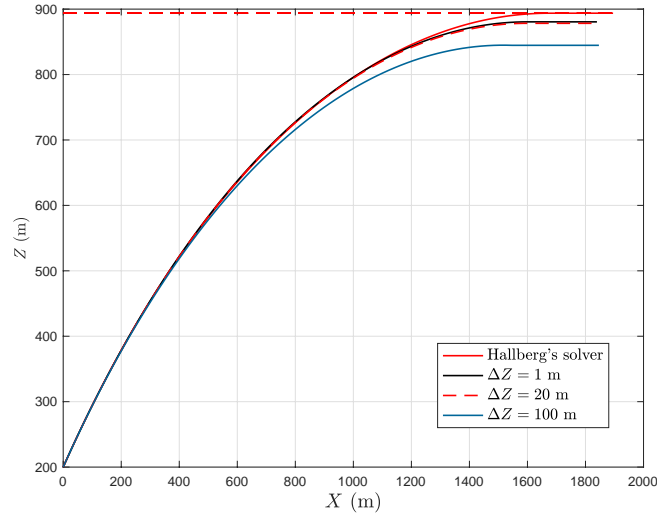


Figure 3-6. Comparison between my RTS and Hallberg's solver

m, and $dz = 1$ m. As shown in Fig. 3-5, all three rays almost overlap with each other before the first ground reflection. The grid step size cases are also compared with Hallberg's solver as shown in Fig. 3-6. The difference between the rays of our predictions solver and Hallberg's ray are 13.244 m, 15.98 m, and 49.11 m for $\Delta Z = 1$ m, $\Delta Z = 20$ m, and $\Delta Z = 100$ m, respectively. The difference is also expected since the two approaches, which are the wavefront movement method and Snell's law.

3.1.2 Propagation Solver Validation

As discussed in Chapter 2, the generalized Burgers' equation is capable of capturing the nonlinearity, attenuation, and dispersion of wave propagation through the atmosphere. The properties of nonlinearity and attenuation of the propagation solver are validated in this subsection.

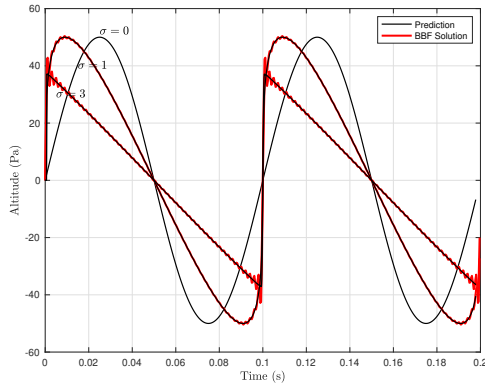
For the nonlinearity validation, the propagation solver is compared with the BBF [128]. A plane wave, defined as $p(0, t) = p_0 \sin 2\pi f t$, is employed as the source signal for both BBF solution and the propagation solver, where p_0 is the initial amplitude and f is the frequency of the signal. The numerical implementation of the BBF from Miller [14] work is employed to obtain the numerical solution with various conditions. In the solver-BBF comparison, attenuation and

dispersion terms are set to zero so that we may first analyze the nonlinear effects. A validation matrix is used to investigate the various propagation conditions as shown in Table 3-3. Three values of p_0 are selected as 50 Pa, 250 Pa, and 2500 Pa, which correspond to the Sound Pressure Level (SPL) at 124.9485 dB, 138.9279 dB, and 158.9279 dB, respectively. The frequencies of the test signal are 10 Hz, 50 Hz, and 500 Hz. The shock formation distance is obtained by using the equation $\bar{x} = (\rho c_\infty^3)/(2\beta_b p_0 \pi f)$ for each case listed in Table 3-3, where $\beta_b = 1.2$ is the nonlinear coefficient. Besides the original signal, predicted waveforms at two non-dimensional shock distances, $\sigma = 1$ and $\sigma = 3$, are captured to compare with the BBF solution. In Fig. 3-7, six cases from the validation matrix are demonstrated. In each subfigure, the y-axis is the amplitude with unit of Pascal, and the x-axis is the time. The BBF solution is constructed with twenty harmonics. The overall performance of the prediction solver is satisfying since the predictions agree well with the BBF solution in amplitude and phase as the average L2 norm of the error is 1.82% for the \bar{x} cases. With the Lanczos filter applied after the time marching in the propagation solver, the Gibbs' phenomenon is eliminated. The Gibbs' phenomenon is apparent in the BBF evaluation due to the use of a limited number of harmonics.

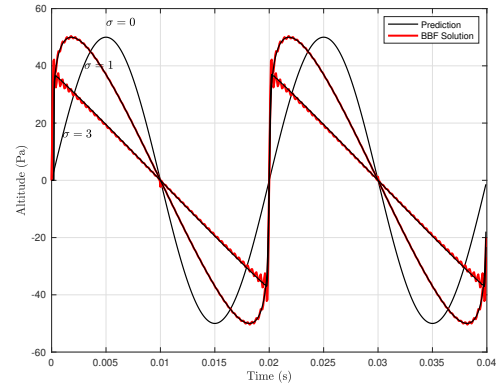
To validate the attenuation effect of the propagation solver, we set the nonlinear term and dispersion terms to zero for plane wave propagation. The test signal is a 2000 Hz tonal sound wave propagating at sea level with an ambient speed of sound of 343 m/s. The results are shown in Fig. 3-8, where y-axis is the SPL and the x-axis is the frequency. The black spectrum and red spectrum are obtained at propagation time $t = 2$ s and $t = 5$ s, respectively. From Sutherland and

Table 3-3. Nonlinearity Validation Matrix.

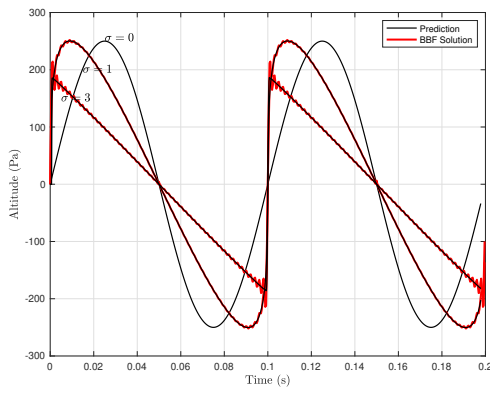
p_0 (Pa)	SPL (dB)	f (Hz)	Shock Distance (m)	σ_1	σ_2	σ_3
50	124.9485	10	12984.105	0	1	3
50	124.9485	50	2596.821	0	1	3
50	124.9485	500	259.682	0	1	3
250	138.9279	10	259.682	0	1	3
250	138.9279	50	519.364	0	1	3
250	138.9279	500	51.936	0	1	3
500	158.9279	10	1298.411	0	1	3
500	158.9279	50	259.682	0	1	3
500	158.9279	500	25.968	0	1	3



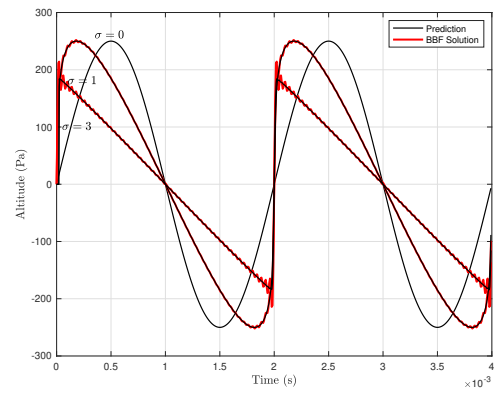
(a) 50 Pa and 10 Hz



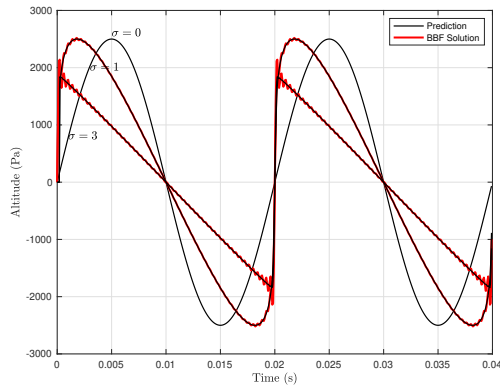
(b) 50 Pa and 50 Hz



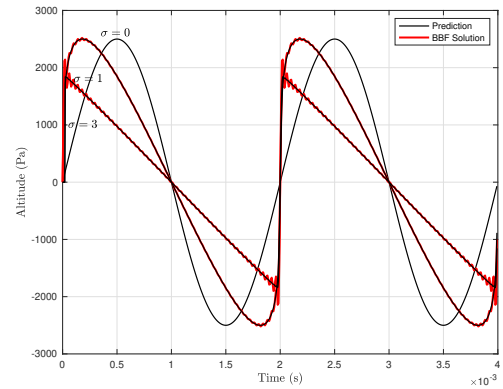
(c) 250 Pa and 10 Hz



(d) 250 Pa and 500 Hz



(e) 2500 Pa and 50 Hz



(f) 2500 Pa and 500 Hz

Figure 3-7. Nonlinear effect validation of the propagation solver by comparing with the BBF solution at different σ .

Bass [68] model, the attenuation for this condition is 6.96 dB/km. From $t = 2$ s to $t = 5$ s, the SPL reduction obtained from the prediction is 7.2356 dB, which is 0.074 dB higher than 7.1618

relative to the Sutherland and Bass model. The error is less than 1.02 %, we believe that the atmospheric attenuation model is implemented correctly.

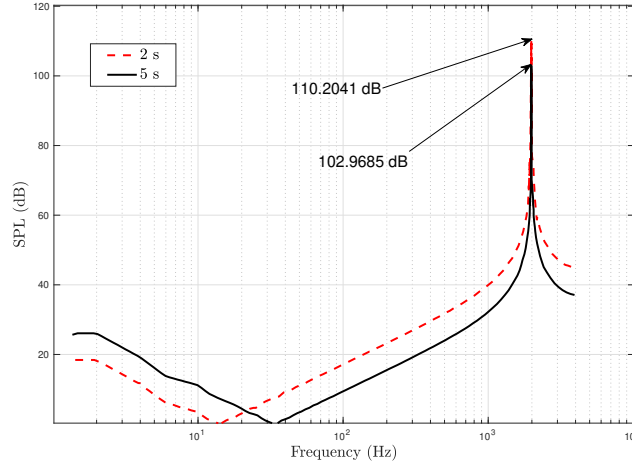


Figure 3-8. Absorption Coefficient Validation.

As the nonlinearity and attenuation components of the solver are validated, the propagation solver is ready for further studies. In the next section, the preliminary results of the ray tracing solver and related propagation solver are demonstrated.

3.2 Preliminary Results of the Numerical Solver

As the numerical solvers are validated, the assembled numerical solver is exercised with realistic test cases. We choose four positions as example infrasound source locations, and all the source locations are at same height of 100 m to simulate the height of a real tornadic infrasound source. Infrasound sources reside within the entire height of the tornado (approximately 5 km), but are dominant below 1 km. Instead of the actual source location, the initial source location of the the propagation solver is 1 km away from the tornado to satisfy the far-field propagation assumption. The propagation path is simulated and obtained by the ray tracing solver as demonstrated in Subsection 3.2.1. Related signal propagation is predicted by the propagation solver (Subsection 3.2.2). The single frequency infrasound, mathematically modeled broadband tornadic infrasound, and the CFD simulated tornadic infrasound are employed as the source signals.

3.2.1 Ray Tracing Results for Propagation Test Cases

In the first step, the acoustic ray tracing solver is applied to find the acoustic ray path that connects the source location and the observer. Four airports, Kansas City International Airport (Kansas City, IATA: MCI), Will Rogers World Airport (Oklahoma City, IATA: OKC), Ted Stevens Anchorage International Airport (Anchorage, IATA: ANC), and José Martí International Airport (Havana, IATA: HAV), are chosen as the infrasound source locations. The OKC and MCI are located in the Tornado Alley, while the HAV and ANC represent the tropical and sub-arctic region. The date and time of the propagation is set to 12:00+00 on March 1st in 1990 for all the propagation cases. In this subsection, the ray tracing results of the HAV case and MCI case are demonstrated in Fig. 3-9 and Fig. 3-10. The x -axis is the horizontal distance from the source

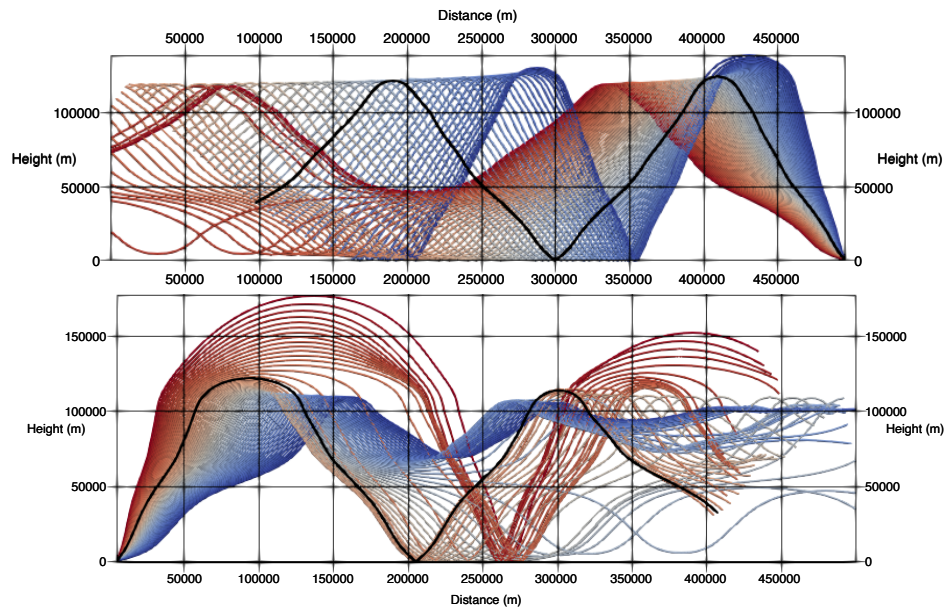


Figure 3-9. Acoustic ray tracing result of the HAV case (Up: Westward propagation, Down: Eastward Propagation).

location, and the y -axis is the altitude. The top subfigures are the westward propagation for both figures, while the bottom subfigures are the eastward propagation. The rays' different colors represent different launching angles. The launching angles are from 30 degrees to 60 degrees for eastward propagation with one degree launching angle increments and 120 degrees to 150 degrees for the westward propagation with one degree launching angle decrements. For the HAV region,

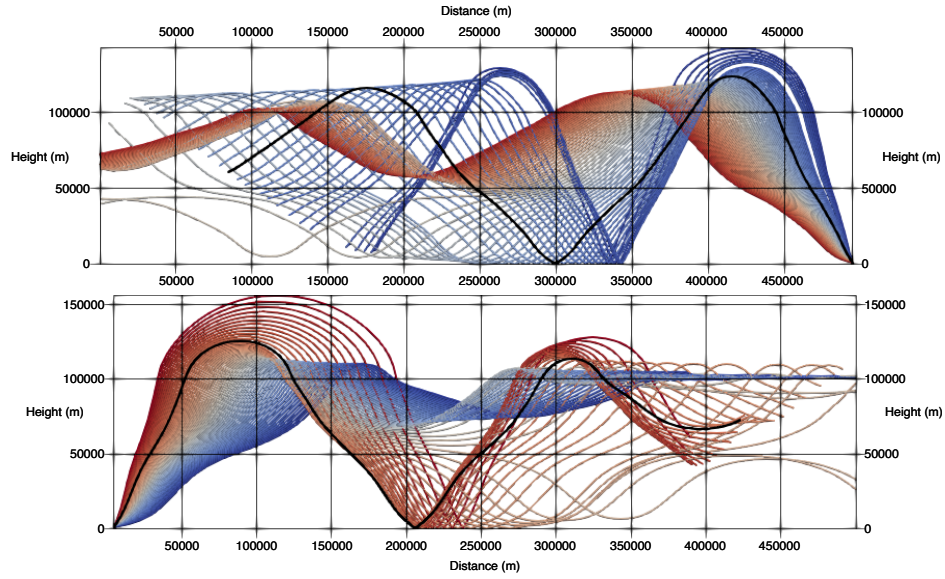


Figure 3-10. Acoustic ray tracing result of the MCI case (Up: Westward propagation, Down: Eastward Propagation).

the eastward propagation is upwind because of a northeast trade wind. At 300 km east from the HAV source location, a shadow zone appears. The observers are located on the ground and 200 km from the source locations. Because of the stronger east trade wind in HAV than MCI, the high launching angles rays in HAV trend to generate a larger shadow zone than MCI case. The black ray paths are those that connect the sources and observers. The launching angles of the black rays are 53° , 132° , 58° , and 127° for the HAV eastward, HAV westward, MCI eastward, and MCI westward cases. The black ray paths, related wind profiles, and temperature data are transferred into the propagation solver as input arguments.

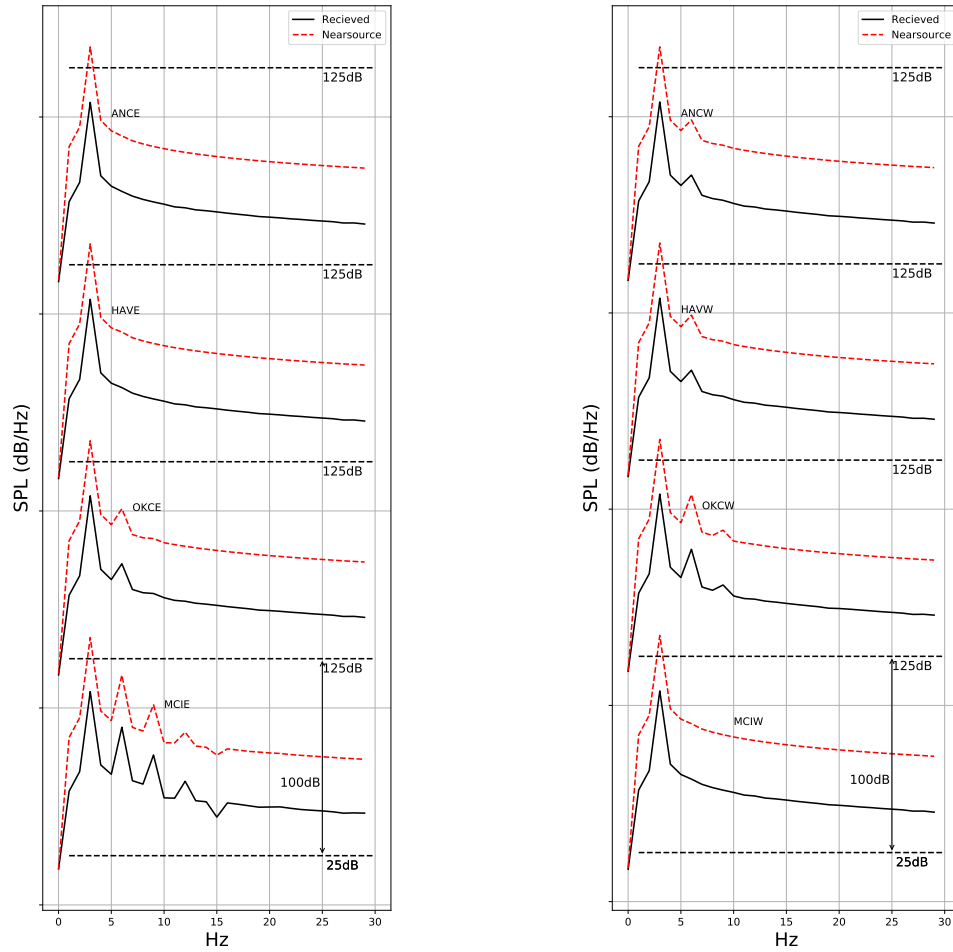
3.2.2 Propagation Solver Case Study without Turbulent Model

As the ray paths are obtained from the ray tracing solver, the propagation solver is now used to predict the received waveform at the observer location. The propagation solver is tested with four different source signals: a 3 Hz 140 dB sine wave, a 5 Hz 120 dB sine wave, a modeled rebuild tornadic broadband infrasound signal, and a tornadic infrasound signal obtained from a CFD simulated tornado [129]. The terms of the nonlinearity, geometric spreading, attenuation, and dispersion are all switched on for these test cases.

To demonstrate the nonlinear effects, we propagate an intensive 140 dB sine wave at 3 Hz in four regions with both eastward and westward propagation, and the results are shown in Fig. 3-11. In this figure, the left column contains the westward propagation cases and the right column contains the eastward propagation cases. For the HAV, OKC, and ANC cases, the eastward propagation are the upwind propagation, while the westward propagation is the upwind propagation for MCI case. The red dash line represents the signal's spectrum after 5 s of propagation, which we call the near-source signal. The black line is the received signal at the observer. Notable nonlinear phenomena are shown for all the upwind propagation cases, as evidenced by the generation of harmonics. For the MCI case, the upwind propagation altered by the nonlinear propagation effect which causes three harmonics at 6 Hz, 9 Hz, and 12 Hz, while the downwind case in MCI is a pure linear propagation. To investigate the different nonlinear effects in MCI's upwind and downwind cases, the nonlinear coefficients along the ray paths are shown in Fig. 3-12. The difference of nonlinearity between the upwind and downwind propagation can be understood clearly with this figure. The y-axis is the nonlinear coefficient, and the x-axis is the propagation time. The red dash line in Fig. 3-12 is the nonlinear coefficient of the downwind propagation, and the black line is the upwind case. After 10 s of propagation, the nonlinear coefficient of the upwind propagation is approximately 100 times larger than the downwind case. This can be explained with the ray tube concept, where the ray tube is compressed as acoustic wave propagates in the upwind direction, which results in a smaller convective volume and greater nonlinear coefficient.

For tornadic infrasound, the SPL is unlikely ever to reach 140 dB, so we use a 5 Hz and 120 dB sine infrasound as the source signal and propagate it in the MCI region. The spectra for this case are shown in Fig. 3-13. For this 120 dB case, there is no apparent nonlinear effect for both upwind and downwind cases. The geometric spreading and attenuation effects have the largest effect on the infrasound propagation.

Besides the single frequency test, we also conduct a broadband signal propagation test. To build a broadband tornadic infrasound signal, we use the mathematical model of Talmadge and



(a) Westward propagation

(b) Eastward propagation

Figure 3-11. A 140 dB and 3 Hz sine wave signal propagation.

Waxler [130]. The modeled Stillwater tornadoes infrasound spectrum [130] is applied, and the rebuilt infrasound propagation results in MCI region are shown in Fig. 3-14. In the left subfigure of Fig. 3-14, the red spectrum is captured at propagation time $t = 100$ s, and the black spectrum is obtained at the observer location. The right subfigure is the pressure time history related to the spectra in the left subfigure, with the dual y-axis of different amplitude magnitudes. Similar to the

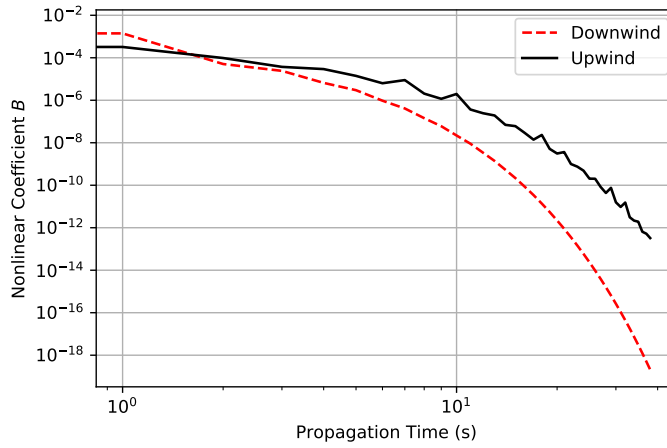
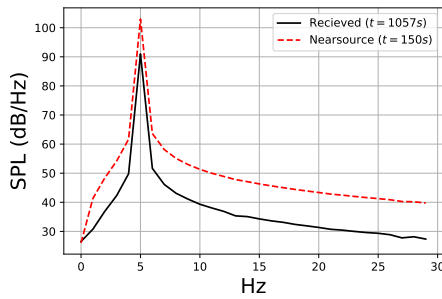
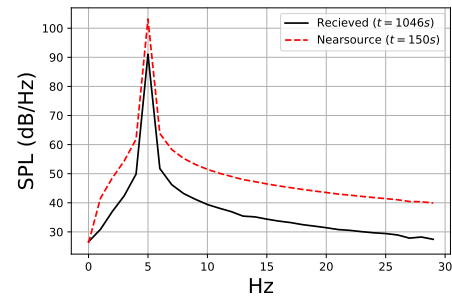


Figure 3-12. Nonlinear coefficient in the near source region (MCI).



(a) Upwind

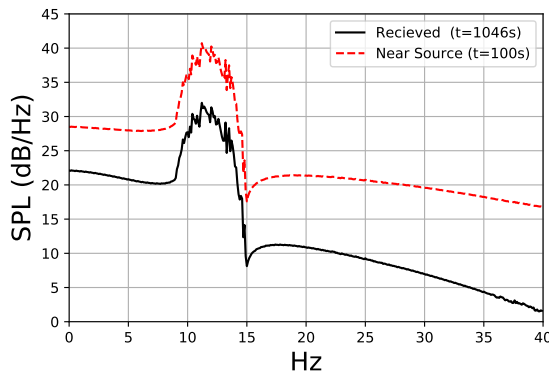


(b) Downwind

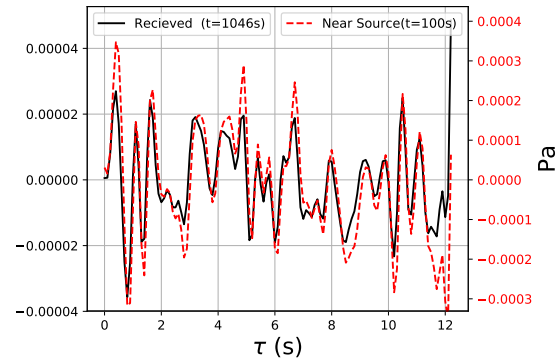
Figure 3-13. 120 dB 5 Hz signal propagation in MCI area.

120 dB and 5 Hz sine wave case, the nonlinear effects are negligible for this broadband signal's propagation. The peaks near $\tau = 0.1$ s, $\tau = 4.8$ s, and $\tau = 6.3$ s decrease significantly larger (23.3950 dB) than the peaks at other location, which is caused by the atmospheric attenuation, since the coefficient of attenuation increases with increasing frequency.

The source signal of the last test case is modeled from a CFD simulated tornado [129] by using Lighthill's acoustic analogy [50]. The simulated tornado is shown as the left subplot in Fig. 3-15 as a u -component contour. The radial vibration of the vortex structure located at the height range from 100 m to 200 m contributes to the major infrasound energy. The spectrum is shown on the right. Two humps are clearly captured in the spectrum at frequencies of 6 Hz and 7 Hz.

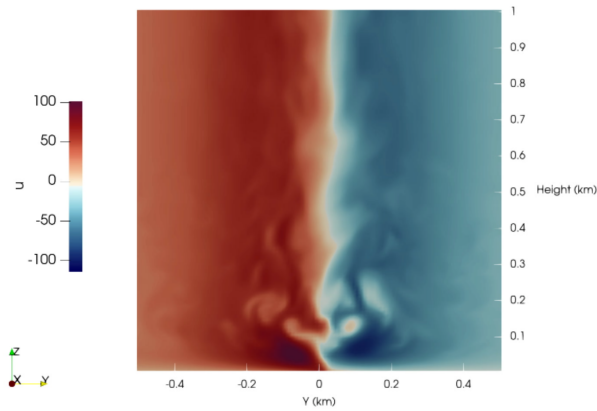


(a) Spectrum

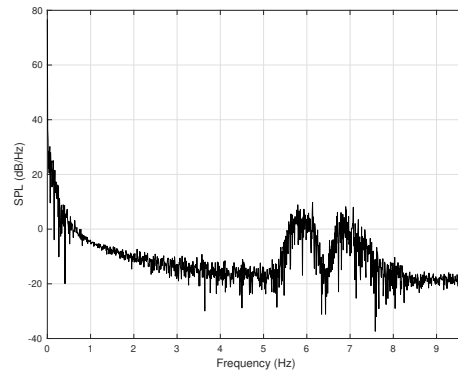


(b) Pressure Time History

Figure 3-14. Broadband signal propagation in MCIE case.



(a) U -component velocity contour



(b) Infrasound spectrum

Figure 3-15. CFD simulated tornado and the spectrum of its tornadic infrasound, courtesy of Penn State University. .

The CFD simulated tornadic infrasound signal is input into the propagation solver and propagates in the HAV region. The pressure time history of the source signal and the received signal are shown in Fig. 3-16 by the black and red lines, respectively. Similar to the pressure time history of the mathematically modeled source signal, the major effects on the propagation are the geometric spreading and the atmospheric attenuation.

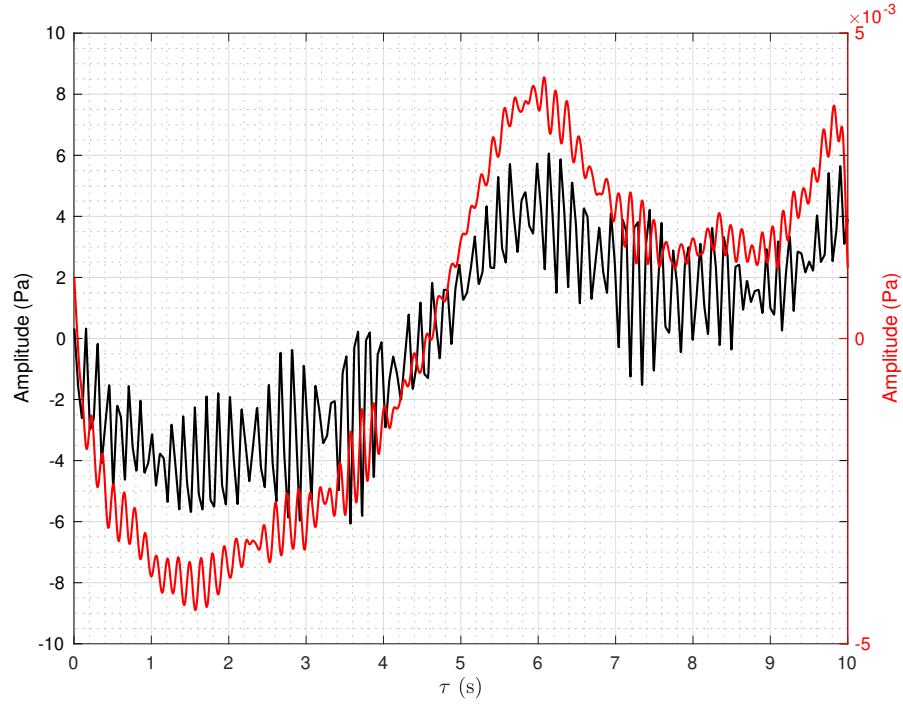


Figure 3-16. CFD tornadic infrasound signal propagation result; Black: source signal, Red: signal at observer.

3.3 Summary

In this chapter, the numerical techniques described in Chapter 2 are implemented and validated. The ray tracing solver is validated by comparing with the Hallberg et al. [82] solver. Nonlinearity and atmospheric attenuation of the propagation solver are validated with the BBF and Sutherland and Bass [68] model, respectively. Four regions' acoustic ray tracing simulations are conducted with HWM93 and NRLMSISE-00 models. Four types of source signals are used with the propagation solver, and the related results are demonstrated and analyzed. For the tornadic infrasound propagation, the nonlinearity is no longer the primary effect to be investigated. While the attenuation is the main focus for the tornadic infrasound propagation, the turbulent scattering attenuation will be studied by experimental techniques in Chapter 4. These measurements will then be used to improve the prediction of the turbulent scattering effect.

CHAPTER 4

WIND TUNNEL EXPERIMENTS AND MEASUREMENTS

To evaluate the effect of turbulence on long-range propagation, a series of experiments are conducted to investigate the turbulent scattering models for acoustic propagation (Chapter 2). The experiments are designed to propagate a sound signal through the UFBLWT with different turbulent flows. By recording the alternation of the sound signal, the turbulent effects on acoustic propagation can be determined. In the experimental campaign, there are three major objectives to be measured accurately, and these objectives are shown as following.

- The first objectives is the initial acoustic source signal. This signal is launched by a commercial speaker, which introduces distortion to the signal because of the speaker's impulse response. Therefore, we tested the speaker in an anechoic chamber to obtain the precise test signal without any reflection and environmental disturbance. The UFBLWT is acoustically characterized to avoid the interaction between wind tunnel background noise and the initial acoustic source signal. Once the test signal and the UFBLWT are prepared for the acoustic test, the test signal is propagated through carefully-controlled turbulent flows in the UFBLWT.
- The second objects is the turbulent statistics, which are measured by a velocity probes' system. These probes are mounted on an automated mechatronic gantry system that moves in three dimensions, and are controlled from outside the tunnel. In this manner, vertical turbulence profiles are measured at a series of locations through the depth of the UFBLWT (from fans to the exit).
- The third objectives is the turbulent-altered acoustic signals, which are recorded by a microphone system during the propagation experiments. These recorded signals are compared with the initial signal to evaluate the physical effects on the propagation.

The entire experimental procedure is constructed in three experimental stages corresponding to the three objectives, and these stages are described in detail in this chapter.

In this chapter, the introduction of the UFBLWT and anechoic chamber are presented first (in Section 4.1). The three stages of the experiment campaign are introduced separately in Section 4.2, with detailed experiment setups and experimental designs. The results are presented and analyzed in Section 4.3.

4.1 University of Florida Turbulent Boundary Layer Wind Tunnel

The UFBLWT (see Fig. 4-1) is a low-speed wind tunnel with a 6 m wide by 3 m high test section. Eight 1.5 m Aerovent vane axial fans with adjustable pitch blades can generate up to 16 m/s tunnel velocities. The 40 m long tunnel has an adjustable ceiling pitch to regain static pressure

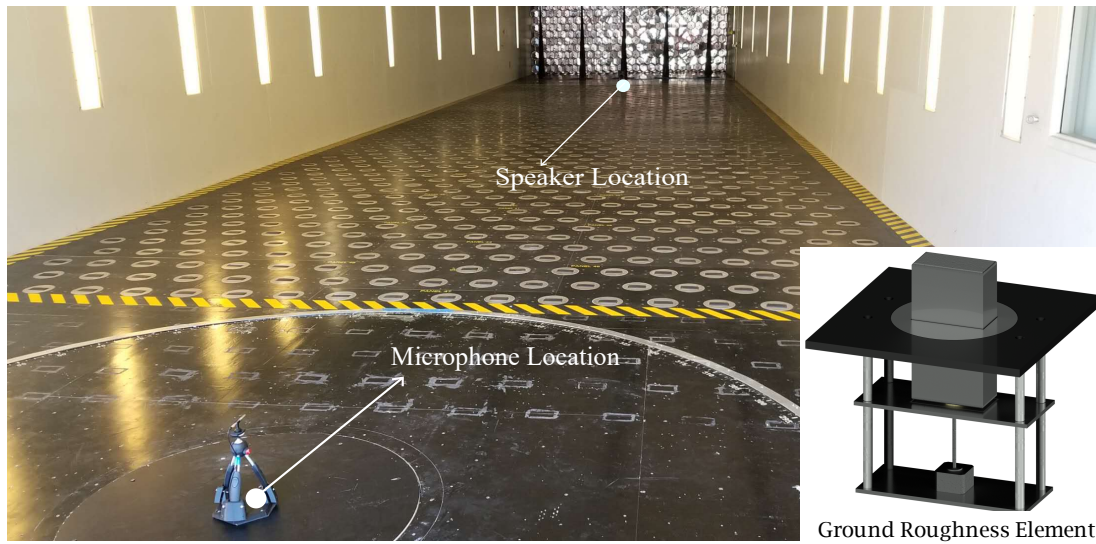


Figure 4-1. University of Florida Boundary Layer Wind Tunnel, acoustic configuration, and a roughness element (Photo courtesy of author).

lost from friction. The floor of the tunnel has mechanical devices (right-bottom corner in Fig. 4-1) that rise to a pre-determined height to control the roughness layer within the turbulent boundary layer (see [131] for details). Roughness elements at the bottom of the boundary layer can be reconfigured to simulate artificial terrain. Many diverse terrain configurations and associated turbulent flows can be rapidly investigated. Each of the 1,116 roughness elements are individually automated to control height and aspect ratio, providing the ability to rapidly reconfigure the tunnel to produce a large range of profiles and scales (see terraformer video at [132]). Validation studies of the flow-field and its relationship to the roughness element configuration have recently been published. These include floor to free stream mean and turbulent velocity for 33 homogeneous terrain configurations [133, 134] and measured longitudinal velocity spectra [135, 133, 131].

The UFBLWT does not have anechoic treatment [136] and is not considered a tunnel that is typically useful for acoustic tests. Wind tunnels created for acoustic testing often have open or partially open test sections [137, 138], anechoic treatment [139], and special baffles to dampen the acoustic waves from the compressor or electric motor system [140, 141]. The present facility is primarily designed to create excellent repeatable measurements of the atmospheric turbulent boundary layer with varying roughness. Roughness elements themselves scatter noise that

propagates throughout the tunnel [142], however, this scattered noise lags the incident wave. Furthermore, the walls of the UFBLWT have very little to no acoustic absorption properties, and therefore we treat them as hard walls that approximate perfectly reflected acoustic waves [143]. Nonetheless, the UFBLWT can be used for acoustic testing to ascertain the alteration of waves by turbulence through a carefully designed experiment, which is described in Subsection 4.2.1 and Subsection 4.2.3.

Near the exit of the tunnel, a meteorological station is used to monitor the local atmospheric conditions. The ambient pressure, humidity, and temperature data are collected during the tests from the meteorological station measurements.

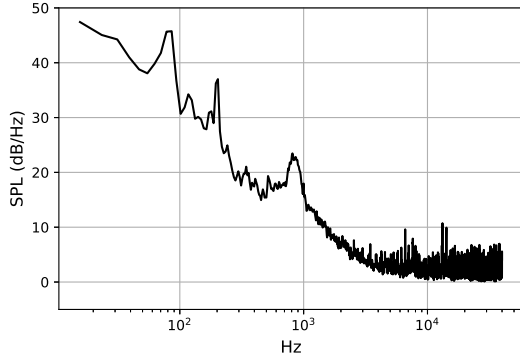
4.2 Stages of the Experiment Campaign

4.2.1 Stage 1: UFBLWT Acoustic Conditions, Test Signal Design, and Anechoic Chamber Test

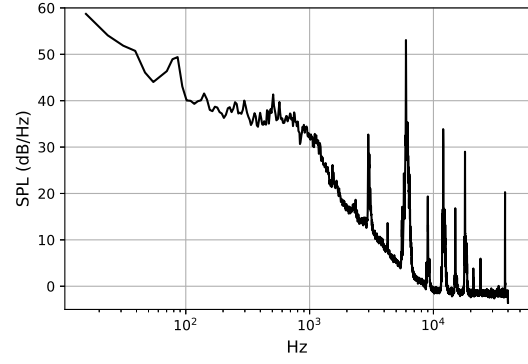
We first characterize the background noise of the wind tunnel. The background noise spectra are shown in Fig. 4-2 with the reference wind speeds of 3.474 m/s, 6.853 m/s, and 10.619 m/s, respectively. The corresponding wind tunnel RPM are 240, 480, and 720. The four spectral measurements within the tunnel test section show significant broadband SPL increases from low RPM to high RPM, while the peaks at 3 kHz, 6 kHz, and 9 kHz are captured and these peaks stay nearly at the same level regardless of the RPM variation. The broadband background noise increase of the tunnel is primarily due to the turbulence within the tunnel. The characteristic peak frequencies may due to the electric motors and the fan blades.

After the background noise and background characteristic frequencies are obtained, a test signal is designed to remove the acoustic reflection and the background noise in the wind tunnel. The test signal is produced by a speaker system, so a speaker test is also necessary to obtain the accurate output of the speaker in the anechoic condition.

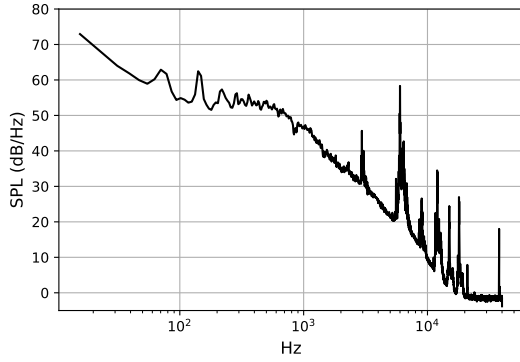
The test signal is a lumped sound of a series of single cycles sine waves. The sine waves are



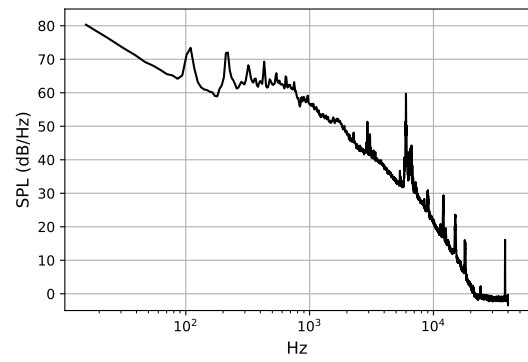
(a) Reference velocity = 0 m/s



(b) Reference velocity = 3.474 m/s



(c) Reference velocity = 6.853 m/s



(d) Reference velocity = 10.619 m/s

Figure 4-2. Example of four different RPMs wind tunnel background noise spectra.

constructed as

$$S_s(t) = \begin{cases} \sin(2\pi f_1 t), & 0 \leq t < 36; \\ \sin(2\pi f_2 t), & 36 \leq t < 72; \\ \sin(2\pi f_3 t), & 72 \leq t < 108; \\ \sin(2\pi f_4 t), & 108 \leq t < 144, \end{cases} \quad (4-1)$$

where $f_1 = 800$ Hz, $f_2 = 1250$ Hz, $f_3 = 1600$ Hz, and $f_4 = 2000$ Hz, respectively. To obtain the single cycles, a window is applied by using Heaviside function as

$$W(t) = \begin{cases} H(t - N_1) - H(t - N_1 - \frac{1}{800}), & t < 36; \\ H(t - N_2) - H(t - N_2 - \frac{1}{1250}), & 36 \leq t < 72; \\ H(t - N_3) - H(t - N_3 - \frac{1}{1600}), & 72 \leq t < 108; \\ H(t - N_4) - H(t - N_4 - \frac{1}{2000}), & 108 \leq t < 144; \end{cases} \quad (4-2)$$

where $H(x)$ is the Heaviside function. N_1 , N_2 , N_3 , and N_4 are constant coefficients and equal to 0, 36, 72, and 108, respectively. By multiplying the window function W with the S_s signal, the test signal S_t is obtained as

$$S_t(t) = W(t)S_s(t). \quad (4-3)$$

and the structure of the test signal is shown in the Fig. 4-3. For each frequency, there are 36 repeated single cycles, which are combined with blank periods to assemble the one-second segments for each single cycle. In Figure 4-3, the 36 single cycles of the 800 Hz are in period 3 s to 39 s, while period 39 s to 75 s is the 1250 Hz, period 75 s to 111 s is the 1600 Hz, and 111 s to 147 is the 2000 Hz, respectively. At the end of the signal, there are four reminder tones indicating the end of the signal.

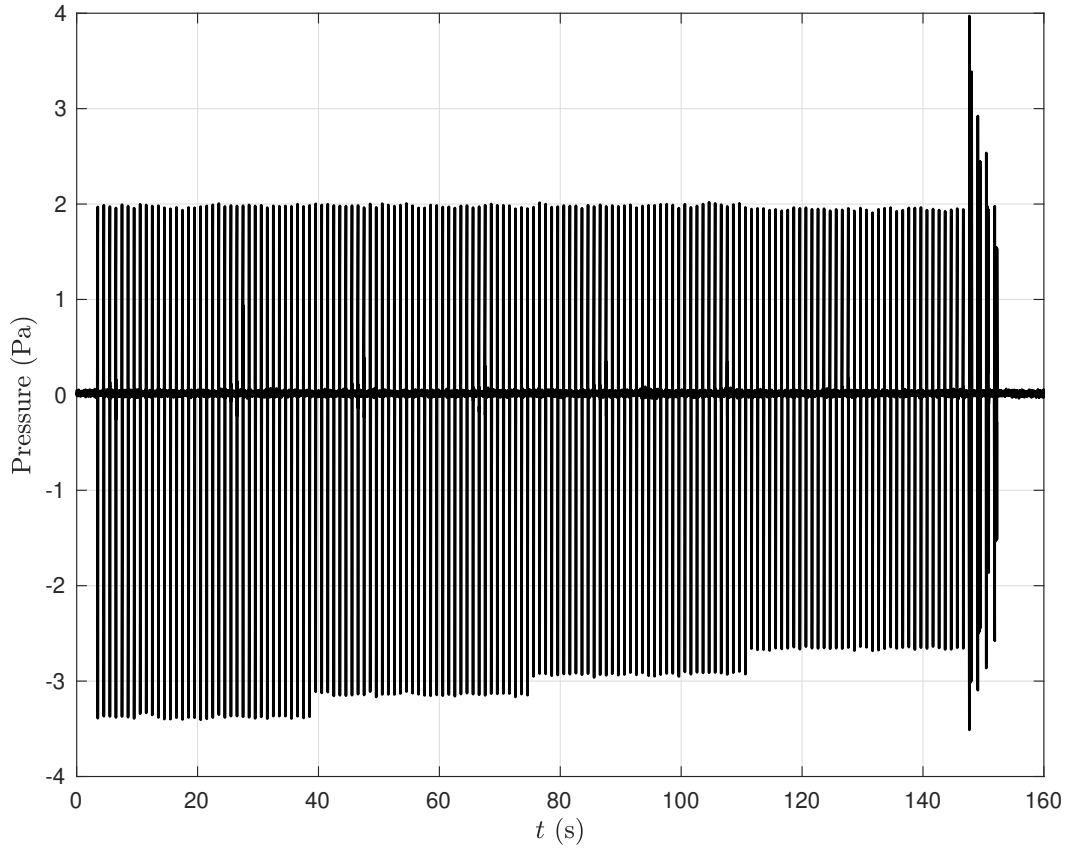


Figure 4-3. Raw anechoic chamber source signal recording at 2 m from the speaker.

This single-cycle test signal is designed to remove the acoustic reflections by producing phase difference between the direct wave and reflected waves. As the reflected wave travels longer distance than the direct wave, the arriving time of the reflected wave is later than the direct wave. If the additional propagation distance caused by reflection is larger than the wave length of the test signal, the phase difference can guarantee a separation in time between the direct wave and reflected waves. To eliminate the background noise, 36 identical single cycles are played for each frequency. By taking the ensemble average of the single cycles, the turbulence-induced background noise can be removed efficiently. With this single-cycle test signal, the reflection and background noise caused by the wind tunnel can be countered, and the source signal can be extracted at the measurement location at the tunnel test section before reflections arrive.

The test signal is coded within a MATLAB script, and played by a commercial speaker. To obtain the accurate output sound of the speaker, we conducted a speaker test in the anechoic chamber as shown in Fig. 4-4. The anechoic chamber is located in the UF Mechanical and



Figure 4-4. Acoustic system (Left: speaker; Right: microphone) in anechoic chamber with the propagation distance = 3 m (Photo courtesy of author).

Aerospace Engineering Building A. The chamber is designed for the open-jet aeroacoustic test [144]. Anechoic treatments are applied to all the sidewalls, including the floor and the ceiling to minimize the wall reflection in the chamber. The interior dimensions of the chamber are 5.5 m long by 5 m wide by 2.3 m high, which provides the propagation distance for the speaker test approximately from 1 m to 4 m. Fiberglass wedges enclosed by steel meshes can provide a cut-off

frequency of approximately 100 Hz, which is satisfying because the frequency of the test signal is approximately 1000 Hz. More detailed information can be found in Mathew [145]. During the anechoic chamber test, all the microphone and speaker setups are identical to the following wind tunnel test to generate the identical output of the speaker.

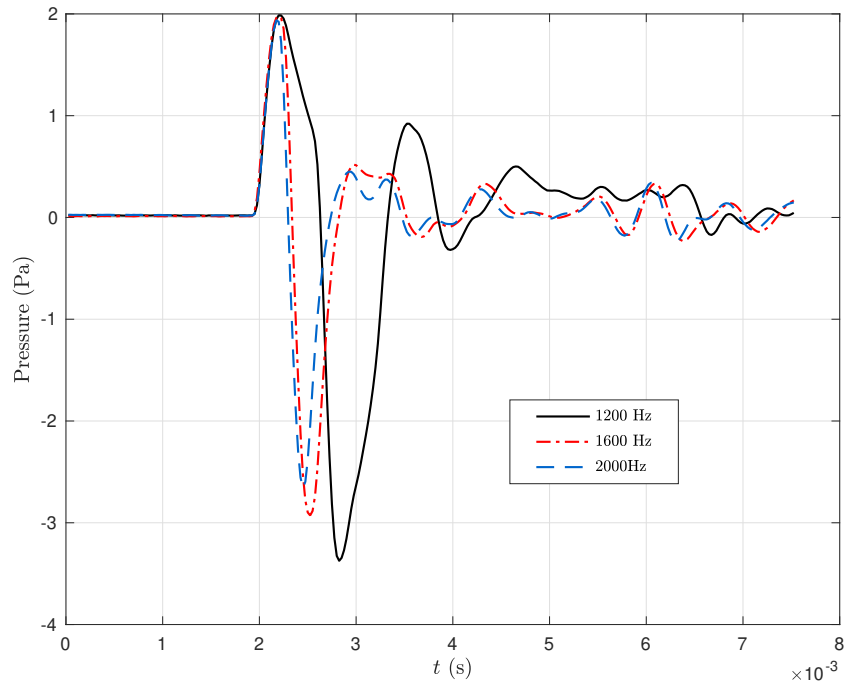


Figure 4-5. Single cycle signals at 2 m away from speaker.

Figure 4-5 shows the measured one-second segments of the test signal from the anechoic chamber speaker test. For the first crests of all the frequencies, the amplitudes are 2 Pa as designed. The impulse responses are observed at the troughs of all three signals, as the amplitudes of the troughs are -3.326 Pa, -2.928 Pa, and -2.657 Pa for 800 Hz, 1250 Hz, and 1600 Hz, respectively. It is expected that the lower frequency signal has a stronger impulse response, as the trough of the 800 Hz signal has the maximum magnitude. In Fig. 4-5, the response time of the speaker is also obtained. The diaphragm takes about 20 milliseconds to rest after the 800 Hz sine pulse, while the response time for 2000 Hz is approximately 13 milliseconds. Because of the impulse response, a zero-padding region created by the Heaviside function is employed to eliminate the leading-and-tailing single cycles' interaction caused by the impulse response. In this

figure, the 800 Hz, 1250 Hz, and 1600 Hz one-second segments are recorded at 2 m from the speaker.

4.2.2 Stage 2: Turbulent Measurement in the UFBLWT

Typically in the UFBLWT, turbulent flow-fields are measured using an automated multi-degree-of-freedom instrument gantry capable of traversing longitudinally, laterally, and vertically nearly the entire length, height, and width of the test section [146]. As shown in Fig. 4-6, the Three-Cobra-Probe [147] (TCP) system is employed. The TCP system consists of three identical Cobra probes from Turbulent Flow Instrument [147] (TFI), and each of the Cobra probes is a fast-response-four-hole probe and capable of measuring the u , v , and w fluctuating velocity components with the sampling frequency at 2 kHz and accuracy of ± 0.5 m/s (TFI Catalogue [147]). All three Cobra probes collect data simultaneously and store the data by using TFI software. In Fig. 4-6, from the bottom to the top, these Cobra probes are labeled Bot, Mid, and Top, respectively. To monitor the vertical cross correlations of the turbulent structure, the spacing between probe Bot and Mid is 40 mm while the spacing between Mid and Top is 60 mm. With this spacing arrangement, we can capture the cross-correlations for 40 mm, 60 mm, and 100 mm vertical length scales. To minimize the interaction and flow-blocking effects, probe Bot is placed horizontally, probe Top is align vertically, and probe Mid is aligned with a 45 degree angle to the ground. The TCP is mounted on the gantry system that is connected to the ceiling of the tunnel. The gantry moves in the streamwise direction of the tunnel. This allows movement of the TCP in the x direction of the tunnel and for turbulence measurements to be made at various positions. An example of a single probe measurement is shown in Fig. 4-7. As shown in this figure, an anisotropic turbulent field is captured as the dependency between the velocity fluctuation and the reference of the rotation.

At the height of $z = 1.48$ m and $x = 2.5$ m, a Pitot tube (Dwyer; Series 600) is used to measure the flow velocity. This Pitot-tube measured velocity is used as the reference wind speed for the test matrices to indicate the working condition of the wind tunnel.

The turbulent test matrix contains 128 tests. Each one of the tests is defined by 4 different

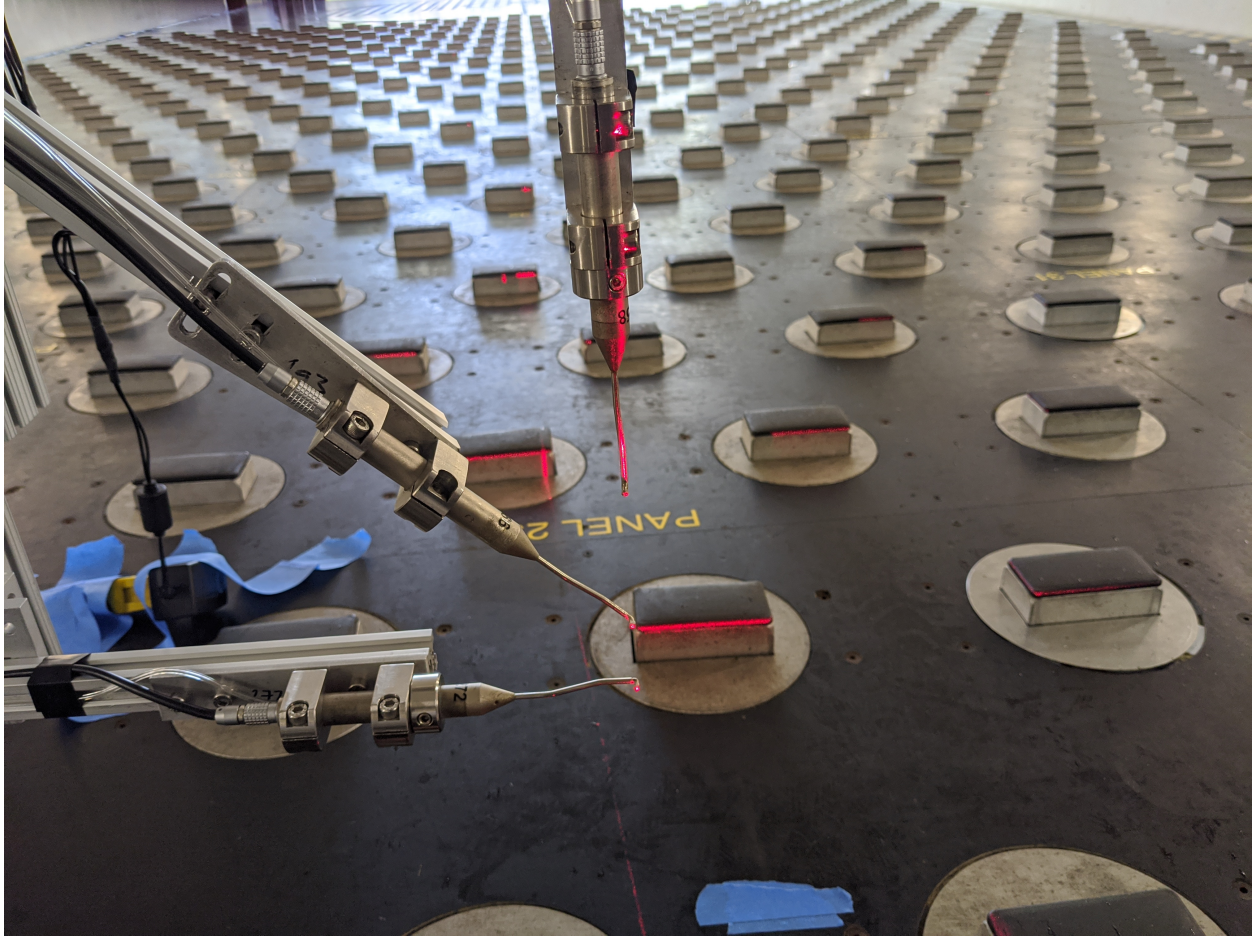


Figure 4-6. Coordinates calibration of Three-Cobra-Probe (TCP) system at $Z = 590$ mm (Photo courtesy of author).

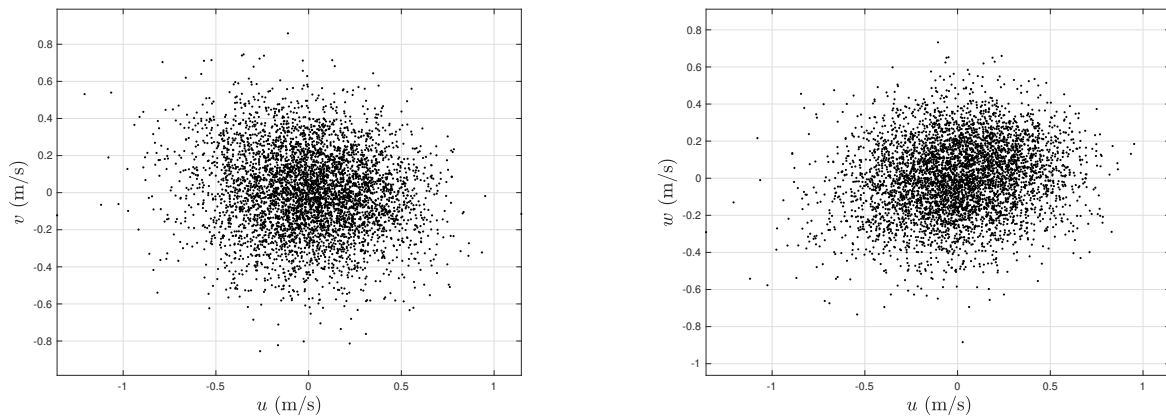


Figure 4-7. Turbulent Field at $EH = 30$ mm, $EL = 900$ mm, and $WS = 5.3$ m/s.

parameters: estimated wind speed (WS), terraformer element height (EH), cobra probe position in x -direction (X) and cobra probe position in z -direction (Z). Because both acoustic and turbulent measurements are conducted in the same coordinates system, the z -location (Z) is used to represent the height of the flow measuring point different from the acoustic test's elevation (EL) shown in Fig. 4-1. To get the turbulent statics along the ray path, Z are kept identical to the EL of the acoustic system. The TCP position in the UFBLWT in the x -direction is defined as the distance from the test section in the UFBLWT to the TCP location in meters. 2 m, 10 m, 16 m, and 22 m were the values of X for all the tests performed. The TCP positions in the UFBLWT in the z -direction are defined as the vertical distance from the floor of the UFBLWT to the center of the horizontal cobra probe Bot. 170 mm, 590 mm, 740 mm, and 900 mm are the positions of the cobra probe Bot in the z -direction for the turbulence tests. In these turbulent tests, there are a total of 4 different estimated reference wind speed in the wind tunnel: 4 m/s, 6 m/s, 8 m/s, and 10 m/s. The terraformer configurations considered in this set are uniform with all the elements with the same height. The terraformer element heights are defined from the floor to the top of the terraformer elements, and are set at 0 mm and 30 mm for turbulent test.

4.2.3 Stage 3: Acoustic Propagation Experiment in the Wind Tunnel

The UFBLWT acoustic experiments are conducted with modified a wind tunnel configuration as shown in Fig. 4-8, along with the coordinate system. The airflow is generated by the fan bank from the left side and combed by the Flow Field Modulator (FFM) and honeycomb. After the Irwin Spires, the airflow is adjusted to a boundary layer profile in vertical direction. Then the boundary layer flow passes the terrainformer to generate different turbulent boundary layers at the test section. The coordinates of the tunnel and the associated dataset is located at the center of the test section, which is also the base of the microphone. We define the upstream direction as x direction, the cross-stream direction as the y direction, and the vertical direction (toward the ceiling of the tunnel), as the z direction. As shown in Fig. 4-8, the distance from the microphone to the speaker is fixed at 22 m in the x direction. There is no refraction of acoustic waves because the temperature variation is negligible in the tunnel. Therefore, the vertical

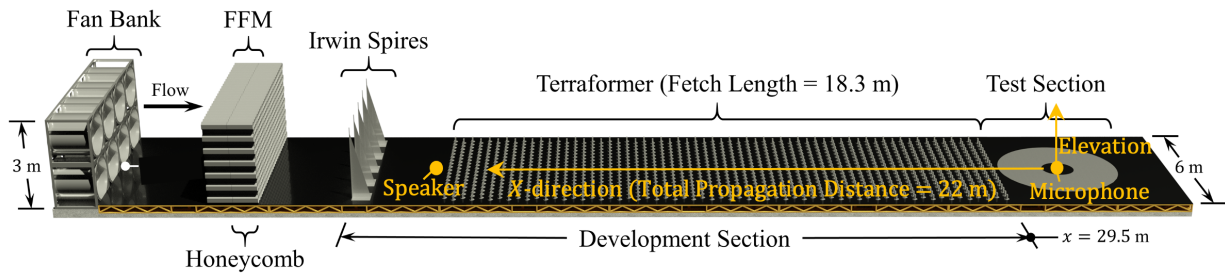


Figure 4-8. Microphone location and speaker location.

positions of the speaker and microphone vary but are always at the same height, which results in a horizontal straight-line ray path of the direct acoustic wave between the speaker face and the microphone. For the acoustic test, we use the elevation (EL) to represent the height of the microphone-speaker system. The EL is adjusted to propagate the test signal through different regions in the turbulent boundary layer. This configuration of the wind tunnel achieves a multi-turbulent conditions for the acoustic propagation test.

The acoustic system consists of the source signal generation system and the sound recording system. The source signal generation system is constructed by a speaker and its supporting structure, along with a controlling laptop. Figure 4-9 shows the speaker system in the UFBLWT. The supporting structure is mounted on the tunnel floor and provides a vertical degree of freedom to the speaker. The audio cable (taped on the floor) connects the speaker to the controlling laptop located outside the wind tunnel near the fanbank. The sound recording system consists of the microphone set, inflow nose-cone, supporting structure, signal amplifier, data-acquisition (DAQ) system, and recording collecting computer in the control room. The microphone set is a GRAS CCP free-field 46BE 1/4 inch microphone set consisting of an IEC 61094 WS3F standardized GRAS 40BE 1/4 inch Prepolarized Free-Field Microphone and a GRAS 26CB 1/4" CCP Standard Preamplifier. The microphone frequency range is 4 Hz to 80 kHz, and the dynamic range is from 35 dB to 160 dB. The microphone is placed at the center of the test section and points in the upstream direction with a zero degree angle relative to the incident acoustic wave. When the wind tunnel flow passes the microphone, the turbulence



Figure 4-9. Speaker at EL = 590 with the supporting system (Photo courtesy of author).

generated by the microphone produces unwanted pressure variations on the microphone diaphragm (see Allen and Soderman [148] for details). Therefore, a GRAS RA0022 1/4 inch nose-cone is placed on the microphone face to reduce the microphone-turbulence interaction noise. Figure 4-10 shows the microphone set mounted on the height-adjustable supporting structure. This structure allow the microphone's height to be adjusted between 0 mm to 1200 mm. A BNC cable connects the microphone to an amplifier, which transmits a voltage signal to a the DAQ system. The acoustic sampling frequency of the DAQ system is 40 kHz, and the DAQ system is controlled by LabView on the computer in the control room. The microphone is calibrated before and after each acoustic test by a GRAS 42AG Multifunction Sound Calibrator. The calibrator produces a sinusoidal signal of 250 Hz (251.19 ± 0.30 Hz) or 1 kHz (1000 ± 1 Hz), at 94 dB (± 0.2 dB) or 114 (± 0.2 dB). The microphone is calibrated by the 1000 Hz signal and use the 250 Hz calibration as a reference. The DAQ records both the voltage in V and acoustic pressure in Pa based on the acoustic calibration. With the wind tunnel configured and acoustic system setup, the acoustic propagation test is conducted based on an acoustic test matrix.

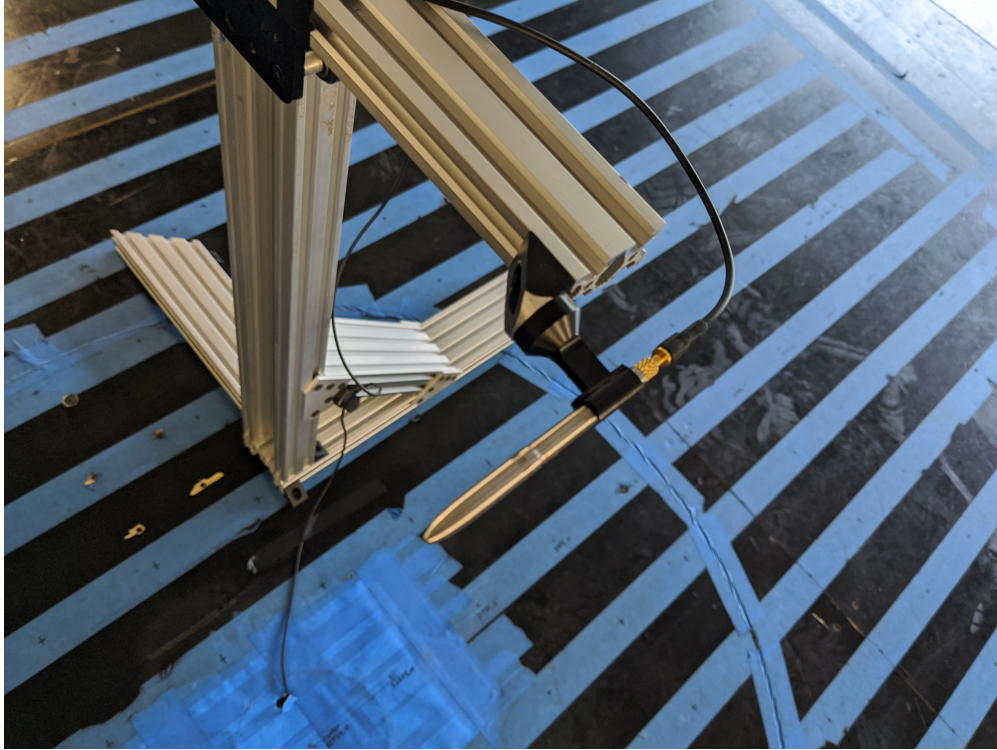


Figure 4-10. GRAS 46BE 1/4 inch CCP free field standard microphone at EL = 590 mm with the supporting system (Photo courtesy of author).

The acoustic test matrix includes 144 different tests. Each one of the tests is defined by 4 different parameters: estimated wind speed (WS), terraformer element height (EH), microphone elevation (EL), and frequency (f). In this set of tests there are a total of 9 different estimated wind speed in the wind tunnel: 0 m/s , 2 m/s , 4 m/s, 5 m/s, 6 m/s, 7 m/s, 8 m/s, 9 m/s, and 10 m/s. The terraformer configurations considered in this set were all uniforms with all the elements at the same height. The terraformer element heights were 0 mm, 10 mm, 30 mm, and 50mm from the floor to the top of the terraformer elements. The microphone elevation in the UFBLWT is defined as the vertical distance from the floor of the UFBLWT to the center of the microphone. 170 mm, 590 mm, 740 mm, and 900 mm were considered as the positions of the microphone in the y direction for the acoustic matrix.

4.3 UFBLWT Experimental Results

As mentioned in the previous section, there are two test matrices for the acoustic and turbulent tests, respectively. Table 4-1 is a summary of these two matrices.

Table 4-1. Acoustic and turbulent test matrices.

Acoustic Test (144 Total Cases)		Turbulent Test (128 Total Cases)	
Elevation (EL) (mm)	170, 590, 740, 900	Z-Location (Z) (mm)	170, 590, 740, 900
Element Height (EH) (mm)	0, 10, 30, 50	Element Height (EH) (mm)	0, 30
Wind Speed (WS) (m/s)	2, 4, 5, 6, 7, 8, 9, 10	X-Location (X) (mm)	2, 10, 16, 20
Frequency (Frq) (Hz)	1250, 1600, 2000	Turbulent Statics (4 Wind Speed Lumped for Each Parameter)	TKE, Time Scale, Integral Time Scale Mean Velocity, Integral Length Scale

In Table 4-1, the parameters for acoustic and turbulent wind tunnel tests described previously are shown with the values for all the tests. All 144 acoustic tests and 128 turbulent tests are included in this table. In this section, the acoustic test results are presented with a post-processing method, and the turbulent measurements are shown, which are used to create the scattering model.

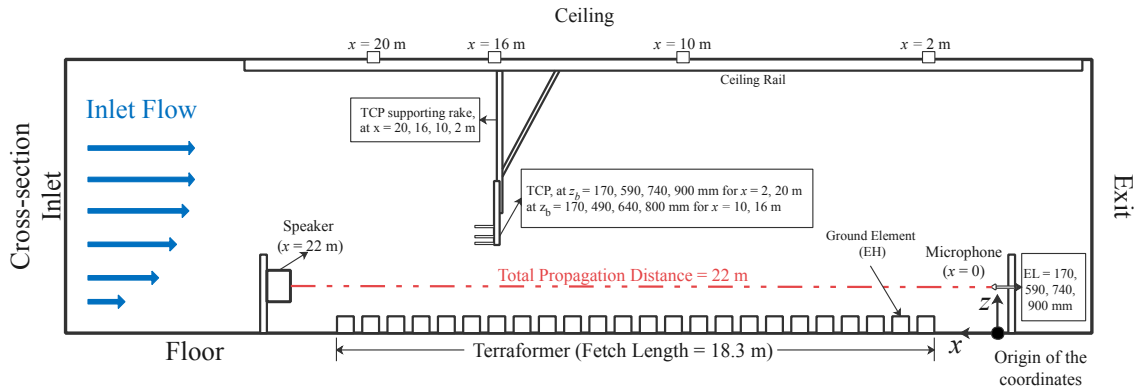


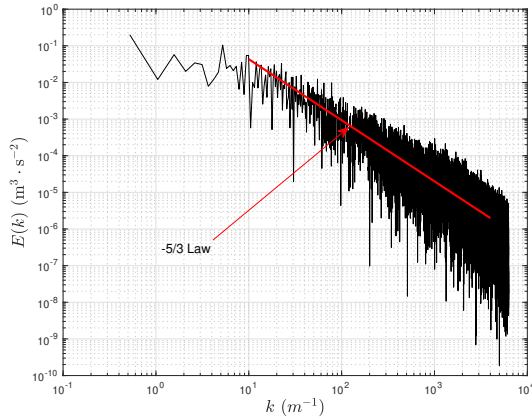
Figure 4-11. Experimental schematic from the UFBLWT acoustic propagation tests.[149]

The experimental procedure is summarized in Fig. 4-11, which shows the setup of the wind tunnel tests. The source signal is generated by a speaker located near the inlet of the wind tunnel, and the microphone is located near the wind tunnel exit. The x coordinate is aligned with the ground center line of the tunnel, and the z direction points to the ceiling. The total propagation distance is 22 m for the acoustic tests. Both the microphone and speaker have adjustable height so

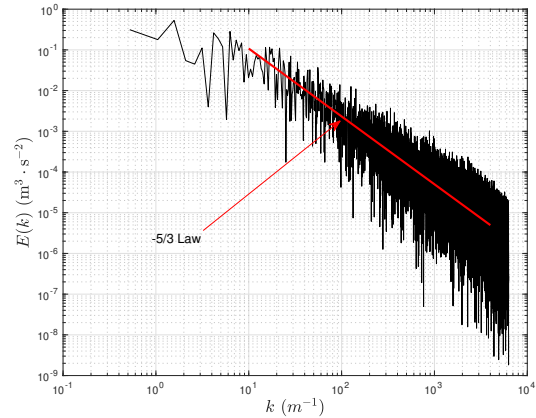
that their elevation height (EL) can vary. The turbulence in the wind tunnel is measured by a Three-Cobra-Probe system (TCP) with both vertical and longitudinal degrees of freedom. The TCP is not present during acoustic tests, so that they do not scatter the acoustic wave. All the ground elements are set at the identical height (EH) to the floor and identical angle to the flow for each test.

4.3.1 Turbulent Measurements

As discussed in the previous sections, the turbulent measurements are conducted in the wind tunnel and the measured data is demonstrated in this subsection. We measure the instantaneous velocity with three orthogonal components. By calibrating zero mean velocity for the y and z direction, we re-orientate the three components to align the TCP with the wind tunnel coordinates in the x direction (Method described in [150]).



(a) PSD of u' at EH = 0, $Z = 170$ mm, WS = 10 m/s, and $x = 2$ m



(b) PSD of u' at EH = 30 mm, $z_b = 170$ mm, WS = 10 m/s, and $X = 2$ m

Figure 4-12. PSD of x -direction turbulent velocity.

Fig. 4-12 presents the power spectral density (PSD) of the fluctuating component of wind in the x direction defined as the turbulent velocity u' for a test at $z_b = 170$ mm, WS = 10 m/s, $x = 2$ m, and EH = 0 and 30 mm. $E(k)$ is the energy-spectrum function and k is the wavenumber of the u -component turbulent velocity. As expected, $k^{-5/3}$ energy decay is observed in the inertial range. Fig. 4-13 illustrates the boundary layer mean velocity profiles at $x = 20$ m, 16 m, 10 m, and 2 m, respectively, with the coordinate system provided in Fig. 4-11. In this figure, the x -axis U_{probe}

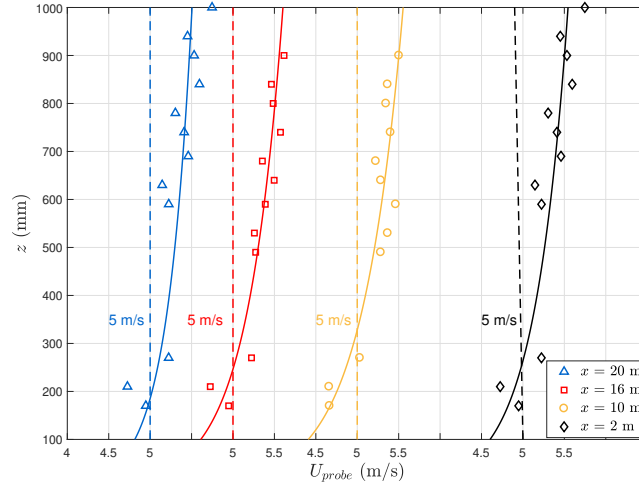


Figure 4-13. Boundary layer profiles along the x -direction, with $EH = 30$ mm and $WS = 6$ m/s.

represents the wind velocity measured by each single Cobra probe. The longitudinal turbulent intensity profiles are shown in Fig. 4-14. The x -axis represents the longitudinal turbulent intensity

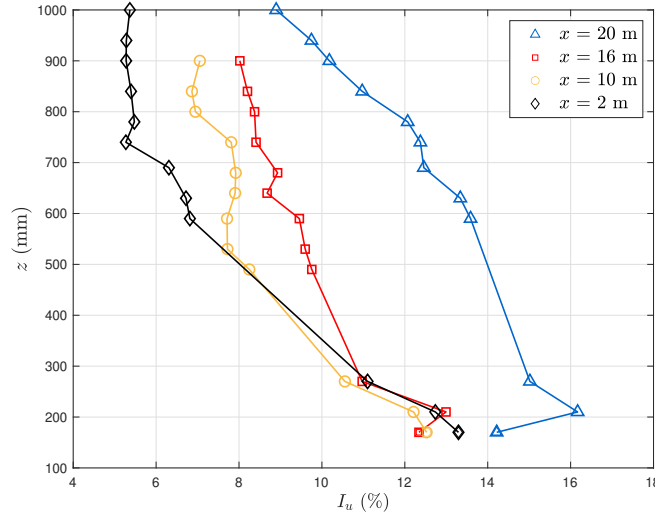


Figure 4-14. Longitudinal turbulent intensity I_u with $EH = 30$ mm, $WS = 6$ m/s.

I_u . From this figure, the turbulent intensity decreases with increasing z for all four x locations. The vertical-spatial-averaged turbulent intensity drops from 12.42% at $x = 20$ m to 7.42% at $x = 2$ m.

We multiply the integral time scale with the mean local velocity to obtain the integral length scale. The integral time scale is captured from the auto-correlation coefficient. The auto

correlations of Probe 272 with the $EH = 30$ mm and $WS = 10$ m/s case are shown in Fig. 4-15.

The left figure is the auto-correlation coefficients obtained at $X = 20$ m, while the right figure is

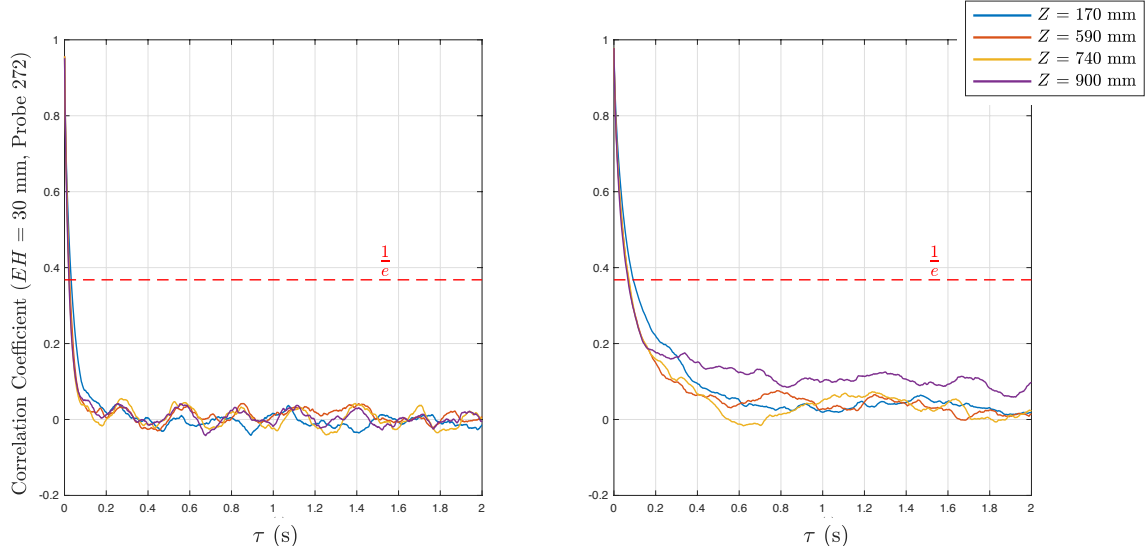


Figure 4-15. Auto correlation with $EH = 30$ mm.

obtained at $X = 2$ m. Here we use the value of $1/e$ to intercept the correlation coefficient plots. A total of 24 cases are selected for the integral time scale calculation, the detailed results are presented in the next chapter.

In Fig. 4-16 the TKE measurements along the ray path are presented for different x locations. The title of each subplot is the x location, and the x -axis represents the U_{probe} and the y -axis is the TKE. At each x location, the TKE decreases with increasing z , which agrees with previous measurements. From the upstream location of $x = 20$ m to the location nearest to test section at $x = 2$ m, the TKE decreases dramatically because of the dissipation effect on the wind tunnel flow. The maximum TKE at the near inlet location ($x = 20$ m) is $0.7756 \text{ m}^2/\text{s}^2$, while the TKE at the location closest to the test section ($x = 2$ m) is $0.1507 \text{ m}^2/\text{s}^2$.

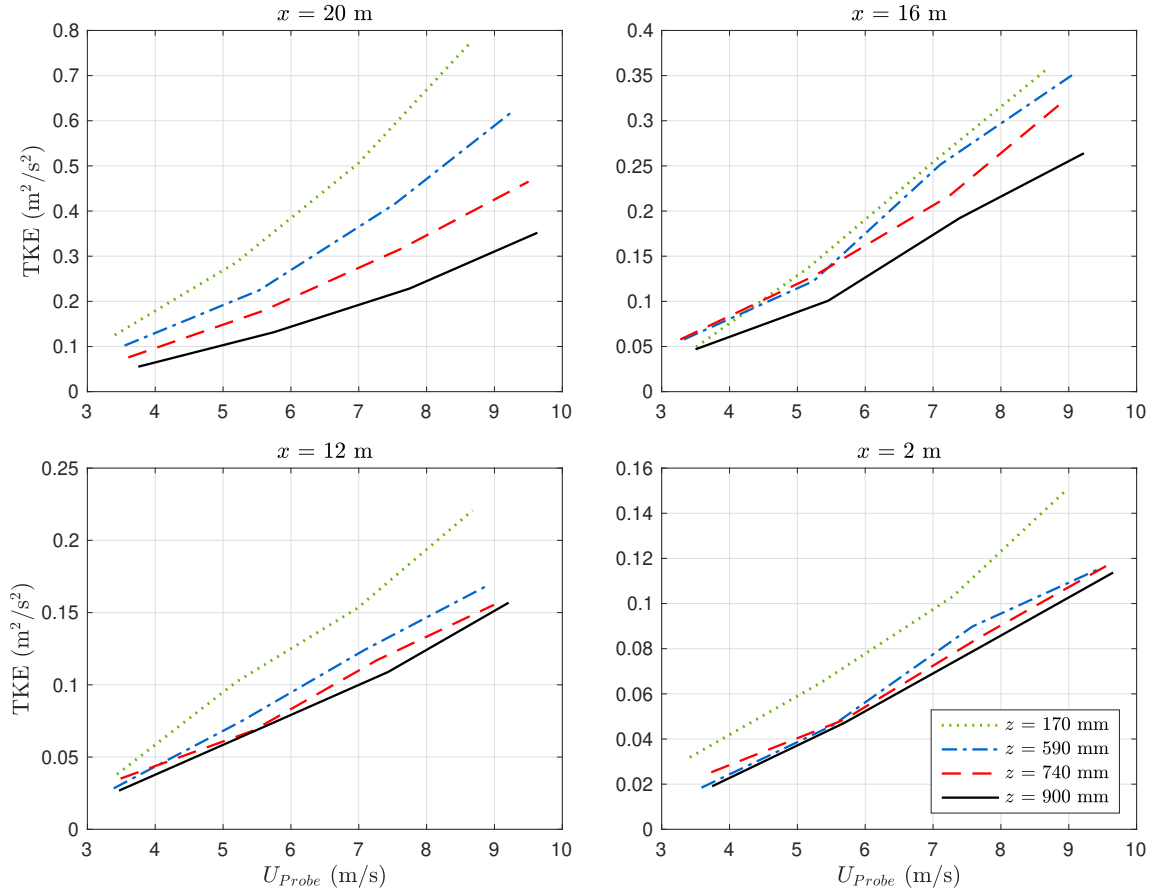


Figure 4-16. TKE measurements with EH = 0.

4.3.2 Acoustic Recording and Post Processing

Figure 4-17 shows an example recording from the wind tunnel with a 3.26 m/s reference wind speed. The entire acoustic signal consists of five parts as designed. The period from 4 s to 40 s is the 800 Hz signal, which contains 36 single-cycle sine waveforms. After the 800 Hz signal, there are 1250 Hz, 1600 Hz, and 2000 Hz signals located at 41 to 76 s, 77 to 112 s, and 113 to 148 s periods, respectively. At the end of the signal, four one-second-long tones with 800 Hz, 1250 Hz, 1600 Hz, and 2000 Hz are set as a reminder to indicate the end of the signal play. The overall structure of the test signal is identical to the recording from the anechoic chamber test in Subsection 4.2.1. The left-side zoom-in figure shows a part of the 1250 Hz signal, in which the periodic signal is clearly observed. The right-side zoom-in figure is an example of recorded

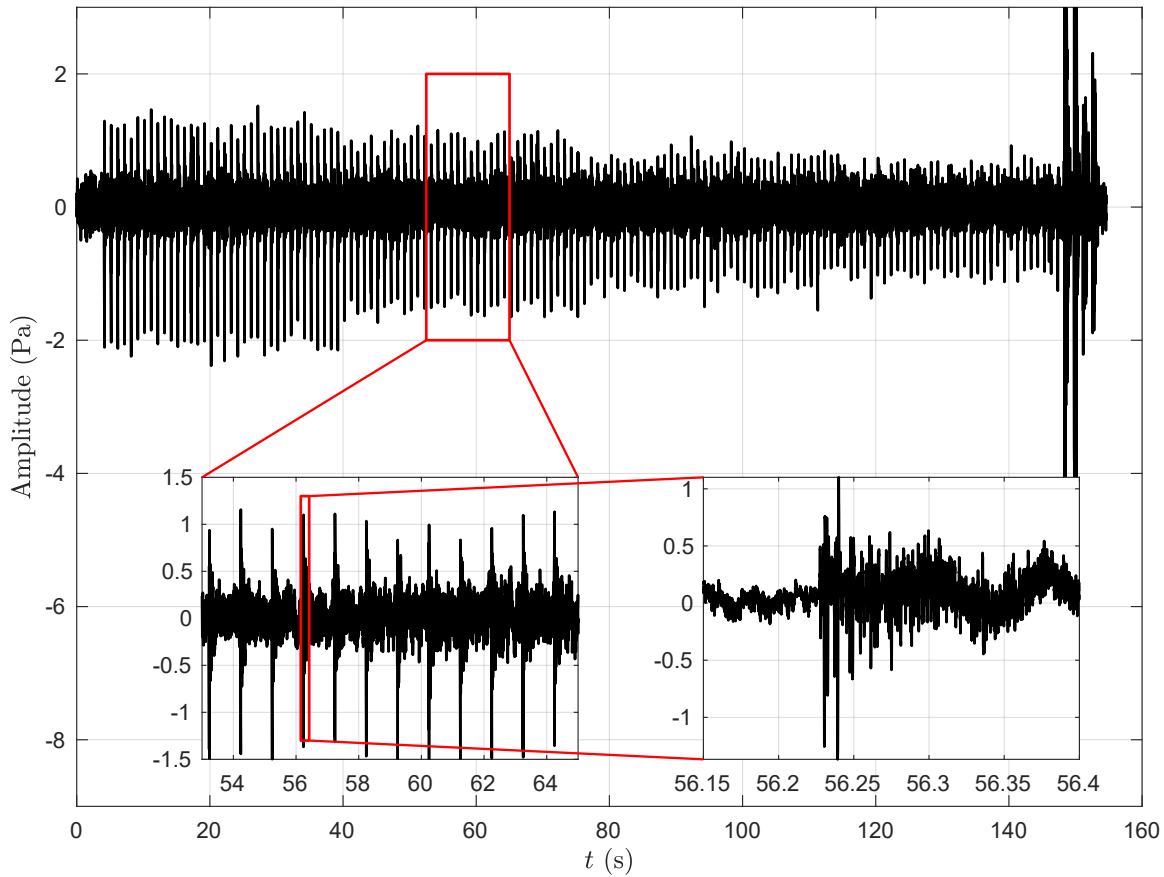


Figure 4-17. Wind tunnel recording with EH = 10 mm, EL = 170 mm, and wind speed = 3.26 m/s.

single-cycle wave segment. For this low wind speed case, the first crest is apparent, even with trailing reflected waves. For higher wind speeds, the background noise rises significantly, and the signal-to-noise ratio can be lower than 1, which makes the first crest hard to recognize. We ensemble 36 single-cycle signals to remove the background noise for 1250 Hz, 1600 Hz, and 2000 Hz signals.

Figure 4-18 is an example of a recorded signal at 1250 Hz. The source signal is identical to the anechoic 1250 Hz signal. By performing an ensemble average, the background noise is reduced significantly. An example is the setpoint 61 case shown in Fig. 4-18. In this case, the signal-to-noise ratio increases from 0.229 to 2.817 for the setpoint 61 case with wind speed at 7.8 m/s. Compared to the anechoic signal, the first sine wave is clearly recognized, along with the

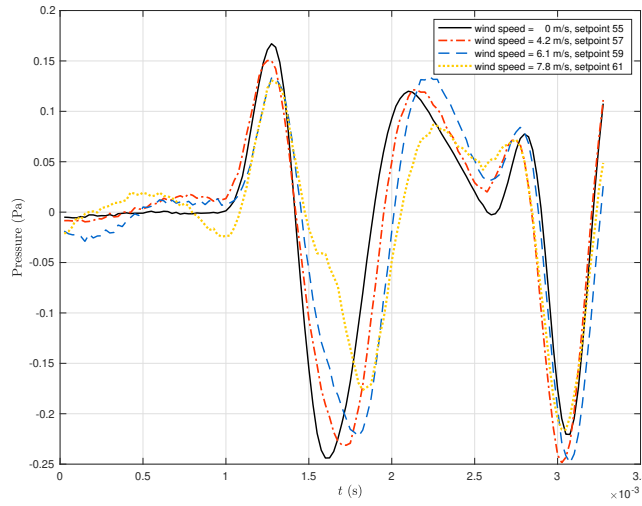


Figure 4-18. Ensemble signal of 1250 Hz with EH = 30 mm, and EL = 590 mm.

trough's impulse response causing about 50% increment on magnitude. After 2.5 milliseconds, the signals completely lose their original wave form, which we believe is the reflected sound waves' interference. We can clearly see the signal's amplitude drops with increasing wind speed from 0 to 7.0 m/s.

With this background noise canceling approach, the test signal's amplitude is obtained for different turbulent flows. Figure 4-19 is a plot of the three frequencies' amplitude versus the estimated wind speed at EH = 0 mm. From the top left to the right bottom, the subplots' titles represent different EL and the colors represent the different frequencies. The overall trend of the four subplots is that the signal's amplitude decreases with increasing wind speed. In the first subplot, the data quality of the 1600 Hz and 2000 Hz signals are unsatisfying because of the unexpected amplitude increase, especially comparing with the 1250 Hz signal. In the other three subplots, the similar patterns are observed with all three frequencies' signals. For the EL = 590 mm case, the maximum amplitude drop happened near the WS = 3 m/s, and the amplitudes for 1250 Hz, 1600 Hz, and 2000 Hz signals reach a flat region after the WS greater than 5 m/s. The amplitude plots of the three frequencies' signals in EL = 740 mm subplot are in a more apparent pattern, with a little bump appeared near WS = 5 m/s. Within the frequency domain, the amplitude of higher frequency's signal is smaller than the lower frequency. On average, the

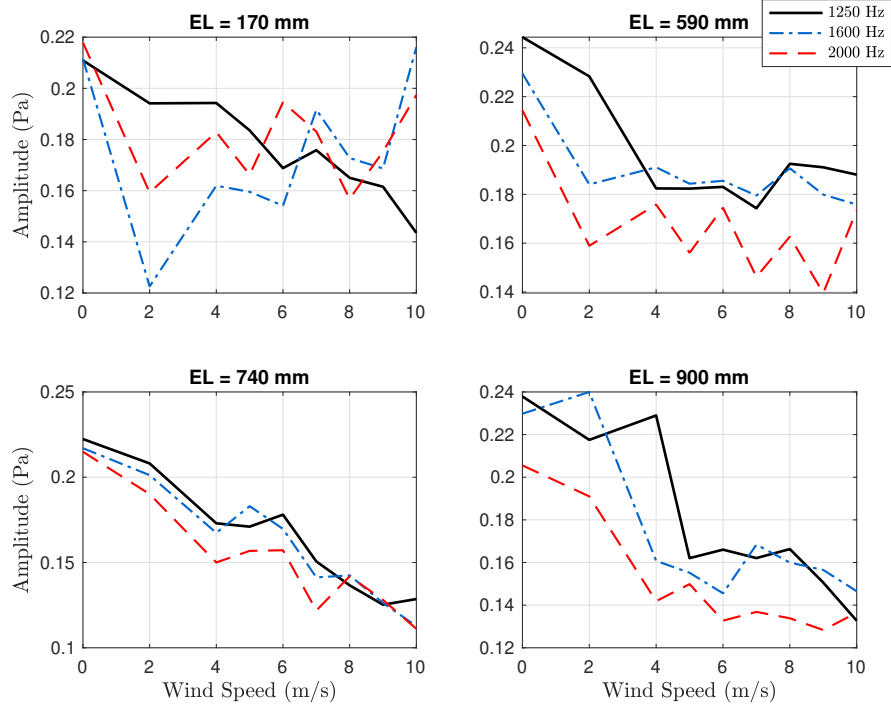


Figure 4-19. Amplitudes of the test signal at EH = 0 mm.

signal's amplitude of the 1600 Hz is 0.15 Pa smaller than the 1250 Hz, while the amplitude of 2000 Hz is 0.1 Pa smaller than 1600 Hz. This amplitude-frequency relation is caused by the atmospheric attenuation, which is predominately dependent on frequency. However, the amplitude decrease caused by increasing turbulent intensity is not frequency independent, because the average amplitude reduction is almost same regardless the frequency variation. To change the turbulent flow's features, the EH increased to 50 mm and the related results are shown in Fig. 4-20. Similar to the results in Fig. 4-19, the amplitude reduction plots in Fig. 4-20 are in the similar patterns for each EL. To investigate the effect of the EH, we use the ratio of the amplitude reduction to the initial amplitude, $\sigma_a = \Delta A_{amp}/A_{ini}$, as the indicator, where ΔA_{amp} is the amplitude drop between WS = 0 and WS = 10, and A_{ini} is the amplitude at WS = 0. From EH = 0 mm case to EH = 50 mm case, the σ_a increases from 0.3195 to 0.5473 with EL = 170 mm.

In the acoustic propagation experiment results, the relation between the amplitude reduction and wind speed is clearly evident, along with the effects of the EH and EL variations. All these parameters (WS, EH, EL) can be considered as sorts of inducement the turbulent flow variations.

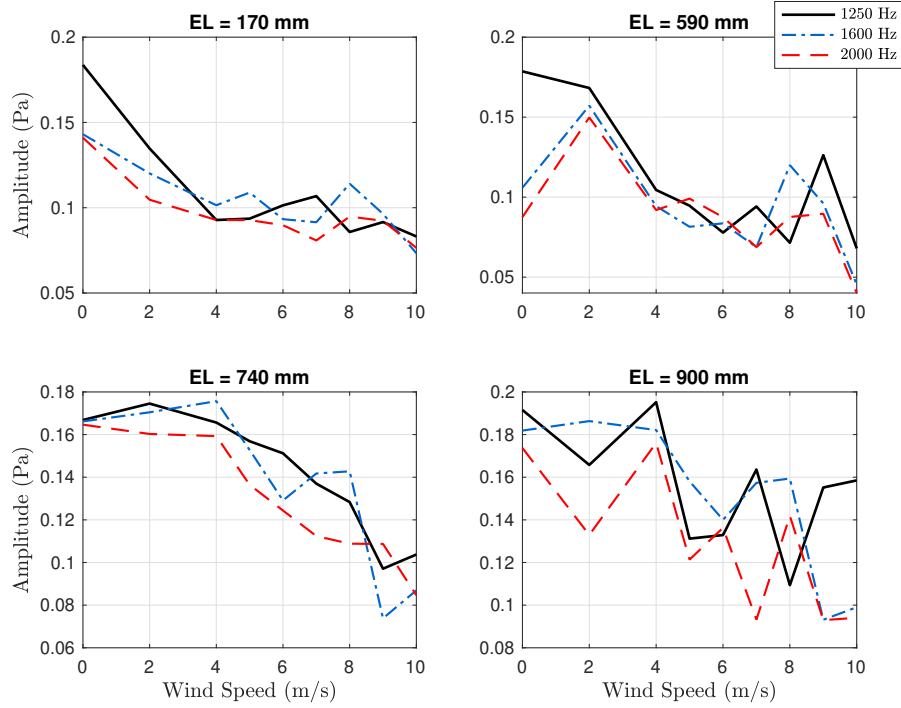


Figure 4-20. Amplitudes of the test signal at EH = 50 mm.

Thus, the turbulent statistics' measurements are necessary for further investigation.

4.4 Field Measurements of Infrasound and Weather Data from Tornadoes

Besides the numerical prediction solver and wind tunnel experimental investigation, our research program involves field tests of tornadoes in the American south east and south to capture the tornado infrasound in the field. The goal of the field measurements is to capture infrasound from tornadoes while simultaneously capturing weather and radar data to provide the numerical solver with realistic source signal and propagation conditions. This way, we completely capture the sound source, weather, radar, and other thermodynamic conditions of actual tornadoes. This portion of the research program is conducted by a joint team at TTU. With two Ka radars and Sticknet weather monitor station, TTU is able to capture the formation and movement of tornadoes.

The infrasound measurement system contains 2 G.R.A.S. 46AZ 1/2" CCP free-field Microphone sets [151] (Fig. 4-21a). These microphones can measure frequencies in the range of 0.5 Hz to 20 kHz with ± 3 dB precision. Our data collection system is shown in Fig. 4-21b. A



(a) *G.R.A.S. low frequency with wind cap*



(b) *DAQ enclosure*

Figure 4-21. Field experiment equipment (Photo courtesy of author).

BNC cable from each microphone connects to a KRYPTONi-1xACC DAQ, which is powered by an AC power battery. The signal is transferred to the DAQ system and recorded by a surface laptop with DEWEsoft X3 software. This whole data collection system is self-contained within a water proof case.

4.5 Summary

In this chapter, the entire experimental procedure is introduced by the logical stages of the experimental campaign. The experimental approaches for three stages are introduced, and the equipment used in the experiment campaign is demonstrated. From the experimental results, the acoustic-turbulent interaction is observed as an attenuation effect, as the amplitude of the recorded acoustic signal decreases with increasing turbulent intensity. On average, near 0.6 Pa amplitude reduction is observed at $EH = 0$ mm with the wind speed increasing from 0 to 10 m/s. For the $EH = 50$ mm cases, the amplitude reduction is approximately 0.8 Pa for the same wind speed increases. For different frequencies, the recorded signals show the similar amplitude reduction pattern with respect to the wind speed at same EH and EL. The obtained experimental data provides the solver development with an reliable data base to modify the scattering model. The data in this chapter is published in the Journal of Structure Engineering [[152](#)].

CHAPTER 5

VALIDATION, SENSITIVITY, NUMERICAL ANALYSIS OF THE BRIDGING MODEL

In this chapter, the author validated the bridging scattering model via UFBLWT experimental data, and investigated the model's sensitivity and applications via numerical approaches. The validation of the model is presented in the Section 5.1. The author numerically propagates an identical source signal through the same boundary layer flows as the UFBLWT tests. By comparing with the experimental recording, the accuracy of the perdition model is obtained. The results of the bridging model are compared with the Ostashev's model. The bridging model is implemented into the Burgers' equation solver (which is introduced in Chapter III) for further propagation tests. In Section 5.2.1, the bridging model's sensitivity is studied with numerical tests in which the model's dependency on the turbulent parameters (TKE and length scale) are addressed. The author also numerically investigates the model's behaviors with the TKE and length scale varying in the designed ranges and compare these behaviors with Ostashev's model. In the last section, Apsley's model [153] is employed to generate a turbulent atmosphere from ground to the altitude of 20 km. Then the author applied the bridging model to this modeled atmosphere to obtain the turbulent absorption coefficient map for the acoustic frequency range from 0.25 to 1024 Hz. The coefficient is presented as contours within the altitude and frequency domain in the Section 5.3. In Section 5.4, the content of this chapter is summarized, and the conclusion is presented.

5.1 Validation by the UFBLWT Experimental Data

As introduced in the Chapter 4, a series of boundary layer propagation experiments are conducted, and the experimental data is collected and published. The purpose of these experiments is to guide the creation and subsequently validate the turbulent attenuation coefficient. The detailed experimental procedure and calibration of the UFBLWT propagation experiments are decribed in details in Zhang et al. [152]. The experimental data is publicly available through the DesignSafe cyberinfrastructure [149]. In this section, the author focuses on the data analysis and the comparison between the prediction and experiments. The validation of turbulent attenuation coefficient are presented through these comparisons.

5.1.1 UFBLWT Experiments Setup

Recall from the previous chapter, the three objectives of the experiment are critical for our model validation. The first involves the careful construction of the source acoustic signal within the tunnel. The second involves the measurements and characterization of the turbulent statistics within the tunnel. The third involves measuring the acoustic signal altered by the turbulence.

The first objective that involves the source signal, is created by a speaker. The anechoic-chamber measured source signal is presented here in Fig. 5-1 with the original signal generated by MATALB. The Matlab-generated source signal of 800 Hz is shown as the blue-dash

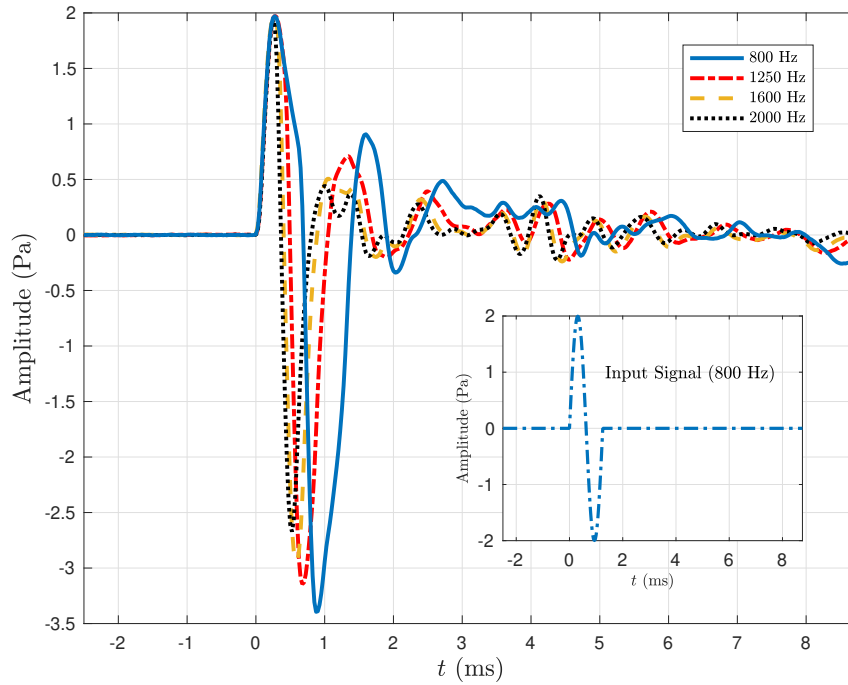


Figure 5-1. Output single cycle signals at 2 m from speaker.

line in the figure inset. We recorded 800 Hz, 1250 Hz, 1600 Hz, and 2000 Hz pulses at a 2 m distance from the speaker. For the first crests of each source signal, the over-pressure amplitudes are 2 Pa. By comparing with the source signal trough at -2 Pa, the impulse responses are observed at the troughs for all four signals in the anechoic chamber, since the amplitudes of the troughs are -3.393 Pa, -3.136 Pa, -2.857, and -2.657 Pa for 800 Hz, 1250 Hz, 1600 Hz, and 2000 Hz, respectively [152]. The 800 Hz pulse had the most intense response since its trough had the

highest magnitude of 3.393 Pa. The anechoic chamber measured signal is the actual source signal in the wind tunnel test, thus the author uses these measured signal as the source signal for the numerical propagation solver.

The second objective is accomplished via measuring turbulent statistics via Cobra probes within the tunnel. These probes are mounted on an automated mechatronic gantry system that moves in three dimensions. Via this approach, both mean flow and turbulent statistics are measured through the turbulent boundary layer. Probes are moved downstream and in the cross-stream direction at multiple locations. The wind tunnel has the ability to control boundary layer roughness via individually controllable roughness elements on the floor. In this way, our results encompass a wide range of realistic atmospheric conditions with varying turbulent statistics, ground roughness, and mean flow velocities. The probe-measured wind velocity, TKE, and length scale, along with the humidity, and temperature, are imported into the propagation solver as the path-dependent parameters. These detailed temperature, humidity, static pressure, and turbulence measurements are available via DesignSafe [149].

The third objective involving measuring the turbulent-distorted acoustic signal, is obtained by a G.R.A.S. [151] microphone system. The detailed pressure-time history of these microphone recordings are presented in the following subsection. The author compares the solver's predictions to the wind tunnel recordings to evaluate the solver's accuracy.

5.1.2 Predictions Compared to UFBLWT Measurements

In this subsection, the author compares the bridging-model embedded solver's predictions to the experimental data. All the wind tunnel measurements including flow velocities, static pressure, humidity, temperature, TKE, and length scales are input directly into the propagation solver. Then the experimental source signal in Fig. 5-1 is sent into the solver to propagate through the same medium and distance as the wind tunnel test. Finally, the solver predicted signal at the receiver is compared to the experimental recording.

Reflections of the source signal on the tunnel walls and the background tunnel noise reduce the quality of our measurements. To reduce these effects, the author implements a ensemble

averaging technique and a linear reflection wave prediction to reduce and remove these disturbances, respectively. By taking the ensemble average of the 36 repeated single cycles for each frequency, the broadband turbulent noise can be efficiently removed, and the signal-to-noise ratio is improved to 2.8 and higher for acoustic measurements. To isolate the portion of the received signal that resulted from reflection from the tunnel walls, the single-cycle signal is also propagated by a linear wave propagation solver with the walls' reflections. There are minimal temperature gradients in the tunnel and the velocity gradient is small, which means the refraction in wind tunnel is negligible. For the purpose of predicting reflection, the ray path is assumed to be a straight line, and the reflections are considered as sound hard reflections. The reflection surfaces are the ceiling, two sidewalls, and the ground. The ceiling and side walls are made of painted plywood, and the ground is made of phenolic plywood. For the ground reflection, the angle of incidence is between 85.3 to 89.1 degrees (varying due to increasing EL), which causes a grazing effect [154]. The ground reflection is not included due to the roughness elements, which scatter and destroy the reflected wave.

For the validation purpose, 24 cases from the wind tunnel experiments are selected for the numerical solver. The case number, EH, EL, TKE, and L_v are listed in the Table. 5-1. Figure 5-2 shows four example comparisons between the numerical predictions and the recordings from UFBLWT. The black lines are the experimental measurements, the dash-dot red lines are the predictions from the nonlinear propagation solver, the dot blue lines are the results of the linear wave prediction, and the bars represent the uncertainty of the experiment. To emphasize the time of arrival of reflected waves, the vertical dash blue lines representing the arrival time are placed in the figures. Tests 1, 2, and 3 are measured at the same EL of 170 mm with the mean wind speed of 5.16 m/s, 6.86 m/s, and 8.64 m/s, while Test 10 is measured at the EL of 900 mm with the wind speed of 5.16 m/s. The EHs of these four cases are set at 30 mm. More cases are accessible via the DesignSafe data depot [149]. The linear wave prediction successfully captures the reflections since the waveform of the prediction matches the experimental data. From the experimental results in Test 10, we can clearly see two reflections with the first reflected crest at +1.2 s of 0.36

Table 5-1. Validation Cases from UFBLWT

Case Number	EH (mm)	EL (mm)	TKE (m^2/s^2)	L_v (m)
1	0	170	0.285497439	1.89229835
2	0	590	0.489045006	2.55338616
3	0	740	0.746791184	3.17293199
4	0	900	0.245965851	1.99618983
5	0	170	0.473571295	2.70437004
6	0	590	0.673486221	3.38440037
7	0	740	0.232772216	2.03943488
8	0	900	0.39870511	2.76364275
9	0	170	0.558109027	3.41604406
10	0	590	0.18105005	2.06054768
11	0	740	0.316720206	2.80264579
12	0	900	0.466614857	3.47699021
13	30	170	0.353873967	1.78445229
14	30	590	0.63734585	2.40364506
15	30	740	0.956740539	2.98005391
16	30	900	0.270380982	2.00620386
17	30	170	0.508913882	2.70243448
18	30	590	0.676676571	3.40066319
19	30	740	0.233836928	2.0537407
20	30	900	0.413122501	2.77636998
21	30	170	0.600274472	3.43597764
22	30	590	0.190015219	2.07592138
23	30	740	0.333646917	2.81281356
24	30	900	0.474984052	3.48962781

Pa and the second reflected crest at +2.4 s of 0.4 Pa.

Predictions shown in Fig 5-2 are the results from the propagation solver without considering reflections. The turbulent attenuation effect is captured by the solver as the predicted amplitudes of the first crest in Test 1, 2, and 3 are 0.18 Pa, 0.11 Pa, and 0.09 Pa, which are all located in the uncertainty range of the experimental results. A 0.09 Pa amplitude decrease is observed with increasing mean TKE from $0.27 \text{ m}^2/\text{s}^2$ to $0.75 \text{ m}^2/\text{s}^2$. The turbulent length scale of Test 1 and Test 10 are 1.89 m and 2.06 m, respectively, while the TKE of Test 1 and Test 10 are $0.27 \text{ m}^2/\text{s}^2$ and $0.18 \text{ m}^2/\text{s}^2$. The different reflection patterns between Test 10 and the other tests shown in Fig. 5-2 are caused by the different ELs, while the EL is 900 mm for the Test 10 and 170 mm for the Test 1, 2, and 3. The decrease in TKE and increase in length scale cause a 0.005 Pa amplitude increase from Test 1 to Test 10.

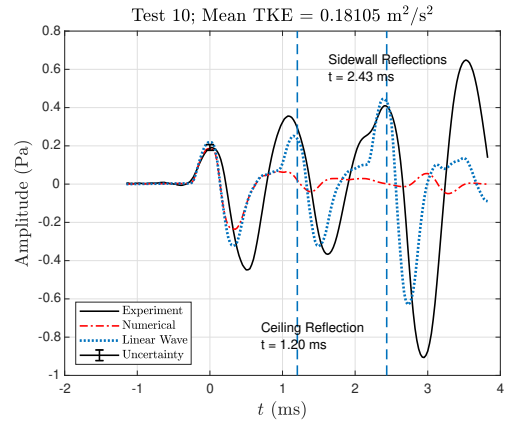
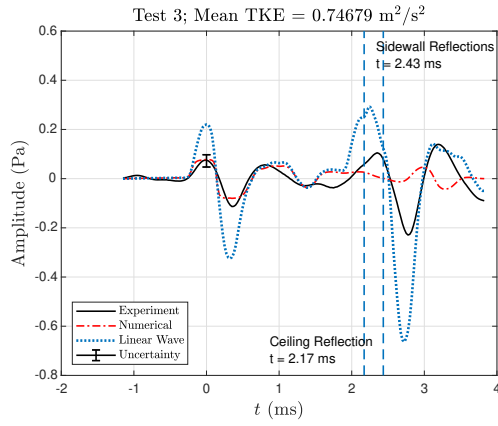
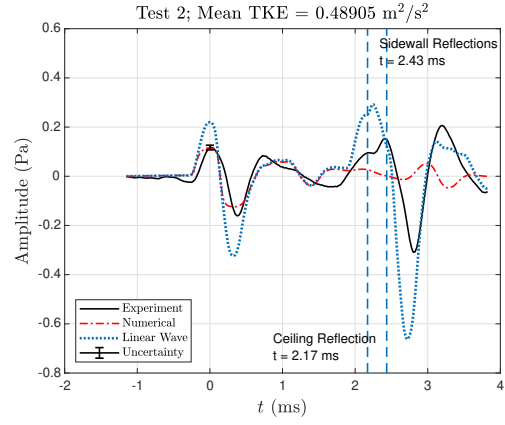
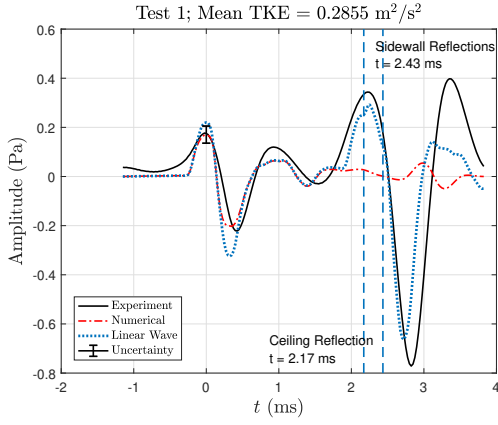


Figure 5-2. The comparison between the experimental results and numerical predictions with reflection isolated.

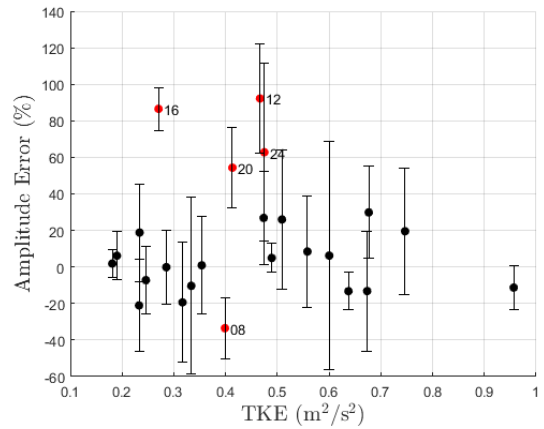
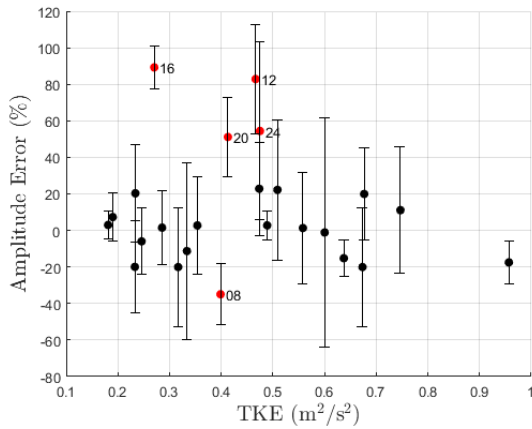


Figure 5-3. The error comparison between the bridging model (top) and Ostashev's model (bottom).

Errors of the 24 predictions relative to experiments are shown in Fig. 5-3. The dots represent the percentage error between the prediction and experiment, and the outliers (prediction not located within the uncertainty band) are colored as red dots and labeled by their test number. The average error of Oshtashev's model is 24.32%, and the average error of the Bridging model is 22.45 %. By removing the outliers from the results, the error of Ostashev's model decreases to 12.67%, while the bridging model's error is 11.9%. The average error of the model is 11.9%, which is approximately a 1% improvement relative to Ostashev's model. However, this prediction improvement is over a distance of 22 m, while propagation in an atmosphere would be approximately 100 km. Turbulent attenuation is observed in the experimental results and is captured by the propagation solver.

5.2 Sensitivity Analysis

A numerical sensitivity analysis is conducted to investigate the new model's (Eqns. 2-79 through 2-80) characteristics and performance for predicting turbulent scattering. For each test, a 1% perturbation is applied to each parameter while all other parameters remain constant. The resulting variation caused by the 1% perturbation is investigated to ascertain each parameter's influence in the propagation process. In this section, the sensitivity tests are divided into two parts: the model sensitivity and the solver sensitivity. By analyzing the absorption coefficient (converted from the cross-section σ_{tot}), the sensitivity of the parameters in the scattering model is obtained. By obtaining the sound pressure level (SPL) variations with each corresponding parameters' perturbation, the most and least sensitive parameters can be identified for the propagation solver.

5.2.1 Parameter Sensitivity in the Scattering Model

The turbulent field is constructed via the von Kármán spectrum (Eqn. 2-67). The total cross-section is calculated by Eqn. 2-68 from Ostashev's model and Eqn. 2-80 from the bridging model by integrating the equations over the entire scattering angle. For both models, the limited-length $k - \varepsilon$ model by Apsley and Castro [153] is employed to reconstruct the atmospheric turbulence for this test. An acoustic ray is constructed as a straight-line horizontal path with an altitude of 100 m to grantee the constant value of the TKE and length scale.

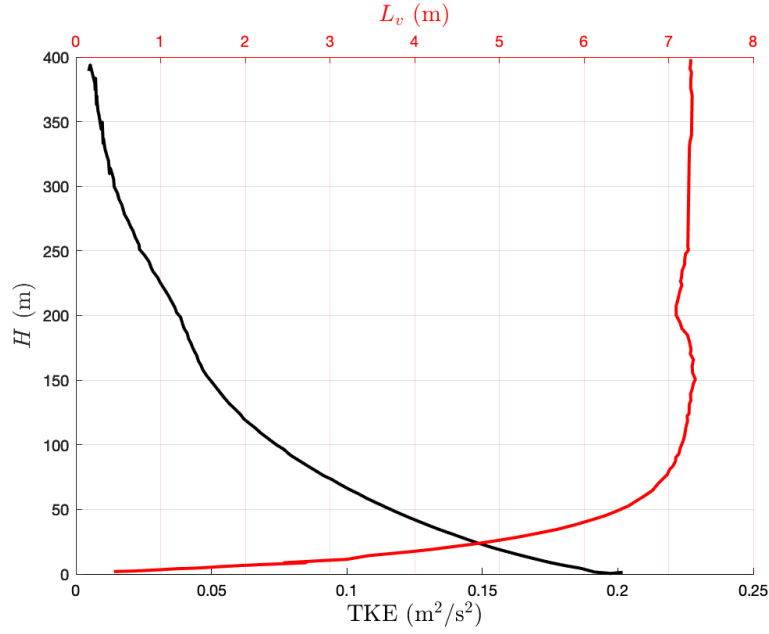


Figure 5-4. Turbulent kinetic energy and length scale predicted by Apsley's model.

Fig. 5-4 is the TKE and length scale profiles from Apsley's model Apsley and Castro [153]. The TKE at 100 m altitude is $0.07 \text{ m}^2/\text{s}^2$, and the length scale is 7.17 m. Then the scattering attenuation coefficients along the ray path are obtained by implementing the TKE and length scale to the scattering model. Fig. 5-5 shows the results of the sensitivity analysis of the scattering models.

The y-axis on the left represents the normalized sensitivity (variation over original value) of the parameters. The total cross-section is converted to the classic absorption coefficient with the unit of dB/km, which is represented by the right y-axis. The solid line is the coefficient obtained from the bridging model, while the dash line is the coefficient calculated by Ostashev's model. Here, α_t represents the turbulent absorption coefficient. Both models agree with each other from 0 to 200 Hz, while the gradient of increasing absorption coefficient in the bridging model decreases when the frequency is higher than 200 Hz. Sensitivity is normalized with its corresponding non-perturbation value. The TKE is represented by the square of the fluctuating velocity σ_v^2 . For Ostashev's model, the perturbation introduced by TKE is steady at 2.012%, which is reasonable considering the TKE in Eqn. 2-67 can be extracted via integration in Eqn. 2-68. The TKE's

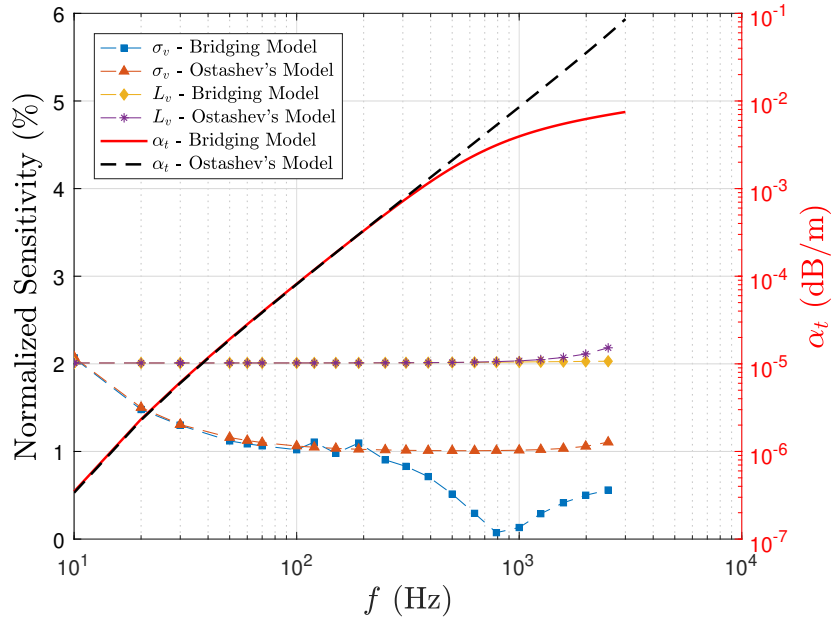


Figure 5-5. The sensitivity of the scattering models.

sensitivity in the bridging model shows a similar trend below the frequency of 1 kHz. When the frequency is higher than 1 kHz, the TKE in the bridging model has a stronger influence with 2.025% coefficient variation. The difference between those two models on the length scale's sensitivity starts from the low-frequency region (around 1 Hz) and increases with frequency. The minimum normalized sensitivity of the L_v is 1.003% at 1000 Hz in Ostashev's model, while the minimum sensitivity of L_v in the bridging model reaches as low as 0.073% at 800 Hz.

From the comparison between those two models, the overall sensitivity of those parameters are similar in those two models, while the bridging model shows 10% stronger length-scale sensitivity than Ostashev's model at 2048 Hz. Meanwhile, the σ_v sensitivity of the bridging model is 56% less than Ostashev's model at 2048 Hz.

5.2.2 Effects of Parameters in Numerical Propagation Solver

A numerical sensitivity analysis is also applied on the propagation solver. A shock wave and a synthetic tornadic infrasound signal are employed for this analysis. The turbulent atmospheric conditions for the propagation sensitivity study are identical to the modeled turbulence in the previous subsection. All the propagation cases are set as plane wave

propagation. The 1% perturbation is applied to six different parameters in the propagation solver.

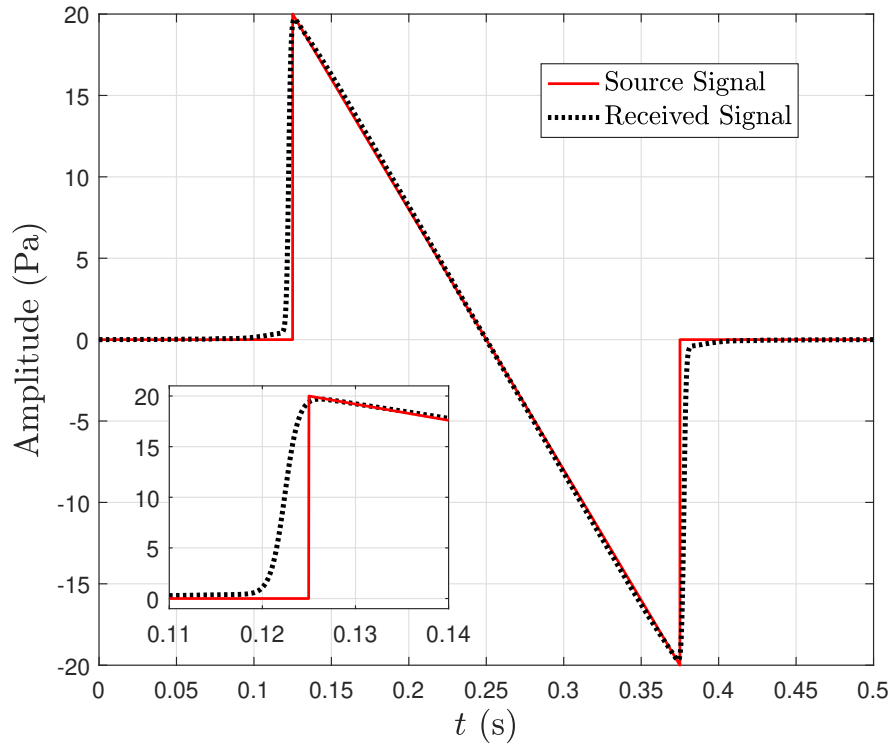


Figure 5-6. Predicted received waveform relative to N wave source.

For the shock wave propagation case, a left-running N-wave is constructed with an amplitude of 20 Pa and time-span of 0.30 s with sampling frequency of 16,384 Hz. Because a 10 sample-point wide Lanczos resampling is applied to the solver to remove the Gibbs' phenomenon at the end of the time marching, frequencies higher than 819 Hz are not examined. For this case, the total propagation distance is 1.0 km, the propagation altitude is 100 m, the humidity is 50 %, and the temperature is 20 °C. The predictions of the pressure time history are shown in Fig. 5-6, where the solid line signal is the source signal, and the dashed line signal is the received signal. The sensitivity analysis for the shock propagation case is shown as Fig. 5-7.

The six parameters tested are the amplitude of the shock (p_{mag}), the propagation distance (R), the atmospheric nonlinear coefficient (β), the atmospheric attenuation coefficient (α), the turbulent length scale (L_v), and the turbulent velocity variance (σ_v). The solid line represents the source signal's spectrum, while the dotted line is the spectrum of the received signal at the

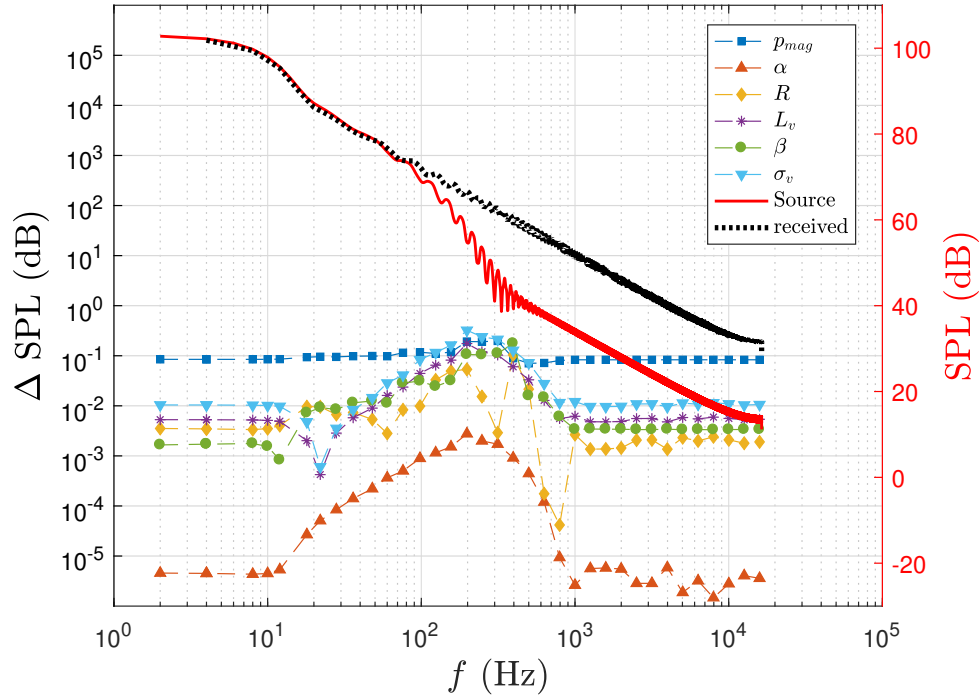


Figure 5-7. Shock wave propagation results and sensitivity analysis.

observer. A significant broadband reduction is observed with the frequency higher than 80 Hz. The parameters are most sensitive in the region between 10 Hz to 1000 Hz. Frequency-dependent absorption is also observed in this region. We observe that the least influenced parameter among those examined is the atmospheric attenuation, whose highest sensitivity is about 3×10^{-3} dB at 20 Hz. The nonlinearity coefficient's sensitivity reaches its highest value near 30 Hz with a 0.1 dB influence on the signal. The velocity variance σ_v and the length scale L_v show similar trends over the entire spectrum. σ_v and L_v initially decrease from 10^{-2} dB and 7×10^{-3} dB at 2 Hz to 3×10^{-4} dB and 6×10^{-4} at 20 Hz, respectively. Then the σ_v and L_v 's hump-like sensitivity increases are observed from 20 Hz to 1024 Hz with a similar profile as α . The difference between the sensitivity of σ_v and L_v almost stay at the same value over the entire frequency domain. The most sensitive parameter is the amplitude of the signal p_{mag} . In the entire frequency range, the sensitivity of p_{mag} is 0.1 dB except for the region near 200 Hz, where a slight increase to 0.2 dB is observed. The propagation distance R is the only parameter that does not have the hump-like sensitivity profile. The amplitude of fluctuation of R 's sensitivity increases with increasing

frequency.

All the parameters show relatively higher sensitivity near the frequency at 200 Hz for the shock propagation case. The most sensitive parameter is the amplitude of the shock wave, while the least sensitive parameter is the atmospheric attenuation. The turbulent attenuation model's two critical parameters, σ_v and L_v , have the same order of magnitude sensitivity. The average value of σ_v and L_v 's sensitivity is higher than R , β , and α , which imply the importance of the turbulent effects during the shock propagation.

We now turn our attention to the sensitivity of broadband tornadic infrasound propagation. A tornadic broadband signal is reconstructed with the model of Frazier et al. [55] as

$$S(\omega) = A_f \omega^{-7/3} + \frac{A_s \omega_n^2 \omega^2}{\omega^4 + 4\xi \omega_n^2 \omega^2 + \omega_n^4} g_a(\omega) + A_n. \quad (5-1)$$

The first term represents the atmospheric background noise, the second is the characteristic tornadic infrasound, and the last is the spectrum magnitude baseline. Here, we isolate the tornadic signal by removing the first term since the atmospheric background noise is not the primary focus of the study. To emphasize the characteristics of the tornadic infrasound, the parameters are chosen here are: $A_s = 1.051$, $\omega_n = 9.3$, $\xi = 0.057$, and $A_n = 5.11 \times 10^{-4}$. The spectrum of the reconstructed signal is shown in Fig. 5-8.

The reconstructed signal is constructed by linear superposition of the tonal noise of all frequencies with energy provided by the modeled red spectrum in Fig. 5-8. The black spectrum is obtained from the reconstructed pressure time history of the tornadic infrasound signal. The reconstructed signal matches with the modeled spectrum, and the average error is 1.3 dB per Hz.

The modeled tornadic infrasound signal is propagated over 1 km with identical altitude, humidity, temperature, and turbulent statistics to the shock propagation test. The prediction of the pressure time history of this tornadic infrasound case is shown in Fig. 5-9.

The upper solid line is the pressure time history of the source signal. The dashed line represents the received signal. In Fig. 5-9, we observe that the maximum amplitude drop is about 3.5 Pa, which is mainly caused by the high-frequency energy decay. This frequency dependent

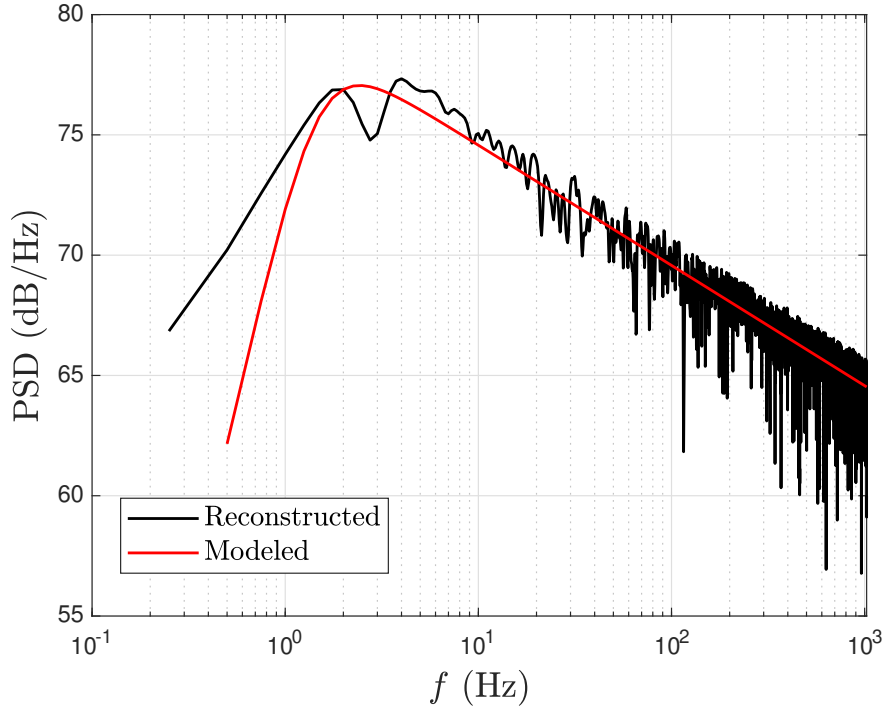


Figure 5-8. Reconstructed tornadic infrasound spectrum via Frazier et al. [55]'s model.

energy decay is easily observed in Fig. 5-10, where the solid line represents the source spectrum and the dashed line represents the received spectrum.

The largest SPL drop in the spectrum occurs in the range of 30 Hz to 1000 Hz. Unlike the shock wave propagation case, the sensitivity of amplitude p_{mag} remains at a constant level of 0.1 dB for all frequencies. The sensitivity of propagation distance R follows almost the same trend as p_{mag} with the value fixed at 10^{-2} from 0.25 Hz to 100 Hz. When the frequency is higher than 100 Hz, the sensitivity of R surges from 10^{-2} at 100 Hz to 10^{-1} at 1000 Hz. The nonlinear coefficient β is the least sensitive parameter when the frequency is higher than 30 Hz, which is reasonable since the overall SPL of the tornadic infrasound is 99.46 dB, and there is no nonlinear component in the source signal. The sensitivities of atmospheric attenuation α and length scale L_v are the same order of magnitude for the frequency range from 20 Hz to 300 Hz, while fluctuations of α and L_v are observed between 10^{-6} dB and 10^{-4} dB from 0.25 Hz to 20 Hz. From 20 Hz to 1000 Hz, the sensitivities of α and L_v increase on the order of 10^{-4} dB to 10^{-2} dB. The sensitivity of ω_v^2 follows a similar trend as α and L_v , but with higher sensitivity, which increases from 10^{-4} dB

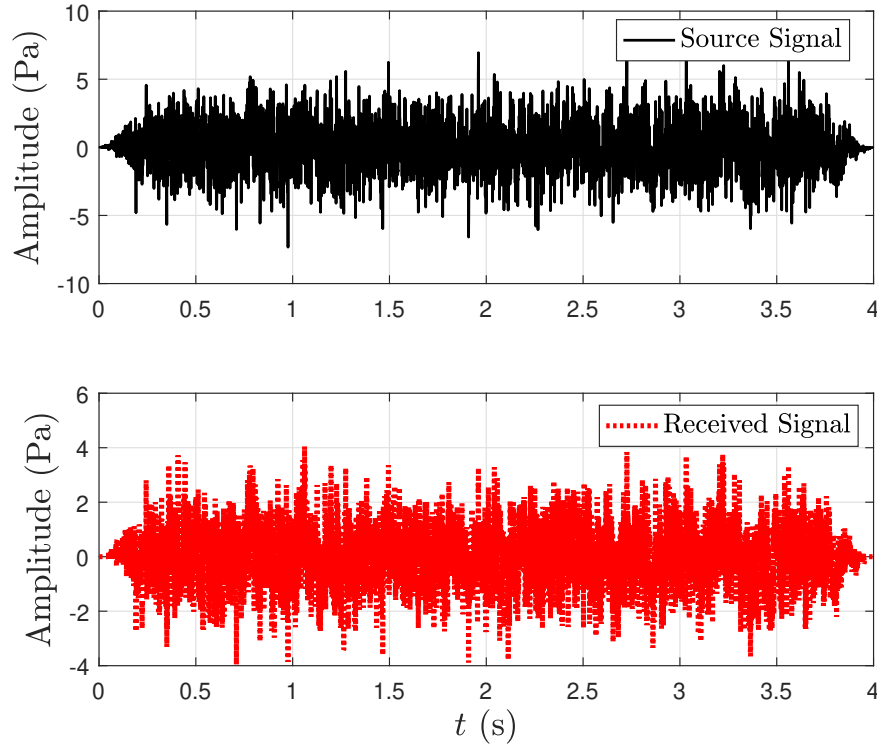


Figure 5-9. Numerical Prediction of the Tornadoic Infrasound Propagation.

at 10 Hz to 0.12 dB at 1000 Hz.

From those two sensitivity analyses, σ_v and L_v are as significant as other propagation parameters. From the macroscopic perspective, parameters are more sensitive with higher frequency in this tornadoic infrasound case.

5.3 Numerical Model Analysis and Parametric Study of the Propagation Solver

The author examines propagation trends with the new bridging model to understand its behavior within more realistic scenarios. In particular, the TKE and L_v are examined since they are the key factor of the bridging model. For this subsection, the absorption coefficient α_t quantifies the effects of TKE and L_v . We examine the source that corresponds to the synthetic tornadoic signal propagation case.

Figure 5-11 shows the distribution of α_t with frequency range of 0.25 Hz to 1024 Hz and TKE range from 0.1 to 10 m^2/s^2 . In Fig. 5-11, the x-axis is the acoustic frequency in Hz, the y-axis is the TKE in m^2/s^2 , and the colors represent the value of the turbulent absorption

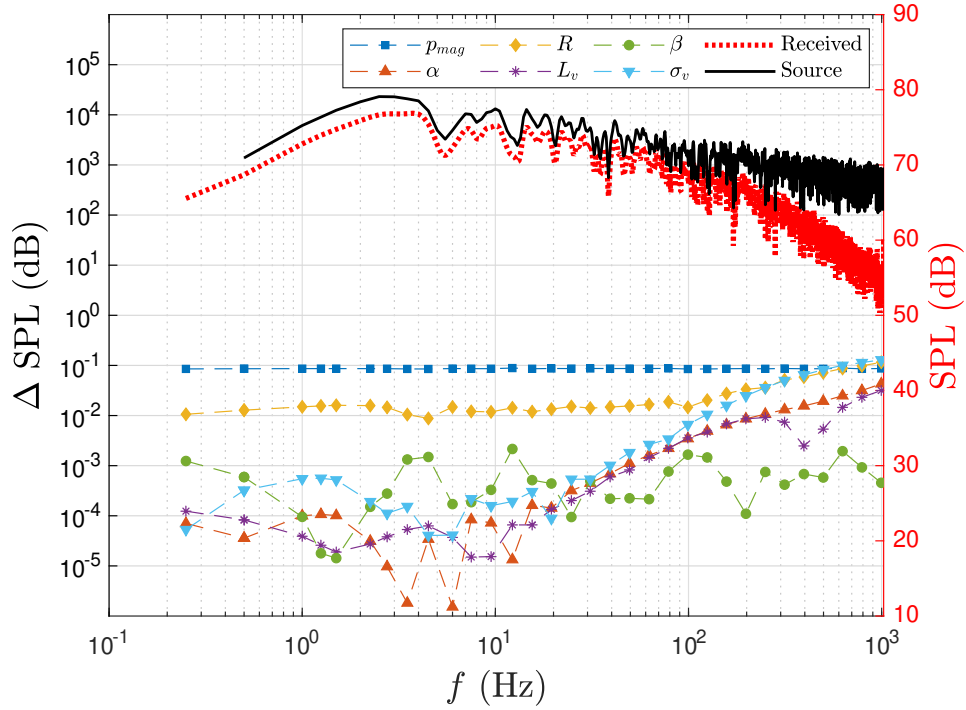


Figure 5-10. Sensitivity analysis of the tornadic infrasound case.

coefficient. The integral length scale L_v for this prediction is fixed at 1.2 m. The coefficient contours are in log scale ranging from 10^{-15} to 1 dB/km. The overall trend of α_t is increasing with increasing TKE, as expected. Turbulent absorption shows a linear increase with frequency, which is similar to the trend involving the atmospheric absorption coefficient Sutherland and Bass [68]. In the low frequency region, $f < 20$ Hz, the maximum α_t is below 10^{-4} dB/m, even with the maximum TKE at $10 \text{ m}^2/\text{s}^2$. For a 20 Hz acoustic signal, the atmospheric absorption coefficient is 2×10^{-5} dB/m. Even for the minimum TKE at $0.1 \text{ m}^2/\text{s}^2$, the turbulent absorption coefficient is approximately 6^{-6} dB/m. Based on this prediction, the turbulent absorption can strengthen the overall acoustic attenuation by a factor ranging from 30% to 500% during propagation in the turbulent atmosphere.

The distribution of the turbulent absorption coefficient α_t in the frequency- L_v domain is presented in Fig. 5-12. Unlike Fig. 5-11, the x -axis is linear to illustrate a clearer insight into the dependency between the L_v and α_t . The TKE for this prediction is set at $0.2 \text{ m}^2/\text{s}^2$. The L_v 's range is from 0.5 to 500 meters, while the frequency range is kept the same as in Fig. 5-11.

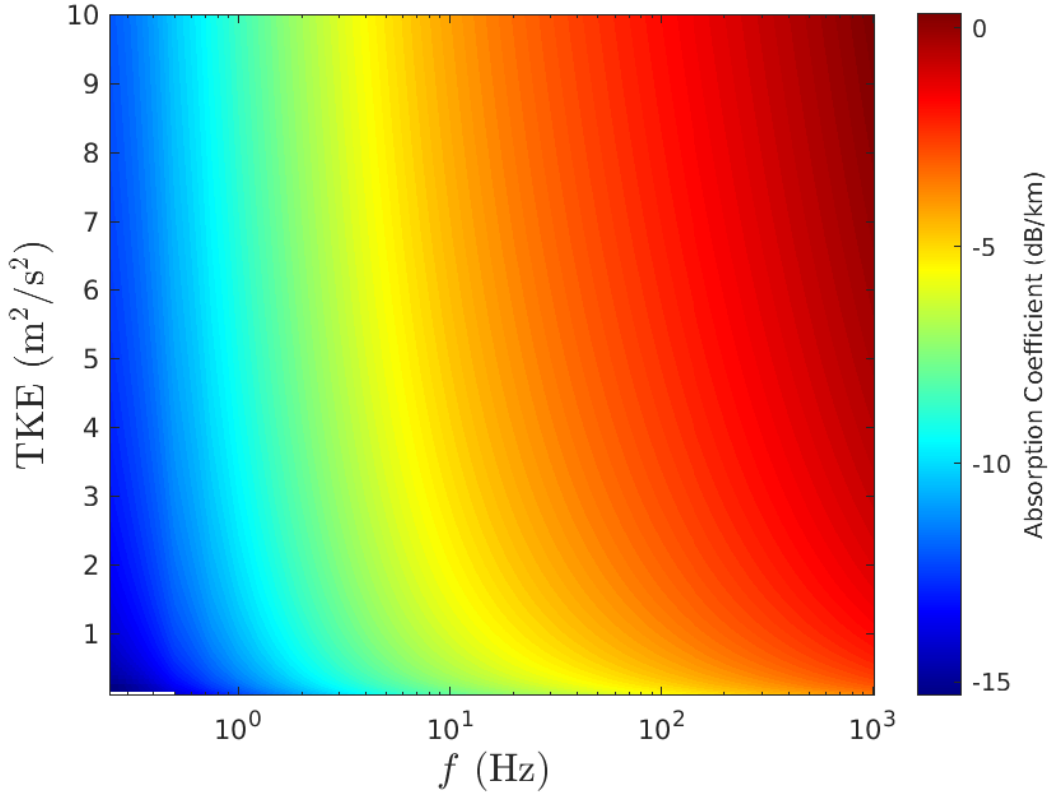


Figure 5-11. Absorption coefficient with respect to TKE and acoustic frequency.

Contour lines are solid. By using the linear x -axis, the α_t 's profile for high frequency shows a hill-like shape with increasing L_v . The L_v of the turning point of these hill-like profiles decreases with increasing frequency. This behavior is caused by the integration of Eqn. 2-80, where L_v can alter the integrating area in wavenumber space. Therefore, the correlation between L_v and acoustic frequency contributes to the curve in Fig. 5-12. Similar behavior is also observed in the predictions of Ostashev's model, and the detailed difference between these two models are shown in Fig. 5-13. An α_t difference contour map is presented in Fig. 5-13 by subtracting the turbulent absorption coefficients from Ostashev's model with the bridging model. Here, the turbulent statistics are identical to those presented in Fig. 5-12.

In Fig. 5-13, the difference of α_t between α_t from the bridging model and Ostashev's model is normalized with the turbulent absorption coefficient from Ostashev's model. At $f > 100$ Hz, the difference between these two models are negligible. At infrasonic frequencies, the difference

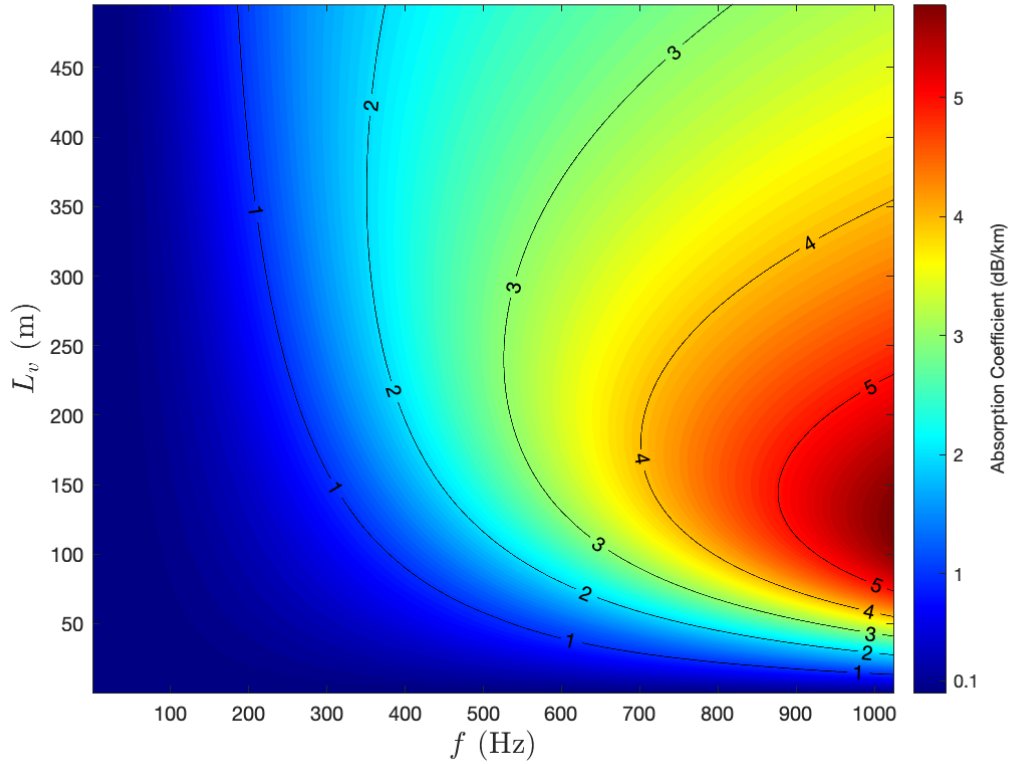


Figure 5-12. Absorption coefficient as a function of turbulent length scale and frequency.

approaches 3% to 4%. The maximum difference appears from f at 10 Hz and L_v at 0.5 m to $f = 0.25$ Hz and L_v at 100 m. This indicates that the effect of the bridging model is more apparent at low frequencies, and that the new model is not required for higher frequency signals.

Figures 5-14a and 5-14b show the results of the OASPL difference with and without turbulence. The tornadic signal shown in Fig. 5-9 is employed as the source signal. The Δ OASPL is the difference between the OASPL of the propagation within a turbulent field and without, respectively. For the first test, the TKE of the turbulent model is fixed at $0.0285 \text{ m}^2/\text{s}^2$, while the L_v varies from 2.5 to 250 m. A $\pm 5\%$ perturbation is applied to evaluate the sensitivity of the model. As shown in Fig. 5-14a, the effects of L_v on the Δ OASPL are linear, while the effects of the perturbation also follows a linear variation.

Finally, we examine an atmosphere with varying TKE and L_v . Variation is governed by the model of Apsley and Castro [153] in an altitude range of 0 to 20 km. Fig. 5-15 shows on

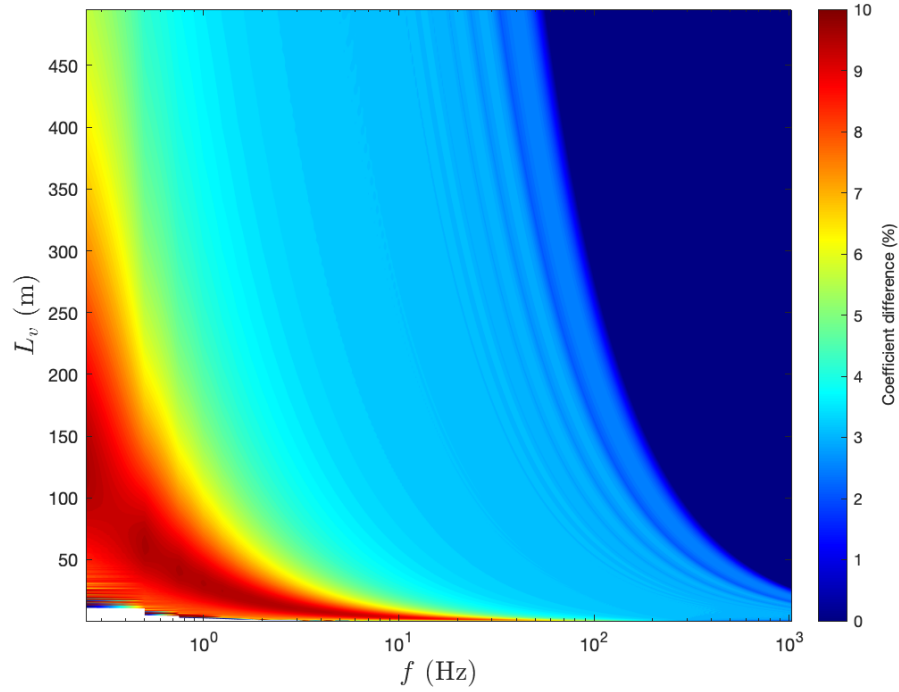
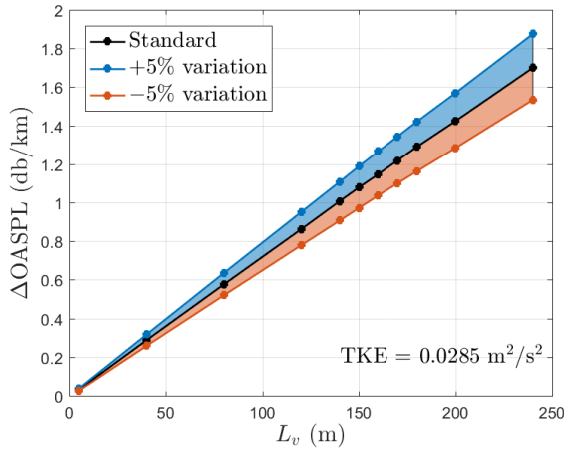
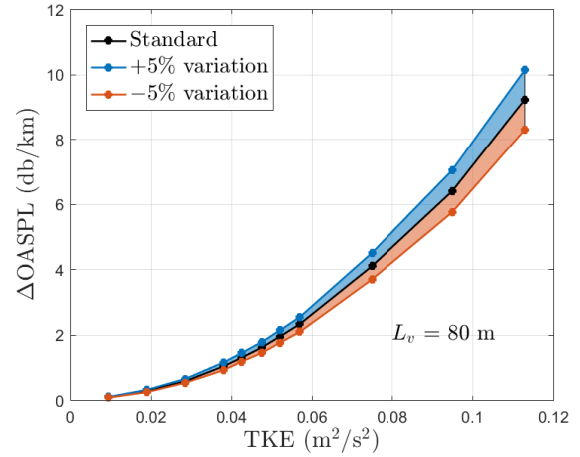


Figure 5-13. Coefficient difference between the bridging model and Ostashev's model.



(a)



(b)

Figure 5-14. Δ OASPL of the bridging model with varying L_v and TKE.

representative example of the turbulent attenuation distribution from 0 to 20 km. The dark blue line represents the maximum absorption, and also represents the height of maximum absorption for each frequency. The dependency of the absorption coefficient on frequency is clearly observed

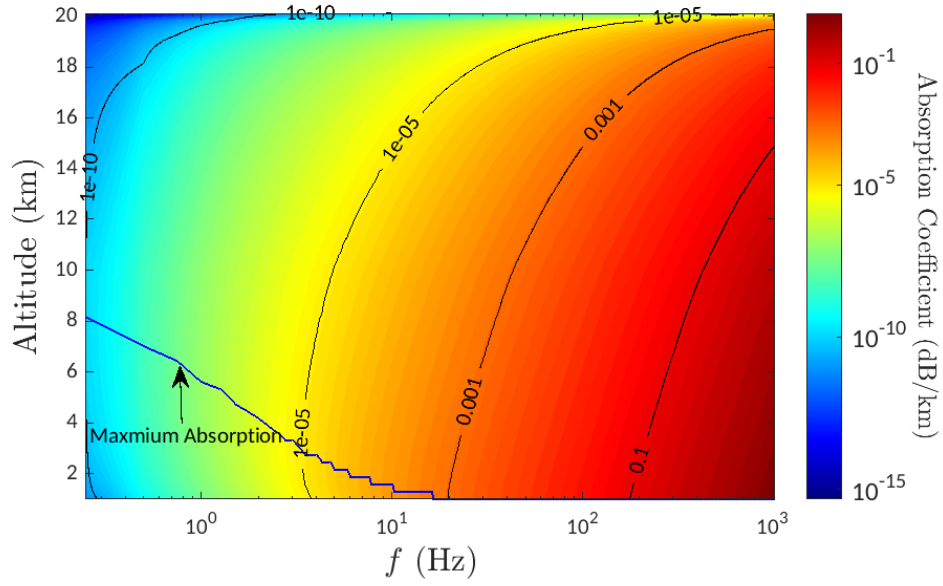


Figure 5-15. Absorption coefficient distribution in frequency and altitude.

as the overall trend of the coefficient increases from 10^{-10} dB/km to 10^{-1} dB/km with increasing frequency from 0.2 to 1000 Hz at 2 km high. For f higher than 20 Hz, the absorption decreases with increasing altitude monotonically. The connection between maximum absorption and altitude is illustrated by the line. For infrasound frequencies (less than 20 Hz), the maximum turbulent absorption altitude increases with decreasing frequency, and this maximum occurs near 8 km at 0.25 Hz. For $f > 20$ Hz, α_t decreases with increasing altitude monotonically. This is due to a combined effect of increasing L_v and decreasing TKE as altitude increases.

5.4 Summary and Conclusion

In this Chapter, the bridging model of acoustic-turbulent interaction for long-range propagation is experimentally validated and numerically investigated. The bridging model is implemented into a generalized Burgers' equation solver for long-range propagation. The solver-predicted signals at the receiver are compared to the UBFLWT experimental recordings. Sensitivity analyses are conducted for both the model and solver. The TKE shows more influence than the length scale in both Ostashev's model and the bridging model. The overall sensitivity of the turbulent length scale in the bridging model is less than in Ostashev's models. The sensitivity of TKE and length scale are also compared with other propagation parameters, including

nonlinear coefficient β , atmospheric absorption α , signal amplitude p_{mag} , and propagation distance R . The TKE and length scale show stronger influence than atmospheric absorption and even reach the maximum sensitivity with the same magnitude as the p_{mag} at 1000 Hz for the tornadic infrasound case.

A series of wind tunnel propagation experiments are conducted in the NSF UFBLWT to validate the newly developed bridging model. The experiments successfully captured the turbulent attenuation. The peak amplitude of the received signal varies from 0.22 Pa to 0.084 Pa, with the mean wind tunnel speed from 0 to 8.56 m/s. These results showed that both Ostashev's and the new model make excellent predictions, and that there is a slight improvement in prediction accuracy with the new model by approximately 1 to 2%. This error is dimensional over the length of the tunnel, and would be amplified over longer distances.

A series of numerical studies are conducted to investigate the new model's characteristics and its influence on the propagation of signals. The TKE and L_v 's effects on predictions are presented, where the TKE primarily effects absorption, and L_v alters α_t . The OASPL of the received tornadic signal is used to analyze the overall influence of the bridging model. Both TKE and L_v contribute to larger decrease of OASPL. By implementing a realistic turbulent atmospheric model with the bridging model, a maximum absorption line is observed within the α_t contour. The content of this chapter is submitted to the Journal of Acoustic Society of America [?].

CHAPTER 6

CONCLUSION AND FUTURE WORK

In this dissertation, infrasound propagation in the atmosphere is investigated by theoretical studies, numerical models, and experimental tests. A new bridging model for acoustic-turbulent interaction is developed. Ostashev's model [11] is modified with the classic acoustic ray theory to account for turbulent refraction effects. To predict the propagation of waves over long distances, this bridging model is implemented into a validated Burgers' equation solver to account for the turbulent effects in the atmosphere. Together, the combined numerical approach represents a fast-responding early-warning tornado prediction system by coupling it with the ray tracing method. It can be incorporated into the NOAA prediction network for early warning of tornadoes. A series of unique boundary layer experiments are conducted in the NSF funded UFBLWT to evaluate the bridging model's accuracy and behavior. A specially-designed microphone-speaker system and three-cobra-probe system successfully collected acoustic and turbulent statistics during the boundary layer tests, respectively.

In this chapter, the summary of the results and outcomes of the presented work is shown. The overall outcomes and summary are presented at the beginning of Section 6.1. Then the author summarizes the mathematical details of the bridging model, the accuracy of the ray tracing solver, the validation of the Burgers' equation solver, the UFBLWT experimental results, and the numerical investigation of the bridging model in Section 6.1. In Section 6.2, potential improvements and applications of the solver are discussed.

6.1 Summary of Results

This dissertation employs experimental techniques to investigate the turbulent-acoustic interaction via propagating a specific test signal through turbulent flows within the UFBLWT. A positive correlation is observed between the acoustic signal's amplitude reduction and the TKE, where the amplitude drops from 0.237 Pa to 0.134 Pa with the increasing TKE from $0.246 \text{ m}^2/\text{s}^2$ to $0.467 \text{ m}^2/\text{s}^2$ at $EL = 900 \text{ mm}$. To numerically model this turbulent-acoustic interaction, a solver is developed to evaluate a modified Ostashev's turbulent scattering model [11]. The Burgers' equation solver is capable of capturing the nonlinearity, attenuation, and dispersion of acoustic propagation. Also, by applying the acoustic ray tracing approach, the numerical package

is able to capture the refraction caused by wind and temperature variations. The modified scattering model provides the Burgers' equation solver with the capability of capturing turbulent effects. Thus the final numerical package can capture the effects of nonlinearity, atmospheric attenuation and dispersion, refraction, and turbulence in propagation.

The Burgers' equation propagation solver and the ray tracing solver are presented in Chapter 3. The propagation solver is validated by comparing it with the Blackstock's [57] bridging function. The acoustic ray tracing solver is validated through comparison with Hallberg's [82] solver. Four propagation cases are presented in the Kansas City region, Oklahoma City region, Havana region, and Anchorage region. The eigenrays are captured, and related infrasound propagation are performed. For an intensive 3 Hz infrasound signal at 140 dB, the effect of wind on the nonlinearity of propagation is captured. The acoustic harmonics are captured for all upwind propagation within these four regions. For the downwind propagation cases, the nonlinearity only appears in the OKC region case. A broadband 120 dB infrasound propagation shows that atmospheric attenuation and geometric spreading are the main effects of infrasound propagation from a tornado.

Chapter 4 introduces the acoustic propagation experiment in the UFBLWT to investigate the turbulent-acoustic interaction. This interaction is clearly observed as the amplitude of the signal decreases with increasing turbulent intensity. The amplitude reduction parameter, σ_a , is used to quantify the turbulent attenuation. By increasing the EH from 0 to 50 mm, σ_a increases approximately 71.4%. For different frequencies, similar amplitude reductions are observed for the same combination of EH and EL.

In Chapter 5, the author numerically investigates the developed bridging model by performing sensitivity analysis and parameter dependence study. The validation of the bridging model is also included in this chapter, and a 2% improvement is obtained comparing to Ostashev's model when analyzing the UFBLWT data.

6.1.1 Summary of The Bridging Model for Acoustic-Turbulent Interaction

Acoustic-turbulent interaction has been studied since the 1950s to evaluate the role of turbulence during acoustic propagation. Lighthill [85] developed his scattering model by starting from the acoustic energy conservation and his acoustic analogy. Ostashev and Wilson [11] successfully developed a scattering model by solving the Helmholtz equation within the turbulent medium. Although the two models use different approaches, their final expressions converge to a similar equation as functions of TKE and integral length scale.

In present dissertation, a bridging model is developed to explore the turbulent scattering related to the low-frequency acoustic waves and large-scale turbulent structures. The refraction caused by the large-scale turbulence is included in the new model by using the classic ray theory and decomposed turbulent field. The author conducts a sensitivity analysis of the model to investigate the parameters' effects on the turbulent absorption coefficient. The acoustic propagation experiments within the UFBLWT are employed for model validation. The author also numerically investigates the model's behavior with the varying TKE and L_v . The results from the bridging model are compared with the results from Ostashev's model. The major outcomes from the mathematical derivation of the new bridging model are:

- The new concept, a subray tube, is created to account for the turbulent scattering with small scattering angle. The acoustic energy contained in the subray tube is expressed as a function of acoustic wave length λ , geodisc elements \mathbf{X} , and the turbulent fluctuation strain rate s_{ij} as $\frac{\lambda}{8\pi} X_{1,i} X_{2,i} \overline{s_{ij} s_{ij}} \cos(\mathbf{X}_1, \mathbf{X}_2)$.
- The Ostashev's model [11] (improved version of Tartaski's original model [88]) is modified and bridged with the new subray tube model. For small scattering angles, the bridging model switches to a turbulent refraction model, which is derived from the classic ray theory by decomposing the turbulent medium into a mean and fluctuating velocity.
- A sine function is used to bridge Ostashev's model and the turbulent refraction model. A characteristic turbulent wave number, k_l , represents the turbulent integral length scale. For scattering wavenumbers larger than k_l , the bridging model converges to Ostashev's scattering model for the cross-section calculation. For scattering wavenumbers smaller than k_l , the refraction model replaces the scattering model.
- The refracted cross-section σ_r is expressed by σ_v , L_v , and partial integration of the turbulent spectrum $E(k)$.

6.1.2 Summary of The Ray Tracing Solver and Burgers' Equation Solver

The acoustic ray tracing algorithm from Gainville [10] is implemented into a solver with the capability of importing realistic discrete weather information. A well-designed validation procedure is conducted to guarantee the ray tracing solver's accuracy. As a benchmark ray tracing solver, the solver of Hallberg et al. [82] is employed to validate the author's ray tracing solver via numerical comparisons. For the ray tracing solver, the validation and grid independence studies are conducted to explore the solver's accuracy. The Burgers' equation solver is validated by performing a nonlinear wave propagation case with varying conditions and comparing with the results of the Blackstock [57] bridging function. The attenuation effects of the developed solver are validated by comparing with the tabulated results of the Sutherland & Bass [68]. The cases examined for validation include tonal and broadband signals' propagation are conducted by the validated Burgers' equation solver. The main outcomes of the solver validation are:

- The results of the ray tracing solver are compared with Hallberg's solver. The turning point location is selected as the parameter to quantify the difference between the two solvers. Good agreement is observed between these two solvers as the maximum difference is 5.23%.
- The time-step-size dependency and mesh dependency is investigated for the ray tracing solver. Both tests show the convergent trends to a same turning point with increasing resolution.
- The Burgers' equation solver is validated with the results from Blackstock bridging function. Predicted shock formation distance is compared with the result from Blackstock bridging function to validate the solver. The L2 norm of the error of the solver is 1.82%.
- The atmospheric attenuation model is compared with Table IV in Sutherland and Bass [68]. For a 2000 Hz signal, the error is less than 1.02%.

6.1.3 Summary of the UFBLWT Propagation Experiments

The three stages of the experiments are introduced, and the equipment used in the experiment campaign is described. From the experimental results, the acoustic-turbulent interaction is observed as an attenuation effect, as the amplitude of the recorded acoustic signal decreases with increasing TKE. The major results and findings of the wind tunnel experiments are:

- On average, a 0.6 Pa amplitude reduction is observed at $EH = 0$ with the wind speed increasing from 0 to 10 m/s.
- For different frequencies, the recorded signals show a similar amplitude reduction pattern with respect to the wind speed at same EH and EL.
- For the $EH = 50$ mm cases, the amplitude reduction is approximately 0.8 Pa for the same wind speed increases as the $EH = 0$ cases. From $EH = 0$ to $EH = 50$ mm, the normalized variation of the amplitude ($\Delta A_{amp}/A_{source}$) increases from 0.3195 to 0.5473 at $EL = 170$ mm.
- The obtained experimental data provides the solver development with an reliable data base to modify the scattering model.
- The database of the UFBLWT experiments is published and well-documented on DesignSafe [152].

6.1.4 Summary of the Numerical Investigation of the Bridging Model

A series of numerical studies are conducted to investigate the new model's characteristics and its influence on the pressure time history of signals as they propagate. The bridging model is implemented into the generalized Burgers' equation solver for long-range propagation. Sensitivity analyses are conducted for both the model and solver. Varying TKE shows more influence than the length scale in both Ostashev's model and the bridging model as the normalized sensitivity of TKE is 2% for Ostashev's model and 2.012% for the bridging model, while the normalized sensitivity of L_v is lower than 1.1% for both models with frequency higher than 100 Hz. The overall sensitivity of the turbulent length scale in the bridging model is less than Ostashev's models. The sensitivity of TKE and length scale are also compared with other propagation parameters, including nonlinear coefficient β , atmospheric absorption α , signal amplitude p_{mag} , and propagation distance R . The TKE and length scale show stronger influence than atmospheric absorption as the sensitivity of TKE and L_v are larger than atmospheric attenuation. The major outcomes and results of the numerical investigations are:

- A characteristic turbulent wave number, k_l , represents the turbulent integral length scale. For scattering wavenumbers larger than k_l , the bridging model converges to Ostashev's scattering model for the cross-section calculation. For scattering wavenumbers smaller than k_l , the refraction model replaces the scattering model.

- The refracted cross-section σ_r is expressed by σ_v , L_v , and partial integration of the turbulent spectrum $E(k)$. A sine function bridges the refraction model and scattering model by matching its maximum value to the maximum cross-section.
- The OASPL of the received tornadic signal is used to analyze the overall influence of the bridging model. Both TKE and L_v contribute to a larger decrease of OASPL.
- These results showed that both Ostashev's and the new model make excellent predictions, and that there is a small improvement in prediction accuracy with the new model by approximately 1 to 2% over 22 m propagation.
- The TKE and L_v 's effects on predictions are presented, where the TKE primarily effects absorption, and L_v alters α_t .
- By implementing a realistic turbulent atmospheric model with the bridging model, a maximum absorption line is observed within the α_t contour. The maximum turbulent absorption for the 0.25 Hz is located at altitude of 8.2 km. As the frequency increases to 10 Hz, this maximum absorption altitude drops to 1.6 km. This variation is caused by the integrative action of the increasing L_v and decreasing TKE with the increasing altitude.
- A series of wind tunnel propagation experiments are conducted in the NSF UFBLWT to validate the newly developed bridging model. The experiments successfully captured the turbulent attenuation. The peak amplitude of the received signal varies from 0.22 Pa to 0.084 Pa, with the mean wind tunnel speed from 0 to 8.56 m/s.

6.2 Future Work

In the presented dissertation, the major innovations are the bridging acoustic-turbulent interaction model and the boundary layer wind tunnel propagation experiments. This unique model and corresponding experiment represent a new technique to capture turbulent effects during long-range propagation. However, there are still some limitations in the present approach. Currently, there is no wind tunnel that can create perfectly scaled atmospheres relative to the full atmospheric turbulent boundary layer (see [155, 156, 157]). The turbulent boundary layer created within the UFBLWT does not capture atmospheric temperature and air density fluctuations. Therefore, we do not expect the acoustic data from the UFBLWT to include the effects of acoustic refraction [158] due to the mean density gradients that are present in the atmosphere. However, the tunnel does allow acoustic waves to be modified by turbulence as observed in the present measurements. Furthermore, the wind tunnel is not an anechoic facility. The acoustics contain reflections from the walls of the tunnel. Waves in the facility follow a system described by Vaidya

and Dean [159], which correspond to duct acoustics [143]. To overcome this tunnel limitation, an ensemble averaging technique to capture the direct ray (geometric acoustics) and its effects from turbulence is implemented. This method allows us to remove the reflected waves from the tunnel walls, floor, and ceiling. Such reflections can in practice be eliminated from three of the walls of a wind tunnel by performing similar acoustic experiments in a wall-jet facility [160], but no such wall-jet wind tunnel with roughness elements exists. Finally, only a limited number of measurements along the ray paths of the acoustic waves from source to observer have been captured by the TCP system. This limitation is not a major issue because of the nature of the slowly varying boundary layer [161] after its initial rapid development near the tunnel entrance. In practice, these profiles are interpolated between measurement positions to approximate the entire profile for the validation of acoustic prediction codes. In the future, more boundary layer wind tunnel tests can facilitate further validation of the solver, or use tests in real atmosphere to help modelling the inhomogeneity of humidity and temperature. For the potential applications of the solver, explosion infrasound propagation and sonic boom propagation can be investigated and discussed. The detailed research discussion about these two solver applications are listed as the following.

6.2.1 Explosion Infrasound Propagation

Besides tornadic infrasound, an explosion is another major source of atmospheric infrasound. High power explosions generate powerful infrasound waves that propagate thousands of kilometers from the source. Therefore, infrasound from explosions are appropriate application for our numerical solver. Previous research [119, 162] mainly focuses on the propagation path and nonlinearity of the explosion infrasound. By applying the newly developed turbulent scattering model, our solver can capture the turbulent effects that occurs during long-range propagation. The source signal, as an “N” wave, needs to be resolved as the initial condition for the numerical solver. Based on previous studies [163, 164], the initial waveform can be calculated with the known trinitrotoluene (TNT) mass of the explosion.

In the future, the numerical replica of several famous high power explosions [165, 166, 162]

will be produced by our numerical solver. The solver’s predictions will be compared with the recordings from the International Monitor System (IMS). The IMS is designed and established to monitor any future entry into force of the Comprehensive Nuclear-Test-Ban Treaty (CTBT) by detecting and locating nuclear explosions [167]. As a part of the IMS, the infrasound monitoring network can provide us with the recorded infrasound signals related to the explosions via an Incorporated Research Institutions for Seismology (IRIS) data management system [168]. In the final dissertation, the turbulent-involved simulation results will be demonstrated and compared with the IMS recordings.

6.2.2 Sonic Boom Propagation

Another potential application of our solver is for sonic boom propagation. A sonic boom is a nonlinear acoustic wave associated with the shockwave created when an object travels through the air at supersonic speed [169]. Presently, potential low-boom aircraft are widely investigated as a commercial supersonic transportation solution while minimizing the signature on the ground. The ground signature of the low-boom aircraft is significantly more “acceptable” than the previous supersonic commercial jets. The ground signature is not only affected by the initial shockwave, but the effects of the propagation can also alter the waveform. The generalized Burgers’ equation is widely used for the sonic boom propagation [170]. However, one limitation of the generalized Burgers’ equation is that the turbulent effects cannot be captured by this one-dimensional approach directly. By applying our numerical solver, the attenuation of turbulent scattering can be included in the sonic boom propagation prediction.

In the future, the sonic boom study with our solver will be conducted in two stages. In the first stage, we will compare our prediction with a current state-of-the-art solver, which is PCBOOM [102]. The Sonic Boom Prediction Workshop (SBPW) hosted by the American Institute of Aeronautics and Astronautics (AIAA) published two cases of the sonic boom propagation predicted by PCBOOM [171]. We will calibrate our solver to reproduce the results to match PCBOOM results without the turbulence model.

APPENDIX DATA ORGANIZATION AND DESIGNSAFE STORAGE

All the experiment data is organized and stored in the DesignSafe Cyber Infrastructure as a published data repository. Figure A-1 shows the layout of the data and metadata files and how they are organized on the DesignSafe-CI Data Depot repository. The Data Depot repository

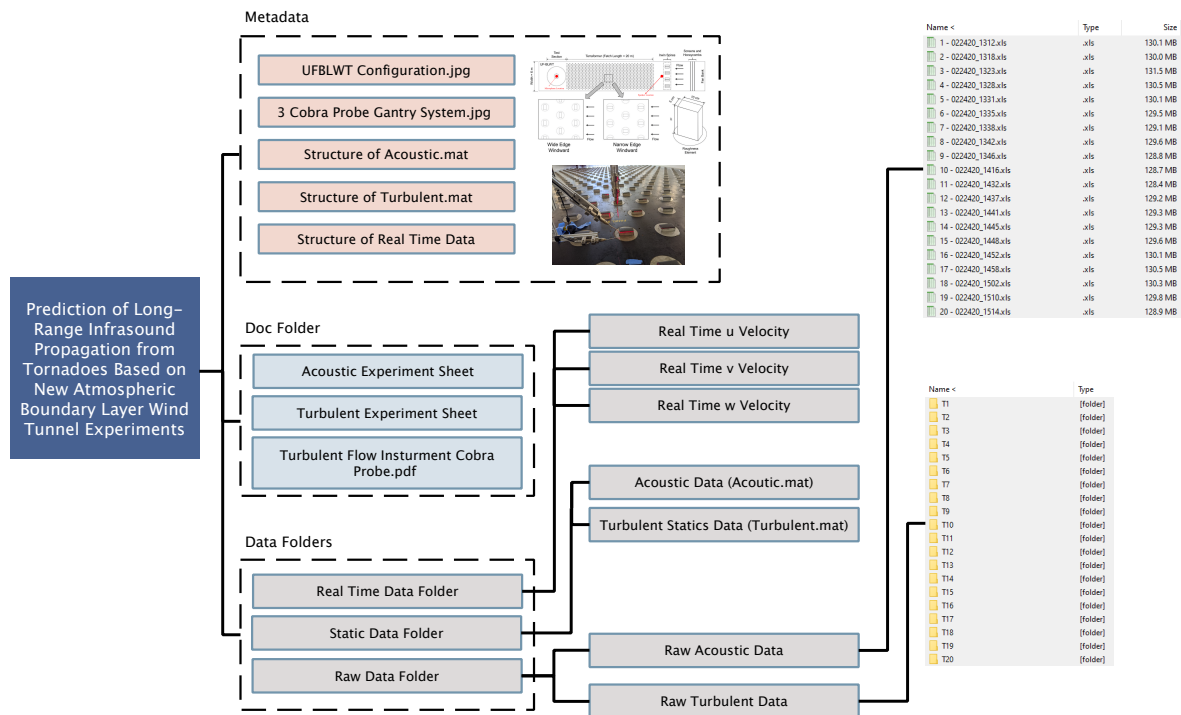


Figure A-1. Data Depot Structure

consists of three major sections: the Metadata, Document Folder, and Data Folder. The Metadata is a document which explains the content of the components of all the files included in the DesignSafe-CI Data Depot repository. It includes a brief introduction of the experimental setup, the experimental configuration, describes the content of the Matlab files, the type of data and resolution for both types: acoustic and turbulent, and finally explains the instrumentation and data processing. The Document Folder includes three different files: two sheets with the acoustic and the turbulent matrix (the Acoustic_test_sheet and the Turbulent_test_sheet), and a manual with the technical specifications of the cobra probes used in this set of experiments (TFI_Cobraprobe).

The acoustic and turbulent data are included in the Data Folder section, which is organized in three different folders according to the nature of the data: Real Time Data Folder, Static Data, and Raw Data Folder. The Real Time Data Folder includes the instantaneous flow velocity measurements, and the source signals recorded in the anechoic chamber. The instantaneous flow is stored in three separate Matlab files corresponding to each one of the three different components: u , v and w (Realtime_u_Velocity.mat, Realtime_v_Velocity.mat and Realtime_w_Velocity.mat). The first index of the velocity measurement is the setpoint number, which can be found in the Turbulent_test_sheet and the unit of the measurement is m/s. The source signals recorded in the anechoic chamber are contained in two Matlab files (SourceSignal_2m.mat and SourceSignal_3m.mat) for 2 m and 3 m away from the speaker, respectively.

Post-processed acoustic data (Acoustic.mat) and turbulent data (Turbulent.mat) are stored separately in the *Static Data* folder. The acoustic data is structured in 4 different fields: Microphone Elevation (EL), terraformer element height elevation (EH), estimated wind speed (WS) and the Frequency of the signal (Fr). In the first field, the tests are divided according to the microphone elevation, those values are 170 mm, 590mm, 740 mm and 900 mm. Once the microphone elevation of the test that the user wants to open is selected, it is possible to choose the second field, which is the terraformer element height elevation. In this case the options to select are 0 mm, 10 mm, 30 mm and 50 mm. The third field to select is the estimated wind speed of the test. As mentioned previously, for the acoustic tests there are 9 different wind speeds: 0 m/s, 2 m/s, 4 m/s, 5m/s, 6 m/s, 7 m/s, 8 m/s, 9 m/s and 10 m/s. Once each one of the fields is selected, the last field correspond to the frequency of the sound source. The values of the frequency per each one of the tests included in the acoustic portion are: 1250 Hz, 1600 Hz and 2000 Hz. For example, if the user requires data from the Acoustic.mat file, with a microphone elevation of 590 mm, terraformer elements height of 30 mm, estimated wind speed of 5 m/s and a frequency of 1250, it is possible access to the time series information through the next prompt once the Matlab file has been loaded: Acoustic.EL590.EH30.Wind5.Fr1250.

The turbulent data is structured in a similar way to the acoustic data, but in this case, in 3

different fields: the cobra probe location in z -direction (Z), terraformer element height elevation (EH) and cobra probe location in x -direction (X). In the first field, the tests are sorted according to the microphone elevation, those values are 170 mm, 590mm, 740 mm and 900 mm. Once the microphone elevation of the test that the user wants to open is selected, it is possible to choose the second field, which is the terraformer element height elevation. In this case the options to select are 0 mm and 30 mm. The third field to select is the cobra probe location in X -direction. The options for this are 2 m, 10 m, 16 m, and 20 m. Once each one of the fields is selected, it is possible to access different parameters for the group of tests such as the TKE, the time scale (Timescale), the integral time scale (IntegralTimeScale), the mean velocity U (MeanVelocityU) and the Integral length scale (IntegralLengthScale). For example, if the user requires data from the turbulence.mat file, with a cobra probe location at 590 mm in z -direction, terraformer elements height of 30 mm and a location of the cobra probes at 20 m in X -direction, it is possible access to the information through the next prompt once the Matlab file has been loaded:

Turbulence.Z590.EH30.X20

The raw data of both turbulence and acoustics are stored in the *Raw Data* folder. For the acoustic raw data, there are 144 recordings in the compressed file. The name of the recordings is designed as *setpoint number - date - time* format. For the setpoints from 1 to 156, the recordings are the same 144 acoustic tests used in the dataset, while the rest of the recordings are the calibration tests and the additional tests. The Acoustic_test_sheet is the acoustic test matrix, in where every acoustic recording can be tracked with its setpoint number along with the operating conditions like temperature, humidity and environmental static pressure. For the raw turbulent data, there are 128 subfolders insider the compressed turbulent raw data file. The name of the subfolder is the constructed by a letter “T” and a number. The “T” represents the turbulent test while the number is the setpoint number for the turbulent test. Similar to the raw acoustic data, the turbulent test subfolder can be tracked by the setpoint number in the Turbulent_test_sheet file under *Doc* folder. For each subfolder, there are three measurements with the extensions of .thA, .thB, and .thC, which represent the measurements of Probe 272, Probe 266 and Probe 256,

respectively, for subfolders from T1 to T42. For subfolders T42 to T144, The extensions .thA, .thB, and .thC represent the measurements of Probe 256, Probe 266 and Probe 272, respectively, due to the DaQ channel exchange.

REFERENCES

- [1] Paul, B. K., and Stimers, M., “Spatial Analyses of the 2011 Joplin Tornado Mortality: Deaths by Interpolated Damage Zones and Location of Victims,” *Weather, Climate, and Society*, Vol. 6, No. 2, 2014, pp. 161–174. doi:[10.1175/wcas-d-13-00022.1](https://doi.org/10.1175/wcas-d-13-00022.1).
- [2] Prevatt, D. O., Coulbourne, W., Graettinger, A. J., Pei, S., Gupta, R., and Grau, D., *Joplin, Missouri, Tornado of May 22, 2011*, American Society of Civil Engineers, 2012. doi:[10.1061/9780784412503](https://doi.org/10.1061/9780784412503).
- [3] Brooks, H. E., and Doswell, C. A., “Normalized Damage from Major Tornadoes in the United States: 1890–1999,” *Weather and Forecasting*, Vol. 16, No. 1, 2001, pp. 168–176. doi:[10.1175/1520-0434\(2001\)016<0168:ndfnti>2.0.co;2](https://doi.org/10.1175/1520-0434(2001)016<0168:ndfnti>2.0.co;2).
- [4] Dixon, P. G., Mercer, A. E., Choi, J., and Allen, J. S., “Tornado Risk Analysis: Is Dixie Alley an Extension of Tornado Alley?” *Bulletin of the American Meteorological Society*, Vol. 92, No. 4, 2011, pp. 433–441. doi:[10.1175/2010bams3102.1](https://doi.org/10.1175/2010bams3102.1).
- [5] Talmadge, C., and Waxler, R., “Infrasound from Tornadoes: Theory, Measurement, and Prospects for Their Use in Early Warning Systems,” *Acoust. Today*, Vol. 12, No. 1, 2016, pp. 43–51.
- [6] Yuan, M., Dickens-Micozzi, M., and Magsig, M. A., “Analysis of Tornado Damage Tracks from the 3 May Tornado Outbreak Using Multispectral Satellite Imagery,” *Weather and Forecasting*, Vol. 17, No. 3, 2002, pp. 382–398. doi:[10.1175/1520-0434\(2002\)017<0382:aotdtf>2.0.co;2](https://doi.org/10.1175/1520-0434(2002)017<0382:aotdtf>2.0.co;2).
- [7] Corfidi, S. F., Weiss, S. J., Kain, J. S., Corfidi, S. J., Rabin, R. M., and Levit, J. J., “Revisiting the 3–4 April 1974 Super Outbreak of Tornadoes,” *Weather and Forecasting*, Vol. 25, No. 2, 2010, pp. 465–510. doi:[10.1175/2009waf2222297.1](https://doi.org/10.1175/2009waf2222297.1).
- [8] Thompson, R. L., and Edwards, R., “An Overview of Environmental Conditions and Forecast Implications of the 3 May 1999 Tornado Outbreak,” *Weather and Forecasting*, Vol. 15, No. 6, 2000, pp. 682–699. doi:[10.1175/1520-0434\(2000\)015<0682:aooeca>2.0.co;2](https://doi.org/10.1175/1520-0434(2000)015<0682:aooeca>2.0.co;2).
- [9] Knupp, K. R., Murphy, T. A., Coleman, T. A., Wade, R. A., Mullins, S. A., Schultz, C. J., Schultz, E. V., Carey, L., Sherrer, A., McCaul, E. W., Carcione, B., Latimer, S., Kula, A., Laws, K., Marsh, P. T., and Klockow, K., “Meteorological Overview of the Devastating 27 April 2011 Tornado Outbreak,” *Bulletin of the American Meteorological Society*, Vol. 95, No. 7, 2014, pp. 1041–1062. doi:[10.1175/bams-d-11-00229.1](https://doi.org/10.1175/bams-d-11-00229.1).
- [10] Gainville, O., “Modeling of Atmospheric Propagation of Infrasound Waves by the Method of Nonlinear Ray Tracing,” Ph.D. thesis, Ecole Centrale de Lyon, 2008.
- [11] Ostashev, V. E., and Wilson, D. K., *Acoustics in moving inhomogeneous media*, CRC Press, 2015.
- [12] Drob, D., Emmert, J., Crowley, G., Picone, J., Shepherd, G., Skinner, W., Hays, P., Niciejewski, R., Larsen, M., She, C., et al., “An Empirical Model of the Earth’s Horizontal Wind Fields: HWM07,” *Journal of Geophysical Research: Space Physics*, Vol. 113, No. A12, 2008.

- [13] Picone, J., Hedin, A., Drob, D. P., and Aikin, A., “NRLMSISE-00 Empirical Model of the Atmosphere: Statistical Comparisons and Scientific Issues,” *Journal of Geophysical Research: Space Physics*, Vol. 107, No. A12, 2002, pp. SIA–15.
- [14] Miller, S. A. E., “Toward a Nonlinear Acoustic Analogy: Turbulence as a Source of Sound and Nonlinear Propagation,” *NASA/TM-2015-218706*, 2015.
- [15] Ostashev, V. E., and Wilson, D. K., “Coherence Function and Mean Field of Plane and Spherical Sound Waves Propagating through Inhomogeneous Anisotropic Turbulence,” *The Journal of the Acoustical Society of America*, Vol. 115, No. 2, 2004, pp. 497–506.
- [16] Blanc-Benon, P., Lipkens, B., Dallois, L., Hamilton, M. F., and Blackstock, D. T., “Propagation of Finite Amplitude Sound through Turbulence: Modeling with Geometrical Acoustics and the Parabolic Approximation,” *The Journal of the Acoustical Society of America*, Vol. 111, No. 1, 2002, pp. 487–498. doi:[10.1121/1.1404378](https://doi.org/10.1121/1.1404378).
- [17] Pierce, A. D., “Statistical Theory of Atmospheric Turbulence Effects on Sonic-Boom Rise Times,” *The Journal of the Acoustical Society of America*, Vol. 49, No. 3B, 1971, pp. 906–924.
- [18] Goldreich, P., and Kumar, P., “The Interaction of Acoustic Radiation with Turbulence,” *Astrophysical Journal*, Vol. 326, No. 1, 1988, pp. 462–478.
- [19] Brown, E. H., and Clifford, S., “On the Attenuation of Sound by Turbulence,” *The Journal of the Acoustical Society of America*, Vol. 60, No. 4, 1976, pp. 788–794.
- [20] Fujita, T., “Proposed Characterization of Tornadoes and Hurricanes by Area and Intensity,” Tech. rep., University of Chicago, Chicago, IL, 02 1971.
- [21] Potter, S., “Fine-Tuning Fujita: After 35 Years, a New Scale for Rating Tornadoes Takes Effect,” *Weatherwise*, Vol. 60, No. 2, 2007, pp. 64–71. doi:[10.3200/wewi.60.2.64-71](https://doi.org/10.3200/wewi.60.2.64-71).
- [22] Doswell, C. A., Brooks, H. E., and Dotzek, N., “On the Implementation of the Enhanced Fujita Scale in the USA,” *Atmospheric Research*, Vol. 93, No. 1-3, 2009, pp. 554–563. doi:[10.1016/j.atmosres.2008.11.003](https://doi.org/10.1016/j.atmosres.2008.11.003).
- [23] Doswell, C. A., Moller, A. R., and Brooks, H. E., “Storm Spotting and Public Awareness since the First Tornado Forecasts of 1948,” *Weather and Forecasting*, Vol. 14, No. 4, 1999, pp. 544–557. doi:[10.1175/1520-0434\(1999\)014<0544:ssapas>2.0.co;2](https://doi.org/10.1175/1520-0434(1999)014<0544:ssapas>2.0.co;2).
- [24] Bates, F. C., “Severe Local Storm Forecasts and Warnings and the General Public1,” *Bulletin of the American Meteorological Society*, Vol. 43, No. 7, 1962, pp. 288–291. doi:[10.1175/1520-0477-43.7.288](https://doi.org/10.1175/1520-0477-43.7.288).
- [25] Brotzge, J., and Donner, W., “The Tornado Warning Process: A Review of Current Research, Challenges, and Opportunities,” *Bulletin of the American Meteorological Society*, Vol. 94, No. 11, 2013, pp. 1715–1733. doi:[10.1175/bams-d-12-00147.1](https://doi.org/10.1175/bams-d-12-00147.1).

- [26] Leik, R., Carter, T., and Clark, J., “Community Response to Natural Hazard Warning,” , 1981.
- [27] Egentowich, J. M., Kaplan, M. L., Lin, Y.-L., and Riordan, A. J., “Mesoscale Simulations of Dynamical Factors Discriminating between a Tornado Outbreak and Non-Event over the Southeast US Part I: 84-48 Hour Precursors,” *Meteorology and Atmospheric Physics*, Vol. 74, No. 1-4, 2000, pp. 129–157. doi:[10.1007/s007030070030](https://doi.org/10.1007/s007030070030).
- [28] Clark, A. J., Kain, J. S., Marsh, P. T., Correia, J., Xue, M., and Kong, F., “Forecasting Tornado Pathlengths Using a Three-Dimensional Object Identification Algorithm Applied to Convection-Allowing Forecasts,” *Weather and Forecasting*, Vol. 27, No. 5, 2012, pp. 1090–1113. doi:[10.1175/waf-d-11-00147.1](https://doi.org/10.1175/waf-d-11-00147.1).
- [29] Trafalis, T. B., Adrianto, I., and Richman, M. B., “Active Learning with Support Vector Machines for Tornado Prediction,” *Computational Science – ICCS 2007*, Springer Berlin Heidelberg, Berlin, Heidelberg, 2007, pp. 1130–1137. doi:[0.1007/978-3-540-72584-8_148](https://doi.org/0.1007/978-3-540-72584-8_148).
- [30] Stout, G. E., and Huff, F. A., “CORRESPONDENCE,” *Bulletin of the American Meteorological Society*, Vol. 34, No. 6, 1953, pp. 281–284. doi:[10.1175/1520-0477-34.6.281](https://doi.org/10.1175/1520-0477-34.6.281).
- [31] Markowski, P. M., “Hook Echoes and Rear-Flank Downdrafts: A Review,” *Monthly Weather Review*, Vol. 130, No. 4, 2002, pp. 852–876. doi:[10.1175/1520-0493\(2002\)130<0852:hearfd>2.0.co;2](https://doi.org/10.1175/1520-0493(2002)130<0852:hearfd>2.0.co;2).
- [32] Brown, R. A., Bumgarner, W. C., Crawford, K. C., and Sirmans, D., “Preliminary Doppler Velocity Measurements in a Developing Radar Hook Echo,” *Bulletin of the American Meteorological Society*, Vol. 52, No. 12, 1971, pp. 1186–1188. doi:[10.1175/1520-0477\(1971\)052<1186:pdv mia>2.0.co;2](https://doi.org/10.1175/1520-0477(1971)052<1186:pdv mia>2.0.co;2).
- [33] Crum, T. D., and Alberty, R. L., “The WSR-88D and the WSR-88D Operational Support Facility,” *Bulletin of the American Meteorological Society*, Vol. 74, No. 9, 1993, pp. 1669–1687. doi:[10.1175/1520-0477\(1993\)074<1669:twatwo>2.0.co;2](https://doi.org/10.1175/1520-0477(1993)074<1669:twatwo>2.0.co;2).
- [34] Crum, T. D., Alberty, R. L., and Burgess, D. W., “Recording, Archiving, and Using WSR-88D Data,” *Bulletin of the American Meteorological Society*, Vol. 74, No. 4, 1993, pp. 645–653. doi:[10.1175/1520-0477\(1993\)074<0645:raauwd>2.0.co;2](https://doi.org/10.1175/1520-0477(1993)074<0645:raauwd>2.0.co;2), URL [https://doi.org/10.1175/1520-0477\(1993\)074<0645:raauwd>2.0.co;2](https://doi.org/10.1175/1520-0477(1993)074<0645:raauwd>2.0.co;2).
- [35] Stumpf, G. J., Witt, A., Mitchell, E. D., Spencer, P. L., Johnson, J. T., Eilts, M. D., Thomas, K. W., and Burgess, D. W., “The National Severe Storms Laboratory Mesocyclone Detection Algorithm for the WSR-88D,” *Weather and Forecasting*, Vol. 13, No. 2, 1998, pp. 304–326. doi:[10.1175/1520-0434\(1998\)013<0304:tnsslm>2.0.co;2](https://doi.org/10.1175/1520-0434(1998)013<0304:tnsslm>2.0.co;2).
- [36] Mitchell, E. D. W., Vasiloff, S. V., Stumpf, G. J., Witt, A., Eilts, M. D., Johnson, J. T., and Thomas, K. W., “The National Severe Storms Laboratory Tornado Detection Algorithm,” *Weather and Forecasting*, Vol. 13, No. 2, 1998, pp. 352–366. doi:[10.1175/1520-0434\(1998\)013<0352:tnsslt>2.0.co;2](https://doi.org/10.1175/1520-0434(1998)013<0352:tnsslt>2.0.co;2).

- [37] Brotzge, J., and Erickson, S., “NWS Tornado Warnings with Zero or Negative Lead Times,” *Weather and Forecasting*, Vol. 24, No. 1, 2009, pp. 140–154. doi:[10.1175/2008waf2007076.1](https://doi.org/10.1175/2008waf2007076.1).
- [38] Bryan, G. H., Wyngaard, J. C., and Fritsch, J. M., “Resolution Requirements for the Simulation of Deep Moist Convection,” *Monthly Weather Review*, Vol. 131, No. 10, 2003, pp. 2394–2416. doi:[10.1175/1520-0493\(2003\)131<2394:rrftso>2.0.co;2](https://doi.org/10.1175/1520-0493(2003)131<2394:rrftso>2.0.co;2).
- [39] Stensrud, D. J., Xue, M., Wicker, L. J., Kelleher, K. E., Foster, M. P., Schaefer, J. T., Schneider, R. S., Benjamin, S. G., Weygandt, S. S., Ferree, J. T., and Tuell, J. P., “Convective-Scale Warn-on-Forecast System,” *Bulletin of the American Meteorological Society*, Vol. 90, No. 10, 2009, pp. 1487–1500. doi:[10.1175/2009bams2795.1](https://doi.org/10.1175/2009bams2795.1).
- [40] Georges, T. M., “Infrasound from Convective Storms: Examining the Evidence,” *Reviews of Geophysics*, Vol. 11, No. 3, 1973, p. 571. doi:[10.1029/rg011i003p00571](https://doi.org/10.1029/rg011i003p00571), URL <https://doi.org/10.1029/rg011i003p00571>.
- [41] Bedard Jr, A. J., Bartram, B., Entwistle, B., Golden, J., Hodanish, S., Jones, R., Nishiyama, R., Keane, A., Mooney, L., Nicholls, M., et al., “Overview of the ISNET Data Set and Conclusions and Recommendations From a March 2004 Workshop to Review ISNET Data,” *Proceedings of the 22nd Conference on severe local storms, American Meteorological Society, Hyannis, MA, Paper*, Vol. 2, 2004.
- [42] Bedard Jr, A. J., Bartram, B., Keane, A., Welsh, D., and Nishiyama, R., “The Infrasound Network (ISNET): Background, Design details, and Display Capability as an 88D Adjunct Tornado Detection Tool,” *22nd Conf. On Severe Local Storms*, 2004.
- [43] Hodanish, S. J., “Comparison of Infrasonic Data and Doppler Velocity Radar Data: A Case Study of the 16 June 2004 Tornadic Supercell Over the Southeast Colorado Plains,” *22nd Conference on Severe Local Storms*, 2004.
- [44] Nicholls, M. E., Pielke Sr, R., and Bedard, A., “Preliminary Numerical Simulations of Infrasound Generation Processes by Severe Weather Using a Fully Compressible Numerical Model,” *Proceedings 22nd Conference on Severe Local Storms*, 2004, pp. 4–8.
- [45] Szoke, E. J., Bedard Jr, A., Thaler, E., and Glancy, R., “A Comparison of ISNet Data with Radar Data for Tornadic and Potentially Tornadic Storms in Northeast Colorado,” *Preprints, 22nd Conf. on Severe Local Storms, Hyannis, MA, Amer. Meteor. Soc.*, Vol. 1, 2004.
- [46] Lipkens, B., “Model Experiment to Study Sonic Boom Propagation through Turbulence. Part III: Validation of Sonic Boom Propagation Models,” *The Journal of the Acoustical Society of America*, Vol. 111, No. 1, 2002, pp. 509–519. doi:[10.1121/1.1371974](https://doi.org/10.1121/1.1371974), URL <https://doi.org/10.1121/1.1371974>.
- [47] Bowman, H. S., and Bedard, A. J., “Observations of Infrasound and Subsonic Disturbances Related to Severe Weather,” *Geophysical Journal of the Royal Astronomical Society*, Vol. 26, No. 1-4, 1971, pp. 215–242. doi:[10.1111/j.1365-246x.1971.tb03396.x](https://doi.org/10.1111/j.1365-246x.1971.tb03396.x).

- [48] Bowman, H. S., “Subsonic waves and severe weather phenomena,” *Proceedings of ESSA/ARPA Symposium on Acoustic Gravitational Waves in the Atmosphere, Boulder, Colorado*, 1968, pp. 215–222.
- [49] Akhalkatsi, M., and Gogoberidze, G., “Infrasound Generation by Tornadic Supercell Storms,” *Quarterly Journal of the Royal Meteorological Society*, Vol. 135, No. 641, 2009, pp. 935–940. doi:[10.1002/qj.421](https://doi.org/10.1002/qj.421).
- [50] Lighthill, M. J., “On Sound Generated Aerodynamically I. General theory,” *Proceedings of the Royal Society of London. Series A. Mathematical and Physical Sciences*, Vol. 211, No. 1107, 1952, pp. 564–587. doi:[10.1098/rspa.1952.0060](https://doi.org/10.1098/rspa.1952.0060).
- [51] Schecter, D. A., Nicholls, M. E., Persing, J., Bedard, A. J., and Pielke, R. A., “Infrasound Emitted by Tornado-Like Vortices: Basic Theory and a Numerical Comparison to the Acoustic Radiation of a Single-Cell Thunderstorm,” *Journal of the Atmospheric Sciences*, Vol. 65, No. 3, 2008, pp. 685–713. doi:[10.1175/2007jas2384.1](https://doi.org/10.1175/2007jas2384.1).
- [52] Akhalkatsi, M., and Gogoberidze, G., “Spectrum of Infrasound Radiation from Supercell Storms,” *Quarterly Journal of the Royal Meteorological Society*, Vol. 137, No. 654, 2011, pp. 229–235.
- [53] Elbing, B., Petrin, C., and S. Van Den Broeke, M., “Detection and Characterization of Infrasound from a Tornado,” 175th meeting of the Acoustical Society of America, 2018, pp. 1–40.
- [54] Bedard, A. J., “Low-Frequency Atmospheric Acoustic Energy Associated with Vortices Produced by Thunderstorms,” *Monthly Weather Review*, Vol. 133, No. 1, 2005, pp. 241–263. doi:[10.1175/mwr-2851.1](https://doi.org/10.1175/mwr-2851.1).
- [55] Frazier, W. G., Talmadge, C., Park, J., Waxler, R., and Assink, J., “Acoustic Detection, Tracking, and Characterization of Three Tornadoes,” *The Journal of the Acoustical Society of America*, Vol. 135, No. 4, 2014, pp. 1742–1751. doi:[10.1121/1.4867365](https://doi.org/10.1121/1.4867365).
- [56] Whitham, G. B., *Linear and Nonlinear Waves*, Vol. 42, John Wiley & Sons, 2011.
- [57] Blackstock, D. T., “Fundamentals of Physical Acoustics,” , 2001.
- [58] Bass, H., Sutherland, L., Piercy, J., and Evans, L., “Absorption of Sound by the Atmosphere,” *papm*, Vol. 17, 1984, pp. 145–232.
- [59] Sabatini, R., Marsden, O., Bailly, C., and Gainville, O., “Three-Dimensional Direct Numerical Simulation of Infrasound Propagation in the Earth’s Atmosphere,” *Journal of Fluid Mechanics*, Vol. 859, 2019, p. 754–789. doi:[10.1017/jfm.2018.816](https://doi.org/10.1017/jfm.2018.816).
- [60] Besset, C., and Blanc, E., “Propagation of Vertical Shock Waves in the Atmosphere,” *The Journal of the Acoustical Society of America*, Vol. 95, No. 4, 1994, pp. 1830–1839. doi:[10.1121/1.408689](https://doi.org/10.1121/1.408689).

- [61] Baskar, S., and Prasad, P., “Formulation of the Problem of Sonic Boom by a Maneuvering Aerofoil as a One-Parameter Family of Cauchy Problems,” *Proceedings of the Indian Academy of Sciences - Section A*, Vol. 116, No. 1, 2006, pp. 97–119. doi:[10.1007/bf02829742](https://doi.org/10.1007/bf02829742).
- [62] McDonald, B. E., and Kuperman, W. A., “Time Domain Formulation for Pulse Propagation Including Nonlinear Behavior at a Caustic,” *The Journal of the Acoustical Society of America*, Vol. 81, No. 5, 1987, pp. 1406–1417. doi:[10.1121/1.394546](https://doi.org/10.1121/1.394546).
- [63] Cleveland, R. O., Hamilton, M. F., and Blackstock, D. T., “Time-Domain Modeling of Finite-Amplitude Sound in Relaxing Fluids,” *The Journal of the Acoustical Society of America*, Vol. 99, No. 6, 1996, pp. 3312–3318. doi:[10.1121/1.414983](https://doi.org/10.1121/1.414983), URL <http://asa.scitation.org/doi/10.1121/1.414983>.
- [64] Drobzheva, Y. V., and Krasnov, V., “The Acoustic Field in the Atmosphere and Ionosphere Caused by a Point Explosion on the Ground,” *Journal of Atmospheric and Solar-Terrestrial Physics*, Vol. 65, No. 3, 2003, pp. 369–377. doi:[10.1016/s1364-6826\(02\)00141-4](https://doi.org/10.1016/s1364-6826(02)00141-4), URL [https://doi.org/10.1016/s1364-6826\(02\)00141-4](https://doi.org/10.1016/s1364-6826(02)00141-4).
- [65] Drobzheva, Y., and Krasnov, V., “Acoustic Energy Transfer to the Upper Atmosphere from Surface Chemical and Underground Nuclear Explosions,” *Journal of Atmospheric and Solar-Terrestrial Physics*, Vol. 68, No. 3-5, 2006, pp. 578–585. doi:[10.1016/j.jastp.2005.03.023](https://doi.org/10.1016/j.jastp.2005.03.023), URL <https://doi.org/10.1016/j.jastp.2005.03.023>.
- [66] Blanc, E., and Rickel, D., “Nonlinear Wave Fronts and Ionospheric Irregularities Observed by HF Sounding over a Powerful Acoustic Source,” *Radio Science*, Vol. 24, No. 3, 1989, pp. 279–288. doi:[10.1029/rs024i003p00279](https://doi.org/10.1029/rs024i003p00279).
- [67] Georges, T., “Instruments and Techniques for Thunderstorm Observation and Analysis,” , 1988.
- [68] Sutherland, L. C., and Bass, H. E., “Atmospheric Absorption in the Atmosphere up to 160 km,” *The Journal of the Acoustical Society of America*, Vol. 115, No. 3, 2004, pp. 1012–1032. doi:[10.1121/1.1631937](https://doi.org/10.1121/1.1631937).
- [69] Lighthill, M. J., “Viscosity Effects in Sound Waves of Finite Amplitude,” *Surveys in mechanics*, Vol. 250351, 1956.
- [70] Pichon, A. L., Blanc, E., and Hauchecorne, A. (eds.), *Infrasound Monitoring for Atmospheric Studies*, Springer Netherlands, 2009. doi:[10.1007/978-1-4020-9508-5](https://doi.org/10.1007/978-1-4020-9508-5).
- [71] McKenna, S. M. H., “Infrasound Wave Propagation Over Near-Regional and Tele-Infrasonic Distances,” Ph.D. thesis, Southern Methodist University, 2005.
- [72] Pekeris, C., “Theory of Propagation of Sound in a Half-space of Variable Sound Velocity under Conditions of Formation of a Shadow Zone,” *The journal of the acoustical society of America*, Vol. 18, No. 2, 1946, pp. 295–315.

- [73] Kwan, A., Dudley, J., and Lantz, E., “Who Really Discovered Snell’s Law?” *Physics World*, Vol. 15, No. 4, 2002, p. 64.
- [74] Dushaw, B., Howe, B., Mercer, J., Spindel, R., Baggeroer, A., Menemenlis, D., Wunsch, C., Birdsall, T., Metzger, K., Clark, C., Colosi, J., Comuelle, B., Dzieciuch, M., Munk, W., Worcester, P., Costa, D., and Forbes, A., “Multimegameter-range Acoustic Data Obtained by Bottom-mounted Hydrophone Arrays for Measurement of Ocean Temperature,” *IEEE Journal of Oceanic Engineering*, Vol. 24, No. 2, 1999, pp. 202–214. doi:[10.1109/48.757271](https://doi.org/10.1109/48.757271).
- [75] Uffelen, L. J. V., Worcester, P. F., Dzieciuch, M. A., Rudnick, D. L., and Colosi, J. A., “Effects of Upper Ocean Sound-speed Structure on Deep Acoustic Shadow-zone Arrivals at 500- and 1000-km range,” *The Journal of the Acoustical Society of America*, Vol. 127, No. 4, 2010, pp. 2169–2181. doi:[10.1121/1.3292948](https://doi.org/10.1121/1.3292948).
- [76] Esclangon, E., “L’acoustique des Canons et des Projectiles (Imprimerie Nationale, Paris),” 1925.
- [77] Guiraud, J.-P., “Acoustique Geometrique Bruit Balistique des Avions Supersoniques et Focalisation,” *Journal de Mecanique*, Vol. 4, No. 2, 1965, p. 215.
- [78] Hayes, W. D., and Runyan Jr, H. L., “Sonic-Boom Propagation through a Stratified Atmosphere,” *The Journal of the Acoustical Society of America*, Vol. 51, No. 2C, 1972, pp. 695–701.
- [79] Friedman, M. P., Kane, E. J., and Sigalla, A., “Effects of Atmosphere and Aircraft Motion on the Location and Intensity of a Sonic Boom,” *AIAA Journal*, Vol. 1, No. 6, 1963, pp. 1327–1335.
- [80] Maglieri, D. J., Hilton, D. A., and McLeod, N. J., *Experiments on the Effects of Atmospheric Refraction and Airplane Accelerations on Sonic-boom Ground-pressure Patterns*, Vol. 3520, National Aeronautics and Space Administration, 1966.
- [81] Coulouvrat, F., “Sonic Boom in the Shadow Zone: A Geometrical Theory of Diffraction,” *The Journal of the Acoustical Society of America*, Vol. 111, No. 1, 2002, pp. 499–508.
- [82] Hallberg, B., Larsson, C., and Israelsson, S., “Numerical Ray Tracing in the Atmospheric Surface Layer,” *The Journal of the Acoustical Society of America*, Vol. 83, No. 6, 2005, pp. 2059–2068. doi:[10.1121/1.396386](https://doi.org/10.1121/1.396386).
- [83] Thompson, R. J., “Ray-Acoustic Intensity in a Moving Medium. I,” *The Journal of the Acoustical Society of America*, Vol. 55, No. 4, 2005, pp. 729–732. doi:[10.1121/1.1914590](https://doi.org/10.1121/1.1914590).
- [84] Thompson, R. J., “Ray-Acoustic Intensity in a Moving Medium. II. A Stratified medium,” *The Journal of the Acoustical Society of America*, Vol. 55, No. 4, 2005, pp. 733–737. doi:[10.1121/1.1914591](https://doi.org/10.1121/1.1914591).

- [85] Lighthill, M. J., “On the Energy Scattered from the Interaction of Turbulence with Sound or Shock Waves,” *Mathematical Proceedings of the Cambridge Philosophical Society*, Vol. 49, No. 3, 1953, pp. 531–551. doi:[10.1017/s0305004100028693](https://doi.org/10.1017/s0305004100028693), URL <https://doi.org/10.1017/s0305004100028693>.
- [86] Pierce, A. D., *Acoustics: an Introduction to Its Physical Principles and Applications*, Springer, 2019.
- [87] Piacsek, A. A., “Atmospheric Turbulence Conditions Leading to Focused and Folded Sonic Boom Wave Fronts,” *The Journal of the Acoustical Society of America*, Vol. 111, No. 1, 2002, pp. 520–529.
- [88] Tatarski, V. I., *Wave Propagation in a Turbulent Medium*, Dover Publication, 1967.
- [89] Newton, R. G., *Scattering theory of waves and particles*, Springer Science & Business Media, 2013.
- [90] Rozanova, A., “The Khokhlov–Zabolotskaya–Kuznetsov Equation,” *Comptes Rendus Mathematique*, Vol. 344, No. 5, 2007, pp. 337 – 342. doi:<https://doi.org/10.1016/j.crma.2007.01.010>.
- [91] Stout, T. A., Blanc-benon, P., and Reichard, K., “Simulation of N-Wave and Shaped Supersonic Signature Turbulent Variations,” Ph.D. thesis, Pennsylvania State University, 2018.
- [92] Rathsam, J., Loubeau, A., and Klos, J., *A study in a new test facility on indoor annoyance caused by sonic booms*, National Aeronautics and Space Administration, Langley Research Center, 2012.
- [93] Aver’yanov, M. V., Khokhlova, V. A., Sapozhnikov, O. A., Blanc-Benon, P., and Cleveland, R. O., “Parabolic Equation for Nonlinear Acoustic Wave Propagation in Inhomogeneous Moving Media,” *Acoustical Physics*, Vol. 52, No. 6, 2006, pp. 623–632. doi:[10.1134/s1063771006060017](https://doi.org/10.1134/s1063771006060017).
- [94] Crighton, D. G., “Model Equations of Nonlinear Acoustics,” *Annual Review of Fluid Mechanics*, Vol. 11, No. 1, 2003, pp. 11–33. doi:[10.1146/annurev.fl.11.010179.000303](https://doi.org/10.1146/annurev.fl.11.010179.000303).
- [95] Blackstock, D. T., “Generalized Burgers Equation for Plane Waves,” *The Journal of the Acoustical Society of America*, Vol. 77, No. 6, 2005, pp. 2050–2053. doi:[10.1121/1.391778](https://doi.org/10.1121/1.391778).
- [96] Saxena, S., Morris, P. J., and Viswanathan, K., “Algorithm for the Nonlinear Propagation of Broadband Jet Noise,” *AIAA Journal*, Vol. 47, No. 1, 2008, pp. 186–194. doi:[10.2514/1.38122](https://doi.org/10.2514/1.38122).
- [97] Lee, S., Brentner, K. S., Farassat, F., and Morris, P. J., “Analytic Formulation and Numerical Implementation of an Acoustic Pressure Gradient Prediction,” *Journal of Sound and Vibration*, Vol. 319, No. 3-5, 2009, pp. 1200–1221. doi:[10.1016/j.jsv.2008.06.028](https://doi.org/10.1016/j.jsv.2008.06.028).

- [98] M., J., “Ray Trace Modeling of Underwater Sound Propagation,” *Modeling and Measurement Methods for Acoustic Waves and for Acoustic Microdevices*, InTech, 2013. doi:[10.5772/55935](https://doi.org/10.5772/55935), URL <https://doi.org/10.5772/55935>.
- [99] Plotkin, K. J., Downing, M., and Page, J., “USAF Single Event Sonic Boom Prediction Model: PCBOOM,” *The Journal of the Acoustical Society of America*, Vol. 95, No. 5, 1994, pp. 2839–2839. doi:[10.1121/1.409605](https://doi.org/10.1121/1.409605).
- [100] Pierces, A. D., and Rad, A., “The MultiPlayer,” Vol. 19, No. 628, 1967.
- [101] Bass, H. E., Bauer, H., and Evans, L. B., “Atmospheric Absorption of Sound: Analytical Expressions,” *The Journal of the Acoustical Society of America*, Vol. 52, No. 3B, 2005, pp. 821–825. doi:[10.1121/1.1913183](https://doi.org/10.1121/1.1913183).
- [102] Lonzaga, J. B., Waxler, R. M., Assink, J. D., and Talmadge, C. L., “Modelling Waveforms of Infrasound Arrivals from Impulsive Sources Using Weakly Non-linear Ray Theory,” *Geophysical Journal International*, Vol. 200, No. 3, 2015, pp. 1347–1361. doi:[10.1093/gji/ggu479](https://doi.org/10.1093/gji/ggu479).
- [103] Averiyarov, M., Blanc-Benon, P., Cleveland, R. O., and Khokhlova, V., “Nonlinear and Diffraction Effects in Propagation of N-waves in Randomly Inhomogeneous Moving Media,” *The Journal of the Acoustical Society of America*, Vol. 129, No. 4, 2011, pp. 1760–1772. doi:[10.1121/1.3557034](https://doi.org/10.1121/1.3557034).
- [104] Aumann, A. R., Tuttle, B. C., Chapin, W. L., and Rizzi, S. A., “The NASA Auralization Framework and plugin architecture,” *INTER-NOISE and NOISE-CON Congress and Conference Proceedings*, Vol. 250, Institute of Noise Control Engineering, 2015, pp. 1932–1943.
- [105] Wyngaard, J. C., *Turbulence in the Atmosphere*, Cambridge University Press, 2010. doi:[10.1017/CBO9780511840524](https://doi.org/10.1017/CBO9780511840524).
- [106] Garratt, J., *The Atmospheric Boundary Layer*, Cambridge Atmospheric and Space Science Series, Cambridge University Press, 1994.
- [107] VanZanten, M. C., Duynkerke, P. G., and Cuijpers, J. W. M., “Entrainment Parameterization in Convective Boundary Layers,” *Journal of the Atmospheric Sciences*, Vol. 56, No. 6, 1999, pp. 813–828. doi:[10.1175/1520-0469\(1999\)056<0813:EPICBL>2.0.CO;2](https://doi.org/10.1175/1520-0469(1999)056<0813:EPICBL>2.0.CO;2).
- [108] Deardorff, J. W., “Numerical Investigation of Neutral and Unstable Planetary Boundary Layers,” *Journal of the Atmospheric Sciences*, Vol. 29, No. 1, 1972, pp. 91–115. doi:[10.1175/1520-0469\(1972\)029<0091:NIONAU>2.0.CO;2](https://doi.org/10.1175/1520-0469(1972)029<0091:NIONAU>2.0.CO;2).
- [109] Barrick, J. D., Ritter, J. A., Watson, C. E., Wynkoop, M. W., and Quinn, J. K., “Calibration of NASA turbulent air motion measurement system,” 1996.

- [110] Cho, J. Y. N., Newell, R. E., Anderson, B. E., Barrick, J. D. W., and Thornhill, K. L., “Characterizations of Tropospheric Turbulence and Stability Layers from Aircraft Observations,” *Journal of Geophysical Research: Atmospheres*, Vol. 108, No. D20, 2003. doi:[10.1029/2002JD002820](https://doi.org/10.1029/2002JD002820).
- [111] Cohn, S. A., “Radar Measurements of Turbulent Eddy Dissipation Rate in the Troposphere: A Comparison of Techniques,” *Journal of Atmospheric and Oceanic Technology*, Vol. 12, No. 1, 1994, pp. 85–95. doi:[10.1175/1520-0426\(1995\)012<0085:RMOTED>2.0.CO;2](https://doi.org/10.1175/1520-0426(1995)012<0085:RMOTED>2.0.CO;2).
- [112] Azouit, M., and Vernin, J., “Remote Investigation of Tropospheric Turbulence by Two-Dimensional Analysis of Stellar Scintillation,” *Journal of the Atmospheric Sciences*, Vol. 37, No. 7, 1980, pp. 1550–1557. doi:[10.1175/1520-0469\(1980\)037<1550:RIOTTB>2.0.CO;2](https://doi.org/10.1175/1520-0469(1980)037<1550:RIOTTB>2.0.CO;2).
- [113] Lindgren, E. A., Sheshadri, A., Podglajen, A., and Carver, R. W., “Seasonal and Latitudinal Variability of the Gravity Wave Spectrum in the Lower Stratosphere,” *Journal of Geophysical Research: Atmospheres*, Vol. 125, No. 18, 2020, p. e2020JD032850. doi:[10.1029/2020JD032850](https://doi.org/10.1029/2020JD032850).
- [114] Bacmeister, J. T., Eckermann, S. D., Newman, P. A., Lait, L., Chan, K. R., Loewenstein, M., Proffitt, M. H., and Gary, B. L., “Stratospheric Horizontal Wavenumber Spectra of Winds, Potential Temperature, and Atmospheric Tracers Observed by High-Altitude Aircraft,” *Journal of Geophysical Research: Atmospheres*, Vol. 101, No. D5, 1996, pp. 9441–9470. doi:[10.1029/95JD03835](https://doi.org/10.1029/95JD03835).
- [115] Lilly, D. K., and Lester, P. F., “Waves and Turbulence in the Stratosphere,” *Journal of the Atmospheric Sciences*, Vol. 31, No. 3, 1974, pp. 800–812. doi:[10.1175/1520-0469\(1974\)031<0800:WATITS>2.0.CO;2](https://doi.org/10.1175/1520-0469(1974)031<0800:WATITS>2.0.CO;2).
- [116] Woodman, R. F., and Guillen, A., “Radar Observations of Winds and Turbulence in the Stratosphere and Mesosphere,” *Journal of the Atmospheric Sciences*, Vol. 31, No. 2, 1974, pp. 493–505. doi:[10.1175/1520-0469\(1974\)031<0493:ROOWAT>2.0.CO;2](https://doi.org/10.1175/1520-0469(1974)031<0493:ROOWAT>2.0.CO;2).
- [117] Gage, K. S., and Balsley, B. B., “On the Scattering and Reflection Mechanisms Contributing to Clear Air Radar Echoes from the Troposphere, Stratosphere, and Mesosphere,” *Radio Science*, Vol. 15, No. 2, 1980, pp. 243–257. doi:[10.1029/RS015i002p00243](https://doi.org/10.1029/RS015i002p00243).
- [118] Lukin, V., “Atmospheric Turbulence Parameters Measurements,” *Astronomical Site Evaluation in the Visible and Radio Range*, Astronomical Society of the Pacific Conference Series, Vol. 266, edited by J. Vernin, Z. Benkhaldoun, and C. Muñoz-Tuñón, 2002, p. 18.
- [119] Gainville, O., Blanc-Benon, P., and Scott, J., “Infrasound Propagation in Realistic Atmosphere Using Nonlinear Ray Theory,” *AIP Conference Proceedings*, Vol. 1474, American Institute of Physics, 2012, pp. 343–346.
- [120] Hedin, A., Fleming, E., Manson, A., Schmidlin, F., Avery, S., Clark, R., Franke, S., Fraser, G., Tsuda, T., Vial, F., and Vincent, R., “Empirical wind model for the upper, middle and

- lower atmosphere,” *Journal of Atmospheric and Terrestrial Physics*, Vol. 58, No. 13, 1996, pp. 1421–1447. doi:[10.1016/0021-9169\(95\)00122-0](https://doi.org/10.1016/0021-9169(95)00122-0).
- [121] Picone, J. M., Hedin, A. E., Drob, D. P., and Aikin, A. C., “NRLMSISE-00 empirical model of the atmosphere: Statistical comparisons and scientific issues,” *Journal of Geophysical Research: Space Physics*, Vol. 107, No. A12, 2002, pp. S15–1–S15–16. doi:[10.1029/2002ja009430](https://doi.org/10.1029/2002ja009430).
- [122] Scott, J., Blanc-Benon, P., and Gainville, O., “Weakly Nonlinear Propagation of Small-wavelength, Impulsive Acoustic Waves in a General Atmosphere,” *Wave Motion*, Vol. 72, 2017, pp. 41–61. doi:<https://doi.org/10.1016/j.wavemoti.2016.12.005>.
- [123] Blackburn, H. M., and Sherwin, S. J., “Formulation of a Galerkin Spectral Element-Fourier Method for Three-Dimensional Incompressible Flows in Cylindrical Geometries,” *Journal of Computational Physics*, Vol. 197, No. 2, 2004, pp. 759–778. doi:[10.1016/j.jcp.2004.02.013](https://doi.org/10.1016/j.jcp.2004.02.013).
- [124] Oboukhov, A., “Structure of the Temperature Field in Turbulent Flows,” *Isv. Geogr. Geophys. Ser.*, Vol. 13, 1949, pp. 58–69.
- [125] Tennekes, H., and Lumley, J. L., *A first course in turbulence*, MIT press, 2018.
- [126] Sreenivasan, K. R., “An update on the energy dissipation rate in isotropic turbulence,” *Physics of Fluids*, Vol. 10, No. 2, 1998, pp. 528–529. doi:[10.1063/1.869575](https://doi.org/10.1063/1.869575).
- [127] Kamrath, M. J., Ostashev, V. E., Wilson, D. K., White, M. J., Hart, C. R., and Finn, A., “Vertical and slanted sound propagation in the near-ground atmosphere: Amplitude and phase fluctuations,” *The Journal of the Acoustical Society of America*, Vol. 149, No. 3, 2021, pp. 2055–2071. doi:[10.1121/10.0003820](https://doi.org/10.1121/10.0003820), URL <https://doi.org/10.1121/10.0003820>.
- [128] Blackstock, D. T., “Connection between the Fay and Fubini Solutions for Plane Sound Waves of Finite Amplitude,” *The Journal of the Acoustical Society of America*, Vol. 39, No. 6, 1966, pp. 1019–1026. doi:[10.1121/1.1909986](https://doi.org/10.1121/1.1909986), URL <https://doi.org/10.1121/1.1909986>.
- [129] Markowski, P. M., “What is the Intrinsic Predictability of Tornadic Supercell Thunderstorms?” *Monthly Weather Review*, Vol. 148, No. 8, 2020, pp. 3157–3180. doi:[10.1175/mwr-d-20-0076.1](https://doi.org/10.1175/mwr-d-20-0076.1).
- [130] Talmadge, C., and Waxler, R., “Infrasound from Tornados: Theory Measurement and Prospects for Their Use in Early Warning Systems,” *Acoustics Today*, Vol. 12, No. 1, 2016, pp. 43–51.
- [131] Fernández-Cabán, P. L., and Masters, F. J., “Experiments in a Large Boundary Layer Wind Tunnel: Upstream Terrain Effects on Surface Pressures Acting on a Low-Rise Structure,” *Journal of Structural Engineering*, Vol. 146, No. 8, 2020, p. 04720002. doi:[10.1061/\(asce\)st.1943-541x.0002690](https://doi.org/10.1061/(asce)st.1943-541x.0002690).

- [132] “UFBLWT terraformer introduction,” <https://ufl.designsafe-ci.org/>, ????. Accessed: 2020-03-01.
- [133] Fernández-Cabán, P. L., and Masters, F. J., “Effects of Freestream Turbulence on the Pressure Acting on a Low-Rise Building Roof in the Separated Flow Region,” *Frontiers in Built Environment*, Vol. 4, 2018. doi:[10.3389/fbuil.2018.00017](https://doi.org/10.3389/fbuil.2018.00017).
- [134] Catarelli, R., Fernández-Cabán, P., Masters, F., Bridge, J., Gurley, K., and Matyas, C., “Automated Terrain Generation for Precise Atmospheric Boundary Layer Simulation in the Wind Tunnel,” *Journal of Wind Engineering and Industrial Aerodynamics*, Vol. 207, 2020, p. 104276. doi:[10.1016/j.jweia.2020.104276](https://doi.org/10.1016/j.jweia.2020.104276).
- [135] Fernández-Cabán, P., Masters, F., and Phillips, B., “Predicting Roof Pressures on a Low-Rise Structure from Freestream Turbulence Using Artificial Neural Networks,” *Frontiers in Built Environment*, Vol. 4, No. 68, 2018.
- [136] Brouwer, H. H., “Anechoic Wind Tunnels,” *National Aerospace Laboratory, NLR*, 1997.
- [137] Remillieux, M., Crede, E., Camargo, H., Burdisso, R., Devenport, W., Rasnick, M., Seeters, P. V., and Chou, A., “Calibration and Demonstration of the New Virginia Tech Anechoic Wind Tunnel,” *14th AIAA/CEAS Aeroacoustics Conference (29th AIAA Aeroacoustics Conference)*, American Institute of Aeronautics and Astronautics, 2008. doi:[10.2514/6.2008-2911](https://doi.org/10.2514/6.2008-2911).
- [138] Mathew, J., Bahr, C., Sheplak, M., Carroll, B., and Cattafesta, L. N., “Characterization of an Anechoic Wind Tunnel Facility,” *Noise Control and Acoustics*, ASMEDC, 2005. doi:[10.1115/imece2005-81737](https://doi.org/10.1115/imece2005-81737).
- [139] Holloway, C., McKenna, P., Dalke, R., Perala, R., and Devor, C., “Time-Domain Modeling, Characterization, and Measurements of Anechoic and Semi-Anechoic Electromagnetic Test Chambers,” *IEEE Transactions on Electromagnetic Compatibility*, Vol. 44, No. 1, 2002, pp. 102–118. doi:[10.1109/15.990716](https://doi.org/10.1109/15.990716), URL <https://doi.org/10.1109/15.990716>.
- [140] Baals, D. D., *Wind Tunnels of NASA*, Vol. 440, Scientific and Technical Information Branch, National Aeronautics and Space Administration, Washington D. C., 1981.
- [141] Duell, E. G., Walter, J., Yen, J., and Nagle, T., “Progress in Aeroacoustic and Climatic Wind Tunnels for Automotive Wind Noise and Acoustic Testing,” *SAE International Journal of Passenger Cars - Mechanical Systems*, Vol. 6, No. 1, 2013, pp. 448–461. doi:[10.4271/2013-01-1352](https://doi.org/10.4271/2013-01-1352).
- [142] Sovardi, C., Jaensch, S., and Polifke, W., “Concurrent Identification of Aero-Acoustic Scattering and Noise Sources at a Flow Duct Singularity in Low Mach Number Flow,” *Journal of Sound and Vibration*, Vol. 377, 2016, pp. 90–105. doi:[10.1016/j.jsv.2016.05.025](https://doi.org/10.1016/j.jsv.2016.05.025).

- [143] Pridmore-Brown, D. C., “Sound Propagation in a Fluid Flowing through an Attenuating Duct,” *The Journal of the Acoustical Society of America*, Vol. 30, No. 7, 1958, pp. 670–670. doi:[10.1121/1.1929943](https://doi.org/10.1121/1.1929943).
- [144] Mathew, J., Bahr, C., Sheplak, M., Carroll, B., and Cattafesta, L. N., “Characterization of an Anechoic Wind Tunnel Facility,” *Noise Control and Acoustics*, ASMEDC, 2005. doi:[10.1115/imece2005-81737](https://doi.org/10.1115/imece2005-81737), URL <https://doi.org/10.1115/imece2005-81737>.
- [145] Mathew, J., Bahr, C., Carroll, B., Sheplak, M., and Cattafesta, L., “Design, Fabrication, and Characterization of an Anechoic Wind Tunnel Facility,” *11th AIAA/CEAS Aeroacoustics Conference*, American Institute of Aeronautics and Astronautics, 2005. doi:[10.2514/6.2005-3052](https://doi.org/10.2514/6.2005-3052).
- [146] Catarelli, R. A., Fernández-Cabán, P. L., Phillips, B. M., Bridge, J. A., Masters, F. J., Gurley, K. R., and Prevatt, D. O., “Automation and New Capabilities in the University of Florida NHERI Boundary Layer Wind Tunnel,” *Frontiers in Built Environment*, Vol. 6, 2020. doi:[10.3389/fbuil.2020.558151](https://doi.org/10.3389/fbuil.2020.558151).
- [147] Turbulent Flow Instrumentation, *Cobra Probe of Turbulent Flow Instrumentation*, Turbulent Flow Instrumentation, 2015. URL <https://www.turbulentflow.com.au/Products/CobraProbe/CobraProbe.php>.
- [148] Allen, C., and Soderman, P., “Aeroacoustic Probe Design for Microphone to Reduce Flow-Induced Self-Noise,” *15th Aeroacoustics Conference*, American Institute of Aeronautics and Astronautics, 1993. doi:[10.2514/6.1993-4343](https://doi.org/10.2514/6.1993-4343).
- [149] Zhang, T., Ojeda, M., Miller, S., and Gurley, K., “Acoustic propagation experiments in a turbulent atmosphere,” , 2021. doi:[10.17603/DS2-BPAV-8W29](https://doi.org/10.17603/DS2-BPAV-8W29).
- [150] Foken, T., and Nappo, C., *Micrometeorology*, Springer-Verlag Berlin Heidelberg, 2008.
- [151] G.R.A.S. Sound & Vibration, *GRAS 46AZ 1/2” CCP Free-field Standard Microphone Set, Low Frequency*, G.R.A.S. Sound & Vibration, 2015. URL <https://www.grasacoustics.com/products/measurement-microphone-sets/constant-current-power-ccp/product/692-46az>.
- [152] Zhang, T., Ojeda-Tuz, M. A., Gurley, K. R., and Miller, S. A. E., “Experiments in a Large-Boundary Layer Wind Tunnel: Propagation of Noise through the Turbulent Boundary Layer,” *Journal of Structure Engineering*, 2020.
- [153] Apsley, D. D., and Castro, I. P., “A limited-length-scale k - ϵ model for the neutral and stably-stratified atmospheric boundary layer,” *Boundary-layer meteorology*, Vol. 83, No. 1, 1997, pp. 75–98.
- [154] Taylor, M. E., “Grazing rays and reflection of singularities of solutions to wave equations,” *Communications in Pure Applied Mathematics*, Vol. 29, 1976, pp. 1–38.

- [155] Cook, N., “Wind-Tunnel Simulation of the Adiabatic Atmospheric Boundary Layer by Roughness, Barrier and Mixing-Device Methods,” *Journal of Wind Engineering and Industrial Aerodynamics*, Vol. 3, No. 2-3, 1978, pp. 157–176. doi:[10.1016/0167-6105\(78\)90007-7](https://doi.org/10.1016/0167-6105(78)90007-7).
- [156] Pelt, R. S. V., Zobeck, T. M., Baddock, M. C., and Cox, J. J., “Design, Construction, and Calibration of a Portable Boundary Layer Wind Tunnel for Field Use,” *Transactions of the ASABE*, Vol. 53, No. 5, 2010, pp. 1413–1422. doi:[10.13031/2013.34911](https://doi.org/10.13031/2013.34911).
- [157] Cook, N. J., “Comment to “Atmospheric Boundary Layer Modeling in a Short Wind Tunnel” by Dan Hlevca and Mircea Deguratu, *EJM/B Fluids*, 79 (2020), 367-375,” *European Journal of Mechanics-B/Fluids*, 2020.
- [158] Brown, E. H., and Hall, F. F., “Advances in Atmospheric Acoustics,” *Reviews of Geophysics*, Vol. 16, No. 1, 1978, p. 47. doi:[10.1029/rg016i001p00047](https://doi.org/10.1029/rg016i001p00047).
- [159] Vaidya, P., and Dean, P., “The State of the Art of Duct Acoustics,” *4th Aeroacoustics Conference*, American Institute of Aeronautics and Astronautics, 1977. doi:[10.2514/6.1977-1279](https://doi.org/10.2514/6.1977-1279).
- [160] Chong, T., Joseph, P., and Davies, P., “Design and Performance of an Open Jet Wind Tunnel for Aero-Acoustic Measurement,” *Applied Acoustics*, Vol. 70, No. 4, 2009, pp. 605–614. doi:[10.1016/j.apacoust.2008.06.011](https://doi.org/10.1016/j.apacoust.2008.06.011).
- [161] Schlichting, H., and Gersten, K., *Boundary-Layer Theory*, Springer, 2016.
- [162] Green, D. N., Vergoz, J., Gibson, R., Pichon, A. L., and Ceranna, L., “Infrasound Radiated by the Gerdec and Chelophechene Explosions: Propagation along Unexpected Paths,” *Geophysical Journal International*, Vol. 185, No. 2, 2011, pp. 890–910. doi:[10.1111/j.1365-246x.2011.04975.x](https://doi.org/10.1111/j.1365-246x.2011.04975.x).
- [163] Koper, K. D., “Empirical Scaling Laws for Truck Bomb Explosions Based on Seismic and Acoustic Data,” *Bulletin of the Seismological Society of America*, Vol. 92, No. 2, 2002, pp. 527–542. doi:[10.1785/0120000242](https://doi.org/10.1785/0120000242).
- [164] Kim, K., and Rodgers, A., “Waveform Inversion of Acoustic Waves for Explosion Yield Estimation,” *Geophysical Research Letters*, Vol. 43, No. 13, 2016, pp. 6883–6890. doi:[10.1002/2016gl069624](https://doi.org/10.1002/2016gl069624).
- [165] Ceranna, L., Pichon, A. L., Green, D. N., and Mialle, P., “The Buncefield Explosion: a Benchmark for Infrasound Analysis Across Central Europe,” *Geophysical Journal International*, Vol. 177, No. 2, 2009, pp. 491–508. doi:[10.1111/j.1365-246x.2008.03998.x](https://doi.org/10.1111/j.1365-246x.2008.03998.x).
- [166] Park, J., Che, I.-Y., Stump, B., Hayward, C., Dannemann, F., Jeong, S., Kwong, K., McComas, S., Oldham, H. R., Scales, M. M., and Wright, V., “Characteristics of Infrasound Signals from North Korean Underground Nuclear Explosions on 2016 January 6 and September 9,” *Geophysical Journal International*, Vol. 214, No. 3, 2018, pp. 1865–1885. doi:[10.1093/gji/ggy252](https://doi.org/10.1093/gji/ggy252).

- [167] Headlin, M. A. H., Garces, M., Bass, H., Hayward, C., Herrin, G., Olson, J., and Wilson, C., “Listening to the Secret Sounds of Earth's Atmosphere,” *Eos, Transactions American Geophysical Union*, Vol. 83, No. 48, 2002, p. 557. doi:[10.1029/2002eo000383](https://doi.org/10.1029/2002eo000383), URL <https://doi.org/10.1029/2002eo000383>.
- [168] University of Washington, *Incorporated Research Institutions for Seismology Data Management Center*, University of Washington, 1984. URL <http://ds.iris.edu/ds/nodes/dmc/>.
- [169] Alauzet, F., and Loseille, A., “High-Order Sonic Boom Modeling Based on Adaptive Methods,” *Journal of Computational Physics*, Vol. 229, No. 3, 2010, pp. 561–593. doi:[10.1016/j.jcp.2009.09.020](https://doi.org/10.1016/j.jcp.2009.09.020), URL <https://doi.org/10.1016/j.jcp.2009.09.020>.
- [170] Rallabhandi, S. K., “Advanced Sonic Boom Prediction Using the Augmented Burgers Equation,” *Journal of Aircraft*, Vol. 48, No. 4, 2011, pp. 1245–1253. doi:[10.2514/1.c031248](https://doi.org/10.2514/1.c031248), URL <https://doi.org/10.2514/1.c031248>.
- [171] Downs, R., Kaye, S., and Page, J., “Sonic Boom Prediction Workshop 3: Propagation Modeling Using PCBoom,” *AIAA AVIATION 2020 FORUM*, American Institute of Aeronautics and Astronautics, 2020. doi:[10.2514/6.2020-2760](https://doi.org/10.2514/6.2020-2760).

BIOGRAPHICAL SKETCH

Tianshu Zhang was born in Jinzhong, Shanxi, P. R. China. He entered Northwestern Polytechnical University in Xi'an, China after graduating from high school in 2012. Tianshu obtained his Bachelor of Engineering degree majoring in flight vehicle propulsion engineering at Northwestern Polytechnical University in June, 2016. In August 2016, he enrolled in the Master of Science program in mechanical engineering at Northeastern University, Boston. In May 2018, Tianshu finished his master thesis focus on experimental investigation on channel flow heat transfer under the supervision of Dr. Mohammad E. Taslim. In the same year in August, Tianshu joined the Theoretical Fluid Dynamics and Turbulence Group and worked with Dr. Steven A. E. Miller to pursue his Ph.D. degree focusing on infrasound propagation and acoustic-turbulent interaction. In December 2021, Tianshu finished his study and was awarded a Ph.D. degree in aerospace engineering by the University of Florida.